

**Theoretical Investigation of a New Class of
Thermoelectric Materials among the Family of
Heusler Compounds**

By

Himanshu Joshi

Registration No. and Date: MZU/Ph.D/872 of 21.04.2016

Submitted

**in fulfillment for the requirements of the
Degree of Doctor of Philosophy in Physics of
Mizoram University, Aizawl**



**Department of Physics
School of Physical Sciences
Mizoram University, Aizawl
Mizoram, India
November 2018**

**Theoretical Investigation of a New Class of
Thermoelectric Materials among the Family of
Heusler Compounds**

By

Himanshu Joshi

Registration No. and Date: MZU/Ph.D/872 of 21.04.2016

**Submitted
in fulfillment for the requirements of the
Degree of Doctor of Philosophy in Physics of
Mizoram University, Aizawl**



**Department of Physics
School of Physical Sciences
Mizoram University, Aizawl**

Mizoram, India

November 2018

मिज़ोरम विश्वविद्यालय
भौतिक विज्ञान विद्यालय
आइजोल ७९६००४ मिज़ोरम
फोन : ०३८९-२३२८०४४(ड), ९४३६९४०५२३(मो०)
फैक्स : ०३८९-२३३०५२२
प्रोफेसर राम कुमार थापा
संकाय प्रमुख



MIZORAM UNIVERSITY
SCHOOL OF PHYSICAL SCIENCES
AIZAWL 796 004 MIZORAM
Phones : 0389 - 2328044(R),
9436140523(M)
FAX : 0389 - 2330522
E-mail : r.k.thapa@gmail.com
Prof. R. K. Thapa

Dated: 15th November, 2018

Certificate

Certified that Sri Himanshu Joshi has carried out research work under my personal supervision and guidance in the Department of Physics, Mizoram University. The results of research work by Sri Himanshu Joshi have been presented in this thesis entitled "Theoretical Investigation of a New Class of Thermoelectric Materials among the Family of Heusler Compounds" and the same has been submitted to the Mizoram University, Aizawl, Mizoram, for the degree of Doctor of Philosophy in Physics.

Sri Himanshu Joshi has fulfilled all the requirements under the Ph.D. regulations of the Mizoram University. To the best of my knowledge, this thesis as a whole or any part, thereof has not been submitted to this University or any other institution for any other degree or diploma.

(Prof. R. K. Thapa)
Supervisor

Declaration of the candidate

Mizoram University

November 2018

I , Himanshu Joshi, hereby declare that the subject matter of this thesis is the record of the works done by me, that the contents of this thesis did not form basis of the award of any previous degree to me or to the best of my knowledge to anybody else, and that the thesis has not been submitted by me to any other University/Institute.

This is being submitted to the Mizoram University for the degree of Doctor of Philosophy in Physics.

(HIMANSHU JOSHI)

Candidate

(Prof. SUMAN RAI)

Head,
Department of Physics

(Prof. R.K.THAPA)

Supervisor

Acknowledgement

Writing this acknowledgement gives me an opportunity to express my deep sense of gratitude and immense respect to the people who have directly or indirectly, knowingly or unknowingly, encouraged and assisted me in this episode of my academic development. This thesis would never have come out without the hidden support and effort of many wonderful people around.

*The journey of my academic development is commemorated with meeting of innumerable personality, the real architecture of this success. I fell that I was really fortunate to have the guidance and encouragement from my supervisor **Prof. R. K. Thapa**. I have been indebted to him, for his patience and kindness as well as academic experience, which enabled me to solve my problems that I faced during this period of my academic development. Despite being busy with his academic and administrative work, he was always willing to drop everything to help me in every respect. I would have been lost without him. I owe my every achievement to him and shall remain obliged to him forever.*

*This work was supported by research fellowship from **DST-SERB, New Delhi** and I am grateful ever. I am also grateful to the teaching faculty of Department of Physics, Mizoram University, for useful discussion and their valuable suggestion during the course of my work. My heartfelt thanks go to **Prof. R. C. Tiwari, Prof. Zaithanzauva, Prof. Suman Rai, Dr. Hranghmingthanga, Dr. Lalremruata, and Dr. Lalthakimi Zadeng**. My thanks also to all the **non-teaching staff members of Department of Physics and Dean's Office** especially **Pu V. Malsawma (Mala)**, who was always there to help whenever I required any technical assistance.*

Acknowledgement

*I am immensely indebted to my senior **Dr. D. P. Rai**, for his continuous support, encouragement and many valuable advices and all kind of support and care I got during my work. Thanks da, I owe you. I would also like to thank **Mrs. Mamta Gurung** for her tips and suggestions for my work and for her warm hospitality. Further, I would like to thank **Dr. Amit Shanker** and **Dr. Sandeep Chhetri** for their suggestions and discussions, which helped me to make this thesis valuable beyond my imagination.*

*I acknowledge gratefully the warm and motherly hospitality and encouragement extended by **Mrs. Kamala Thapa**. She has always been a guide and source of inspirations, above all, she provided a homely atmosphere that never let me feel the distance of my home. Thanks to **Sunita Didi, Raju Daju and Purnima Bhawju** for their warm hospitality and help. I also thank **Navin Uncle** and his family for their care and support during my stay in Mizoram.*

*For an enormous help and friendship I owe an enormous thanks to all my friends in Mizoram, **Dr. Hari Prasad Jaishi, Dr. Sanjay Singh, Lalhriatpuia Hnamte, Jackson Gurung, Aawaz Rai, Mohanbir Subba, Jayanta Dawhra and Laxman Mirsa**. I had a lot of fun in the Hostel, with my hostel mates **Saurav Upadhyay, Dipendra Khanal, Dipanta Gogoi, Lakhyajit, Sanjay Bhaiya, Prem Bhaiya, Iftakar Bhaiya** and **Engineering guys**, thank you guys. Your presence made me easier and comfortable in the hostel. My heartily thanks extends to all the research colleagues **Dr. Rebecca Lalngaihawmi, Dr. Nirmla Devi, Dr. T. Malsawmtluanga** and many individuals who helped me to make years in **Physics Department, MZU** into an interesting and enjoyable period of my life.*

Acknowledgement

*Most importantly, none of these would have been possible without the love and selfless support of my family. My father **Sri. Shanker Prasad Joshi** and my mother **Smt. Duhita Joshi** are the ones who laid down the foundation stone of my education with all their efforts and taught me to be disciplined and made me follow moral ethics, without which there is no success. My grandparents **Sri. N.D. Bhandari** and **Smt. Madhu Bhandari** were always the source of all inspiration in my life. I am also very thankful to my aunts, **Muna Chema, Appu Chema** and **Rittam Chema** who understand me and have been encouraging me for an early completion of my work. I am grateful to my younger brother **Mr. Hemanka Joshi** who had always been with my parents, looking after the family during my absence. Thank you bhai and best wishes for your future.*

*Thanks to my friends back in Darjeeling, **Binoy, Anupam, Arish, Vivek and Kitu** for making my holidays refreshing, whenever I came home. Special thanks to **Ms. Diksha Giri** for her continuous encouragement and support whenever and whichever way when required. I owe all of you guys.*

*Above all, I thank **Almighty God** for giving me the strength, knowledge, ability and opportunity to undertake this research work and to perceive and complete it satisfactorily. Without his blessing, nothing would have been possible. Finally, I would like to thank everybody, I failed to mention their names one by one but their constant support and encouragement helped me a lot for completion of my work. Once again I thank **God** for all the blessings bestowed upon me and giving all these wonderful people in my life and the opportunity to step forward in the excellent World of Science.*

Dated: 15th November, 2018

Mizoram University, Aizawl.

(Himanshu Joshi)

CONTENTS

Sl. No.		Page No.
1.	Title of the Thesis	<i>i</i>
2.	Certificate	<i>ii</i>
3.	Declaration	<i>iii</i>
4.	Acknowledgement	<i>iv</i>
5.	Contents	<i>vii</i>
6.	List of Figures	<i>x</i>
7.	List of tables	<i>xiv</i>
8.	List of Abbreviations	<i>xv</i>
9.	Chapter 1 : Introduction	1
10.	1.1: Brief Introduction of Thermoelectric effect	2
11.	1.2: Heusler compounds as potential thermoelectric materials	8
12.	1.3: Searching of High efficiency thermoelectric Heusler compounds	15
13.	1.4: Review of Literature	18
14.	1.5: Motivation, Objective and Scope of the Thesis	20
15.	Chapter 2 : Theoretical formalism and Methodology	23

Contents

16.	2.1:	Study of Electronic properties	23
17.	2.1.1:	Density Functional Theory	23
18.	2.1.2:	Details of Theoretical Methodology	25
19.	2.1.3:	Kohn Sham Equation	28
20.	2.1.4:	Local Density Approximation	30
21.	2.1.5:	Generalized Gradient Approximation	31
22.	2.1.6:	Local Spin Density Approximation	33
23.	2.1.7:	FP-LAPW method	34
24.	2.1.8:	Modified Becke Johnson Potential	39
25.	2.1.9:	Equation of states	40
26.	2.1.10:	Elastic Constants	40
27.	2.1.11:	The WIEN2k Code	41
28.	2.2:	Study of Thermoelectric properties	45
29.	2.2.1:	BoltzTraP (Boltzmann Transport Properties) code	45
30.	2.2.2:	Computation of Relaxation time (τ)	47
31.	2.2.3:	Computation of Lattice thermal conductivity	48
32.	Chapter 3	: Electronic and thermoelectric properties of half- Heusler MCoSb (M=Ti, Zr and Hf).	51
33.	3.1:	Structural optimization	51
34.	3.2:	Electronic Properties	57
35.	3.3:	Thermoelectric properties	68

36.	Chapter 4	:	Investigation of new class of Heusler thermoelectric materials	80
37.		4.1:	XAuSn (X=Sc, Lu) Half-Heusler Compounds	80
38.		4.1.1:	Crystal structure of XAuSn (X=Sc, Lu)	81
39.		4.1.2:	Electronic properties and band structures of XAuSn (X=Sc, Lu)	84
40.		4.1.3:	Thermoelectric properties of XAuSn (X=Sc, Lu)	90
41.		4.2:	CoX'Y'Si (X'=Y, Zr; Y'=Fe, Mn) Quaternary Heusler Compounds	98
42.		4.2.1:	Crystal Structure of CoX'Y'Si (X'=Y, Zr; Y'=Fe, Mn)	98
43.		4.2.2:	Density of States and Electronic Structure of CoX'Y'Si (X'=Y, Zr; Y'=Fe, Mn)	102
44.		4.2.3:	Transport properties of CoX'Y'Si (X'=Y, Zr; Y'=Fe, Mn)	111
45.		4.3:	XSiSb (X=Ti, Hf) Half-Heusler Compounds	117
46.		4.3.1:	Structural Optimization of XSiSb (X=Ti, Hf)	117
47.		4.3.2:	Electronic properties of XSiSb (X=Ti, Hf)	119

Contents

48.	4.3.3:	Thermoelectric properties of XSiSb (X=Ti, Hf)	123
49.	Chapter 5	: Conclusion	128
50.	References	:	132
51.	Biodata	:	147
52.	Research	:	150
	Publication		
53.	Reprints of		
	Published Papers		

LIST OF FIGURES

Figure Number	Title of Figure	Page Number
1.1	Schematic representation of Seebeck effect	4
1.2.1	Comparison of highest reported ZT (ZT_{\max}) in Heusler compounds, Cu-based chalcogenides, (Sn,Pb) (Se,Te) compounds, and Skutterudites.	10
1.2.2	Crystal structures of full-Heusler and half-Heusler (Semi-Heusler) alloys.	10
1.2.3	Schematic diagram of band structure of Heusler compounds for different number of valance electrons.	14
1.3	A schematic diagram of the DOS and band structure of semiconductor Heusler compounds that favors thermoelectricity in case of (a) single extremum valance and conduction band (b) Multiple extrema valance and conduction band. E_F' represents the possible shift in Fermi energy when the system is subjected to doping.	17
2.1.1	Unit cell partitioning into atomic spheres (I) and an interstitial region (II)	38
2.1.2	Flow chart of WIEN2k code	44
3.1	(a) Unit cell structure of MCoSb (M=Ti, Zr and Hf), (b) Volume optimization curve for TiCoSb, (c) ZrCoSb and (d) HfCoSb, fitted using the Murnaghan's equation of state.	55
3.2.1	Total DOS of (a) TiCoSb, (b) ZrCoSb and (c) HfCoSb (Green-GGA, Red-mBJ).	58

3.2.2	Partial DOS plot of TiCoSb (a) Ti contribution, (b) Co contribution, (c) Sb contribution, (d) <i>d</i> -states of Ti, (e) <i>d</i> -states of Co and (f) <i>p</i> -states of Sb (Green-GGA and red-mBJ).	60
3.2.3	Partial DOS plot of ZrCoSb (a) Zr contribution, (b) Co contribution, (c) Sb contribution, (d) <i>d</i> -states of Zr, (e) <i>d</i> -states of Co and (f) <i>p</i> -states of Sb (Green-GGA and red-mBJ).	61
3.2.4	Partial DOS plot of HfCoSb (a) Hf contribution, (b) Co contribution, (c) Sb contribution, (d) <i>d</i> -states of Hf, (e) <i>d</i> -states of Co and (f) <i>p</i> -states of Sb.	62
3.2.5	Electronic band structure of (a) TiCoSb, (b) ZrCoSb and (c) HfCoSb (Green-GGA and red-mBJ).	66
3.3.1	Thermoelectric parameters (a) Seebeck effect, (b) Electrical properties and (c) Thermal conductivity as a function of chemical potential.	71
3.3.2	Thermodynamic parameters (a) Debye's temperature and (b) Grüneisen parameter used in calculating lattice thermal conductivity, as a function of temperature.	73
3.3.3	Lattice thermal conductivity of MCoSb (M=Ti, Zr and Hf) (b) Comparison of lattice thermal conductivity of ZrCoSb with the theoretical results of Andrea <i>et. al.</i>	73
3.3.4	Seebeck coefficient of (a) TiCoSb, (b) ZrCoSb and (c) HfCoSb, for different carrier concentration.	77
3.3.5	(a) Electrical conductivity, (b) Electronic thermal conductivity, (c) Total thermal conductivity of TiCoSb (d) ZrCoSb (e) HfCoSb and (f) the Figure of merit.	78
3.3.6	Relaxation time calculated as a function of temperature.	79
4.1	Crystal structure of XAuSn (X=Sc, Au) and their respective volume optimization curves.	82

4.1.2	Total DOS plotted along with the band structure for (a) ScAuSn and (b) LuAuSn.	85
4.1.3	Partial DOS plot of ScAuSn, plotted to show the contributions from different electronic states to the total DOS.	87
4.1.4	Partial DOS plot of LuAuSn, plotted to show the contributions from different electronic states to the total DOS.	88
4.1.5	Seebeck coefficient of (a) ScAuSn and (b) LuAuSn plotted for different levels of charge carrier concentration.	92
4.1.6	Thermoelectric parameters of XAuSn (X= Sc, Lu) plotted as a function of temperature (a) Relaxation time (b) electrical conductivity (c) electronic thermal conductivity (d) lattice thermal conductivity (e) total thermal conductivity and (f) the figure of merit.	94
4.1.7	Thermodynamic parameters (a) Debye's temperature, (b) Equilibrium volume and (c) Grüneisen parameter used in calculating lattice thermal conductivity, as a function of temperature.	96
4.2.1	Volume optimization curve of (a) CoYFeSi (b) CoZrMnSi and (c) Crystal structure of Quaternary Heusler CoX'Y'Si (X'=Y, Zr; Y'=Fe, Mn).	100
4.2.2	DOS plot alongside with the band structure plot for (a) CoZrMnSi (b) CoYFeSi and (c) the band structure plot of CoYFeSi, plotted using GGA XC functional.	104
4.2.3	Partial DOS plot of CoZrMnSi, representing different electronic states contributing to the total DOS.	107
4.2.4	Partial DOS plot of CoYFeSi, representing different electronic states contributing to the total DOS.	108
4.2.5	Seebeck coefficient as a function of temperature plotted at different levels of carrier concentration	112

4.2.6	Thermodynamic parameters (a) Equilibrium volume, (b) Debye's temperature and (c) Grüneisen parameter used in calculating lattice thermal conductivity, as a function of temperature.	114
4.2.7	Thermoelectric parameters of $\text{CoX}'\text{Y}'\text{Si}$ ($\text{X}'=\text{Y}$, Zr; $\text{Y}'=\text{Fe}$, Mn) QH compounds plotted as a function of temperature (a) Relaxation time (b) electrical conductivity (c) electronic thermal conductivity (d) lattice thermal conductivity (e) total thermal conductivity and (f) the Figure of merit.	115
4.3.1	Crystal structure along with the volume optimization curve for (a) HfSiSb and (b) TiSiSb	118
4.3.2	Total DOS and band structure plot of (a) HfSiSb and (b) TiSiSb plotted using GGA approximation.	121
4.3.3	Partial DOS plot of (a) Hf, (b) Si and (c) Sb for HfSiSb.	122
4.3.4	Partial DOS plot of (a) Ti, (b) Si and (c) Sb for TiSiSb.	122
4.3.5	Thermoelectric parameters of HfSiSb (a) Seebeck coefficient, (b) Electrical conductivity and (c) electronic and phononic thermal conductivity and (d) total thermal conductivity, as a function of temperature.	125
4.3.6	Thermoelectric parameters of XYSb ($\text{X} = \text{Hf}$, Ti and $\text{Y} = \text{Ge}$, Si) (a) Seebeck coefficient, (b) Electrical conductivity and (c) total thermal conductivity, as a function of temperature.	126

LIST OF TABLES:

Table Number	Title of Table	Page No.
3.1.	Lattice constants (a), Bulk modules (B) and pressure derivative of bulk modules (B') obtained using Murnaghan's equation of state.	56
3.2.	Calculated band gap for TiCoSb, ZrCoSb and HfCoSb	67
3.3.	Thermoelectric parameters at 800 K where S was found to be maximum.	79
4.1.1	Lattice constants (a), Bulk modules (B) and pressure derivative of bulk modules (B') obtained using Murnaghan's equation of state for XAuSn ($X=Sc, Lu$). The lattice constants values are compared with the experimental results of Sebastian <i>et al.</i>	83
4.1.2	Thermoelectric parameters of ScAuSn and LuAuSn, for those temperatures where ZT is found to be maximum. ScAuSn gives maximum ZT at 1100 K and LuAuSn gives that at 1400 K.	97
4.2.1	Lattice constants (a), Bulk modules (B) and pressure derivative of bulk modules (B') obtained using Murnaghan's equation of state for CoX'Y'Si ($X'=Y, Zr; Y'=Fe, Mn$). The lattice constants values are compared with the theoretically obtained results of Kundu <i>et al.</i> , 2017.	101
4.2.2	Calculated energy band gaps of CoX'Y'Si ($X'=Y, Zr; Y'=Fe, Mn$)	110
4.2.3	Thermoelectric parameters of CoZrMnSi and CoYFeSi, for those temperatures where ZT is found to be maximum. Both CoZrMnSi and CoYFeSi gives maximum ZT at 1100 K.	116
4.3.1	Comparison of the calculated lattice parameters with the available theoretical results for XSiSb ($X=Hf, Ti$).	118
4.3.2	Calculated thermoelectric parameters of XSiSb ($X=Hf, Ti$) at room temperatures	127

LIST OF ABBREVIATIONS

APW	-	Augmented Plane Wave
CBM	-	Conduction Band Minimum
E_F	-	Fermi Energy
DFT	-	Density functional theory
EOS	-	Equation of State
FH	-	Full Heusler
FP-LAPW	-	Full-potential linearized augmented plane wave method
GGA	-	Generalized gradient approximation
HH	-	Half-Heusler
HM	-	Half-metallic
KS	-	Kohn sham
LDA	-	Local density approximation
LSDA	-	Local spin density approximation
mBJ	-	Modified Becke-Johnson
PDOS	-	Partial DOS
PBE	-	Perdew, Burke and Ernzerhof
TDOS	-	Total DOS
TE	-	Thermoelectric
VBM	-	Valence Band Maximum
VdW	-	Van der Waals
XC	-	The exchange and correlation energy
ZT	-	Thermoelectric figure of merit



To my Parents,

I am always grateful to you.....

Chapter 1:

Introduction

Introduction

Being most intelligent life form to have set foot on this planet, we human beings have achieved impressive scientific progress and created technologies that seemed impossible to our fore fathers or impossible even about a decade earlier. While we enjoy the advancement of technology, we are unaware of the cost that Mother Nature has to bear in order to provide us the present advancement. The energy consumption rate of our present generation is diminishing the natural resources and our methods of energy production is causing great environmental hazardous issues. Thus, a potential threat is that we may make Earth unfit to sustain life for our future generation. The energy consumption and production rate globally has increased over 7×10^{20} J (~20 terawatts) annually (Ritchie and Roser, 2018). This is equivalent to about 10,000 crores (100 billion) barrels of oil per year or 20 billion tons of coal per year! A rough estimation of the global energy consumption rate in early 1900's was about 1 terawatt. It is surprising to know how far and how fast we have come. This huge energy consumption would lead to two possible conclusions. Either Earth will exhaust its fossil fuels and we may no longer have source for energy production, or the climate change resulted by burning of such huge amount of fuel may collapse the planetary system. None of it seems like a good conclusion. Another surprising thing to note would be that about 63% of the produced energy is not even utilized but is lost during combustion and heat transfer processes (Forman *et al.* 2016,). That is, about 12.6 terawatts of energy is rejected as waste heat globally. Waste heat is unavoidable for any energy converting machineries and therefore

limits the efficiency of automobile engines and power plants, which as a result consumes more fuel in order to achieve the desired energy output. It is this waste heat that is largely dissipated into the atmosphere and contributes to the global warming. Luckily, there are ways to reduce this waste heat by switching to renewable energy sources without having to worry about natural resources degradation or about climate change effects. One of the approach is by using thermoelectric devices, which has the ability to convert waste unused heat directly to useful electrical energy. These materials are environment friendly and has long life, it therefore has the potentiality to be used as a source of renewable energy. Further, these materials would maximize the efficiency of an engine by reducing their heating effects and would help to approach the Carnot's engine limit. However, use of thermoelectric materials would not surpass the Carnot limit, as according to second law of Thermodynamics (Butler, 1925).

1.1 Brief Introduction of Thermoelectric Effect

Thermoelectricity is the phenomenon by virtue of which heat energy can be converted into electrical energy. It is based upon two primary effects, namely the Seebeck effect and the Peltier effect. These effects along with the laws of thermodynamics is used to derive the thermoelectric effect (Domenicali, 1953). Seebeck effect describes the flow of charge carriers by induced temperature gradient, whereas Peltier effect is mainly associated with heat flow due to induced electric current. Thus, Seebeck effect and Peltier effect works opposite to one another. Named after the discoverer, Seebeck effect is the phenomenon in which two dissimilar conductors, of *p*- and *n*- type, when subjected to thermal gradient (temperature difference), produces an electric potential difference due to migration of charge carriers from hot to cold junction (Seebeck, 1823). This will result in the flow of current from hot to cold junction, until an equilibrium is reached (Fig. 1.1).

The ratio of the difference in voltage to the difference in temperature is referred to as the Seebeck coefficient and is independent of other properties of the material (intrinsic property). Therefore, mathematically, Seebeck coefficient is described as

$$S = \frac{\Delta V}{\Delta T} \quad (1.1)$$

Hence, according to Seebeck effect, in order to create thermoelectric devices, both *n*- and *p*-type charge carriers should diffuse energy under a temperature gradient and electric field. This is the main underlying principle of thermoelectric effect and it leads to an important curiosity. How much energy can be converted by means of thermoelectric devices? That is, it raises a question about the energy conversion efficiency of thermoelectric materials, because for technological and industrial applications, efficiency is always the issue of highest concern. So, the efficiency of thermoelectric materials has to be described and in order to obtain the efficiency, some assumptions should be made first. Two important assumptions are mentioned and are as follows-

- 1) A material as a whole has the electrical conductivity along with its thermal conductivity and Seebeck coefficient a constant.
- 2) The resistance at the hot and cold junction are negligible.

With these assumptions, the power output to the load (shown in Fig. 1.1) can be expressed as

$$P^2 = I^2 R_L \quad (1.2)$$

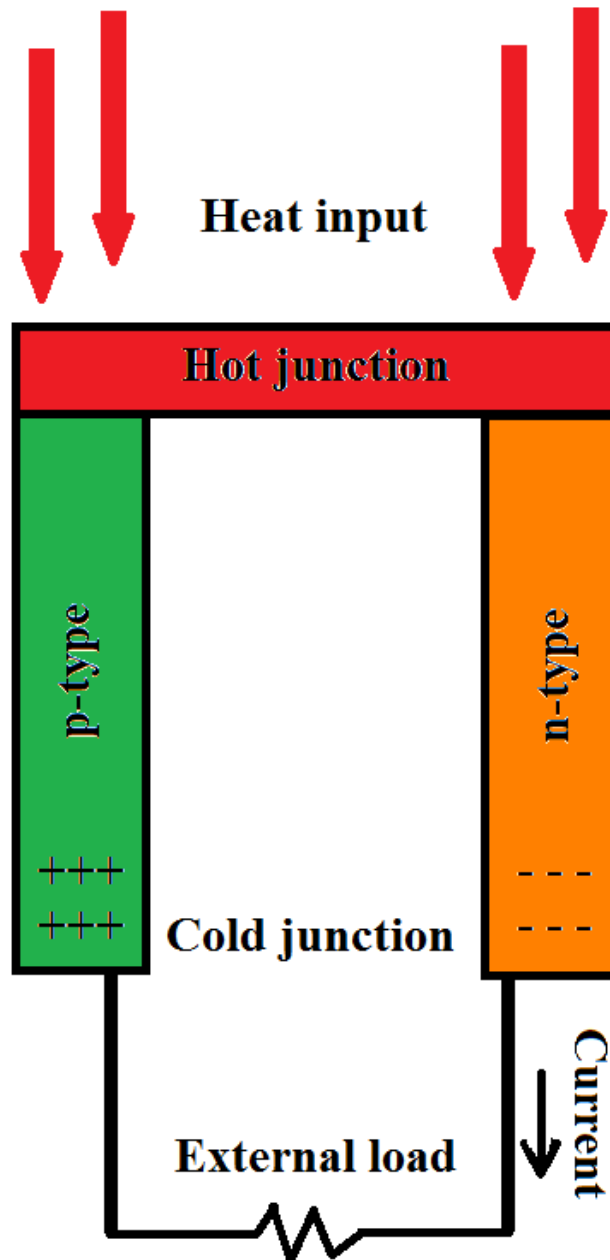


Fig.1.1: Schematic representation of Seebeck effect.

In equation 1.2, I is the current and R_L is the resistivity of the load. The current I is induced by the Seebeck effect and is given by

$$I = \frac{S(T_h - T_c)}{R_L + R} \quad (1.3)$$

where, S is the Seebeck coefficient, R is the total resistance of the p - and n - type conductors and T_h and T_c represents the temperature at the hot and the cold junctions respectively. The electrical power P is maximum when $R_L = R$. Now, the electric current flowing through a material under the influence of Seebeck effect, gives rise to heat flow, according to Peltier effect. The flow of heat in hot junction results due to transfer of heat by electrons through diffusion, when it collides with other electrons (Behnia, 2015) and it consists of three components, the heat flow due to thermal conductivity, absorbed heat at the hot junction due to Peltier effect and the heat due to Joule heating. Heat flow due to thermal conductivity is expressed as

$$Q_t = \kappa(T_h - T_c) \quad (1.4)$$

where, κ represents the thermal conductivity of n - and p -type conductors and T_h and T_c , the temperature of the hot and the cold junction respectively.

The heat absorbed at the hot junction due to Peltier effect is-

$$Q_p = S I T_h \quad (1.5)$$

and the heat due to Joule heating of the thermoelectric material is,

$$Q_j = \frac{1}{2} I^2 R \quad (1.6)$$

Here, the factor $\frac{1}{2}$ arises due to an additional assumption that supposes half of Joules heat flows to the hot side while the remaining half to the cold side. Therefore, efficiency can

be described as the ratio of electrical power to the heat flow on hot side of the thermoelectric material and is expressed as (Rowe, 2005)

$$\eta = \frac{P}{Q_h} \quad (1.7)$$

where, the heat flow to the hot side $Q_h = Q_t + Q_p + Q_j$.

Using equation 1.2 to 1.6, equation 1.7 can be written in case of maximum electrical power as

$$\eta = \frac{T_h - T_c}{\frac{3T_h + T_c}{2} + \frac{4}{Z}} \quad (1.8)$$

where, $Z = \frac{S^2}{R\kappa}$. However $R = R_L$ is not the condition for maximum efficiency but it's the

condition for maximum electrical power. In order to find the condition for maximum efficiency, lets denote $R_L/R = x$. Then η can be denoted as a function of temperature and

maximizing η requires the condition $\frac{\partial \eta}{\partial x} = 0$. Thus,

$$x_0 = (1 + ZT)^{1/2} \quad (1.9)$$

where, $T = \frac{T_h + T_c}{2}$, is the average temperature at the junction. The quantity ZT is a

dimensionless quantity known as the figure of merit and is defined as the maximum efficiency condition of a thermoelectric material. It is expressed as

$$ZT = \frac{S^2 \sigma T}{\kappa} \quad (1.10)$$

where, $\sigma = 1/R$ and κ are the electrical and thermal conductivity respectively. κ comprises of two parts, namely the electronic contribution (k_e) and the phononic or

the lattice contribution (k_p) to thermal conductivity, such that $k = k_e + k_p$. The maximum efficiency can then be expressed in terms of equation 1.9 and can be written as

$$\eta_{\max} = \frac{T_h - T_c}{T_h} \left(\frac{x_0 - 1}{x_0 + \frac{T_c}{T_h}} \right) \quad (1.11)$$

It can be clearly seen from the equation that higher the factor x_0 , higher is the efficiency.

The condition $\frac{T_h - T_c}{T_h} \rightarrow 1$ has to be followed for better efficiency results and can be easily

adjusted by choosing the temperature of the hot junction much higher than that of cold junction. Two limiting case can be applied in equation 1.11. First, $ZT \ll 1$, when ZT is much smaller than 1, $\eta_{\max} \ll 1$. This condition does not interest thermoelectric

application. Secondly, $ZT \gg 1$, then $\eta_{\max} \rightarrow \frac{T_h - T_c}{T_h}$ and the efficiency entirely depends

upon the choice of temperature, so we can have ideal thermoelectric efficiency. The temperature of the hot and cold junction has to be chosen such that it fits practical interest, and for those temperatures generally $ZT \approx 1$, so that $\eta_{\max} \approx 0.3$. It means that about 30% of the heat input is converted into useful electricity. This is the benchmark efficiency value for a material to have potential thermoelectric application (Heremans *et al.* 2008).

Already several materials have proven themselves suitable for thermoelectric applications leading to substantial energy saving in automobiles (Saqr *et al.* 2008) and energy devices (Fleurial *et al.*, 1997). In order to replace the current heat engine systems with thermoelectric materials, we need to find a material with high efficiency having $ZT \geq 3$ (Boukai *et al.* 2008), which would give us an efficiency of about 50% but till date no material with ZT near about 3 is known (Armstrong, 2017). Recently, several attempts are being made to reach the high efficiency targets (Zeier, 2017), but still thermoelectric

materials aren't being used in large scale as its application is limited only up to laboratory standards. There are many potential road blocks for its journey from laboratory to the market place, however there exists a number of ways to optimize its efficiency and is discussed in the section "Searching of High Efficiency Thermoelectric Heusler Compounds" which follows later in this chapter.

1.2. Heusler Compounds as Potential Thermoelectric Materials

Heusler compounds have recently gained attraction as promising thermoelectric materials because of its increasing utility in industrial and automobile waste heat recovery (Chen *et al.*, 2013, Yan *et al.*, 2011 and Kaur *et al.*, 2018). The advantage of choosing Heusler compound lies is their high mechanical and thermal stability (Silpawilawan 2017), low thermal conductivity (Snyder and Toberer, 2008), excellent electronic properties favoring thermoelectric application (Kaue *et al.*, 2017), environmental friendly constituents ensuring low toxicity (Bos and Downie, 2014), low cost of production and elemental abundance (Chen *et al.*, 2013). The working temperature range of Heusler compounds are much higher than other efficient thermoelectric materials like skutterudites, chalcogenides etc. (Olvera *et al.*, 2017). Figure 1.2.1 shows the comparison of working temperature range for Heusler compounds with other thermoelectric materials. Owing to its high temperature performance, Heusler compounds are being considered as the most potential candidates for use in industrial applications.

Heusler compounds were discovered in 1903 and is named after a German chemist Friedrich Heusler (Heusler *et al.*, 1903). The first Heusler compound to be discovered was Cu_2MnAl and it showed ferromagnetic behavior even though none of its constituents had magnetic nature (Heusler *et al.*, 1903). This unique behavior of Cu_2MnAl popularized Heusler compound and since then more than 1500 elemental combinations

are characterized as Heusler compounds. They offer large variety of properties like semiconductors, ferroelectricity, superconductors, topological insulators etc. which gained growing interest creating large field of applications in opto-electronics, magneto-electronic, spintronic, memory control devices and thermoelectric utility.

Heusler compounds are ternary X_2YZ intermetallic, with X and Y as transition elements in the periodic table and Z as the main group element. Generally, they are of two types based on their stoichiometry and chemical formula. The one with chemical formula XYZ is a half-Heusler (HH) compound and has 1:1:1 stoichiometry. It crystallizes in $C1_b$ structure with space group $F\bar{4}3m$ (space group number 216). The second having chemical formula X_2YZ is a full Heusler (FH) compound and has 2:1:1 stoichiometry. It crystallizes in L_{21} structure with space group $Fm\bar{3}m$ (space group number 225). Their crystal structure are shown in Fig. 1.2.2. The crystal structure of full-Heusler consists of four interpenetrating *fcc* sublattices. The two X atom occupies the Wyckoff position $8c$ with coordinates $(3/4, 3/4, 3/4)$ and $(1/4, 1/4, 1/4)$, Y and Z takes the Wyckoff position $4a$ and $4b$ with coordinates $(0, 0, 0)$ and $(1/2, 1/2, 1/2)$ respectively (Graf *et al.*, 2011). This structure is similar to a zinc blende-type sublattice, consisting of one X and Z, where the remaining tetrahedral holes is occupied by second X and Y located in the octahedral holes (Graf *et al.*, 2011).

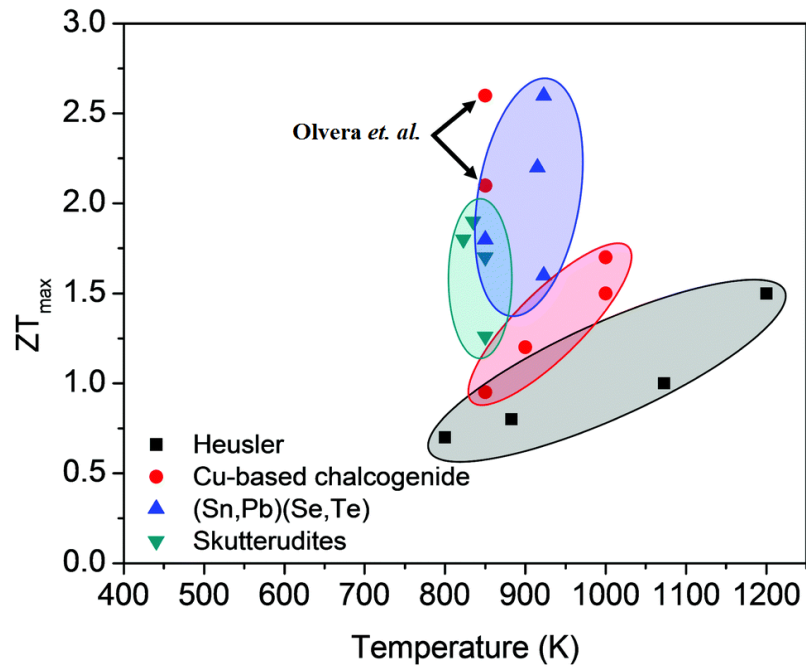


Fig. 1.2.1: Comparison of highest reported ZT (ZT_{max}) in Heusler compounds, Cu-based chalcogenides, (Sn,Pb) (Se,Te) compounds, and Skutterudites (Olvera *et al.*, 2017).

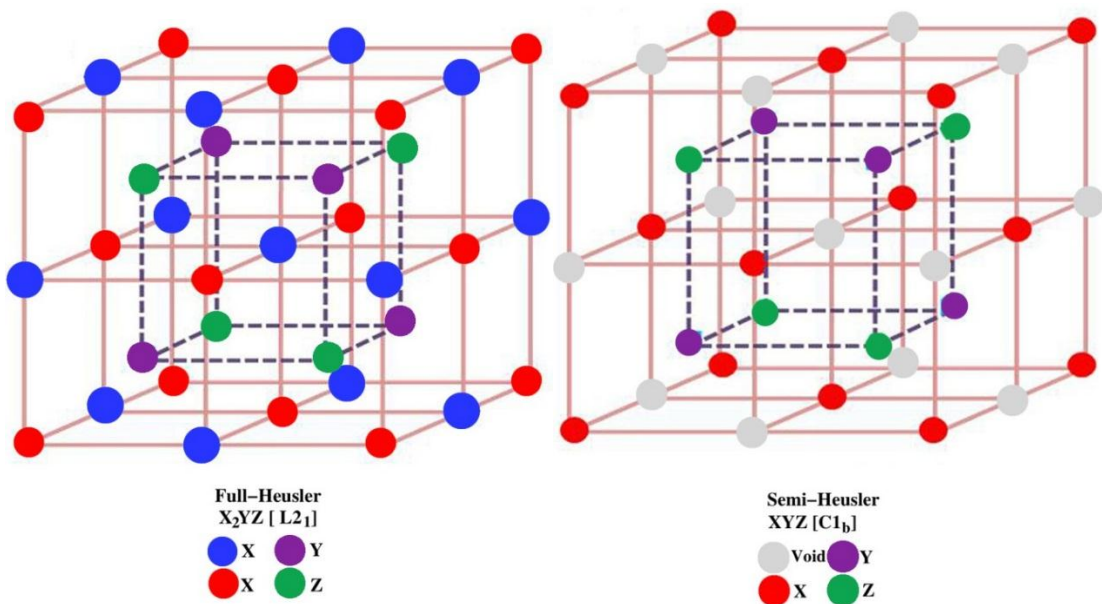


Figure 1.2.2: Crystal structures of full-Heusler and half-Heusler (Semi-Heusler) alloys.

Half-Heusler crystal structure is closely similar to that of the full-Heusler one and can be considered as a tetrahedral ZnS-type structure with filled octahedral lattice sites. Unlike the full-Heusler structure, it has three interpenetrating *fcc* sublattices, with X atom occupying the Wyckoff position *4c* (1/4, 1/4, 1/4), Y atom the position *4a* (0, 0, 0) and Z atom the position *4b* (1/2, 1/2, 1/2), the position (3/4, 3/4, 3/4) remains vacant. The other inequivalent lattice site occupancies are X (*4a*) Y (*4b*) Z (*4c*), X (*4b*) Y (*4c*) Z (*4a*) and X (*4c*) Y (*4a*) Z (*4b*) (Graf *et al.*, 2011).

Recently, a new class of Heusler compounds known as quaternary Heusler compounds (QH) have started to emerge (He *et al.*, 2018 and Kundu *et al.*, 2017). They are found to be semiconducting based upon the 18 or 24 electron rule and are also being considered for thermoelectric applications. When a full Heusler compound with the chemical formula X_2YZ is substituted with a transition element say X' , such as to give the chemical formula $XX'YZ$, then a quaternary Heusler compound is formed. They are based upon the structural prototype of LiMgPdSn with space group of a half-Heusler compound, occupying the Wyckoff positions *4c*, *4d*, *4b* and *4a* respectively for X, X' , Y and Z. Two of such compounds namely, CoYFeSi and CoMnZrSi are investigated for their potential thermoelectric applications in this thesis.

The Slater-Pauling (S-P) rule (Slater, 1936 and Pauling, 1938) has its importance in determining the band structure properties of Heusler compounds which can be predicted by simply counting the valence electrons. The magnetic moment of Heusler compounds can be determined easily from the S-P equation expressed as $M = (Z-18) \mu_B$ (for half-Heusler compounds) and as $M = (Z-24) \mu_B$ (for full-Heusler compounds), where M and Z are the magnetic moment and the number of valence electrons in the unit cell (Galanakis *et al.*, 2006). HH and FH compounds with valence electron count (VEC) of

18 or 24 has magnetic moment 0, as seen from S-P equation and are of particular interest to us because they are non-magnetic and exhibits semiconducting properties, which is favorable for thermoelectric applications (Galanakis *et al.*, 2006). These type of Heusler alloys have electronic band structure with narrow band gaps and is beneficial for thermoelectric properties (Yang *et al.*, 2008 and Osterhage *et al.*, 2014). Particularly, compounds with VEC of 18 shows closed cell behavior and are found to be semi-metals or semiconductors. Studies have shown that 18 VEC system consisting of light transition elements are reported to exhibit excellent thermoelectric properties (Sootsman *et al.*, 2009). For these systems, the electronic states responsible for the occurrence of band gap, plays a vital role on determining the behavior of transport properties. 18 VEC system consisting of heavy elements like Pt, Au, Pb, Bi or Po and the elements from lanthanide series exhibit nearly zero band gap and are called gapless semiconductors. Such materials with zero direct band gaps are predicted to be topological insulators and are currently being considered for thermoelectric applications (Ding *et al.*, 2015), however much progress has to be made to enhance the thermoelectric efficiency of these type of systems. Among nine compounds that we have investigated, two compounds, namely LuAuSn and CoYFeSi falls in this category.

Heusler compounds with VEC of 21 to 23 are found to be ferromagnets exhibiting half-metallic properties (de Groot *et al.*, 1983), whereas compounds with VEC of 20, are highly unstable compounds (Tobola *et al.*, 1998). A schematic diagram of the band structure of Heusler compounds for different number of valence electrons is presented in Fig. 1.2.3. In reference to the figure, the band structure that supports thermoelectricity most, is the one with the VEC of 18 or 24. The size of the band gap of such systems depends largely on the hybridization between the *d*-states of *X* and *Y* atom. It is to be

noted that, structural disorders like imperfection and defects largely affects the band structure. Mostly, experiments take these disorders into account whereas, theoretical studies are based upon perfect single crystals and this leads to the over estimation of band gaps by theoretical prediction, which finally affects the thermoelectric performance. Apart from that, the degeneracy of the bands and the structure of the valence and the conduction band plays leading role in determining the thermoelectric properties and is discussed in the next section that follows.

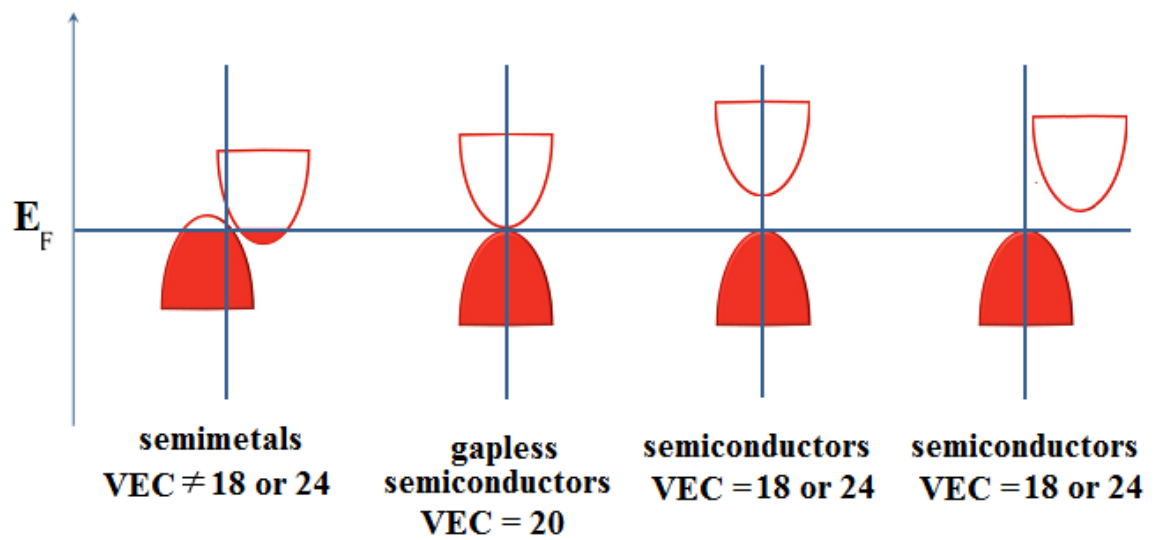


Figure 1.2.3: Schematic diagram of band structure of Heusler compounds for different number of valence electrons.

1.3. Searching of High Efficiency Thermoelectric Heusler Compounds

As mentioned earlier, the efficiency of thermoelectric material depends upon the constituent materials and there exists number of parameters that relates to the thermoelectric efficiency. Therefore in this section, it is intended to highlight key factors that are important while searching for high performance Heusler thermoelectric materials and factors which enhances their efficiency. In order to enhance the efficiency, high ZT values are necessary to obtain. In reference to the efficiency expression given by equation 1.8 and the ZT expression given by equation 1.10, it is clear that in order to achieve the best efficiency, thermal conductivity (κ) has to be minimized and the power factor ($S^2\sigma$) has to be maximized. However, this task is not as easy as it seems because these parameters are inter-related and it's a challenge to simultaneously achieve high power factor along with low thermal conductivity in the same material.

One of the method to enhance the efficiency is by enhancing the electronic properties which would ultimately lead to high ZT value. This can be achieved by optimizing the carrier concentration of the material. Decreasing the carrier concentration increases S and decreases κ , but it simultaneously decreases the electrical conductivity (σ) as well. Therefore, one has to compromise for low σ value in order to achieve high S value. This method can be easily realized by doping electron or hole to the respective n - or p -type thermoelectric material. Thus, the Heusler compounds has to be chosen in such a way that the electrical conductivity of the material does not become very low on optimizing its carrier concentration. To ensure this, the X and Y combination of the Heusler compound has to be chosen such that either of it contains highly efficient electrical conductors like group 10, group 11 or group 12 elements of the periodic table,

while the Z combination has to be metalloid to ensure low thermal conductivity (middle elements in group 3A to 6A).

Another way to choose high efficient Heusler thermoelectric material is by investigating their electronic properties. The shape of the Density of States (DOS) and the electronic band structure has a significant impact on the carrier concentration and thermoelectric performance of the materials. Most of the 18 VEC systems have flat slopes for DOS and the Fermi energy (E_f) lies just above the valence band, within the conduction region. As a result, E_f almost remains constant with temperature when charge carriers flow from valence band to the conduction band, leading to enhanced S [Kittle *et al.*, 2006]. The band structure of these type of Heusler compounds becomes more complex if d - or f -orbitals are included in the valence electrons. Such band structure shows high degeneracy along with steep DOS slopes at the Fermi level and is beneficial to obtain large ZT (Mahan *et al.*, 1996 and Pei *et al.*, 2012). Further, their band structure features steep slopes of the valence band maximum (VBM) and has more than one maxima of the valence band. Steep slope ensures low effective mass of the charge carriers, and multi maxima the high electrical conductivity, both of which favors thermoelectricity (Pei *et al.*, 2012). Therefore, Heusler compounds with VEC of 18 involving d - or f -orbitals in the electronic structure highly favors thermoelectricity and has to be beard in mind while choosing Heusler thermoelectric materials. A schematic diagram of the DOS and band structure that favors thermoelectricity in Heusler compound is shown in Fig. 1.3. It is assumed that the band structure obeys parabolic band model.

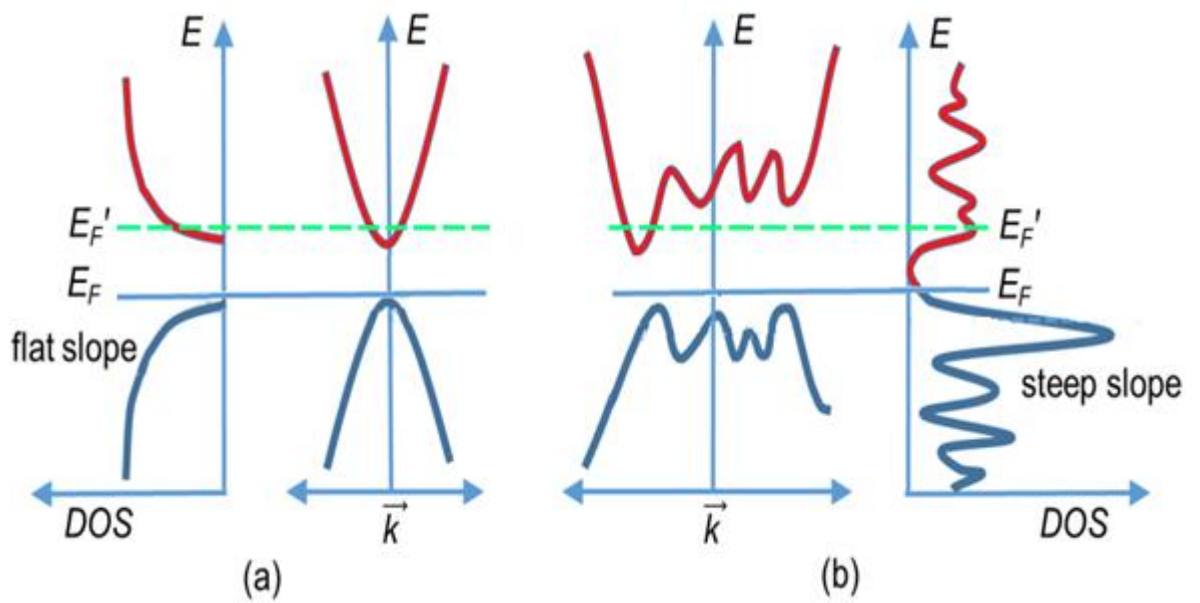


Fig. 1.3: A schematic diagram of the DOS and band structure of semiconductor Heusler compounds that favors thermoelectricity in case of **(a)** single extremum valence and conduction band **(b)** Multiple extrema valence and conduction band. E_F' represents the possible shift in Fermi energy when the system is subjected to doping.

Therefore changing the slope and the band degeneracy to adjust the band structure is an important tool for enhancing the thermoelectric properties. However, to achieve this is also a challenge and cannot be achieved easily because the degeneracy of the bands can only be changed by changing the crystal structure.

1.4 Review of literature

In the last few decades, tremendous research interest is observed in the field of thermoelectrics. This results due to the continuous need of efficient materials for alternative sources of power generation. Waste heat which limits the engines efficiency is also solely responsible for climate change problems and with the advancement of this technology, all can be taken care of. Almost two centuries have passed since the first thermoelectric effect was discovered but still its technological applications are limited. In this section, the advancement in the field of thermoelectrics, based upon the available literature that acted as the basis of this thesis is presented.

In 1821 Thomas Johann Seebeck observed that a magnetic compass got deflected when temperature difference was established between the junctions of two dissimilar conductors. It was later identified that the deflection of the compass was due to the electric voltage that was set up due to the temperature difference in the junction of two materials which as a result produced an electric current and a magnetic field (Seebeck, 1823). This effect was named as Seebeck effect after the name of the discoverer.

(Sherman *et al.*, 1960) calculated the efficiency of thermoelectric devices with respect to power generation and refrigeration. Thermoelectric refrigeration is outside the scope of the Thesis and thus only power generation is considered in this work. The

optimum efficiency of a thermoelectric material was reported in their work as a function of temperature difference between the hot and the cold junctions.

Works done by Decher, 1997 and Rowe, 2005 acted as the basis in understanding the fundamental behavior of thermoelectricity. Works done by Rowe further provided a foundation on increasing the efficiency of thermoelectric material by reducing their dimension. Increasing the efficiency by reducing the dimensionality of a material is again outside the scope of the Thesis and is not considered in this work. However, we have made a theoretical analysis on enhancing the thermoelectric figure of merit (ZT) of silicon by reducing its dimension to atomic scale, in an attempt to fully understand the thermoelectric effect (Joshi *et al.*, 2016 and Joshi *et al.*, 2017). It is to be noted that the work done in this thesis interests only in the efficiency of pure Heusler compounds, with no structure modification or what so ever which implements reduction in dimensionality or doping effects.

(Yang *et al.*, 2008) calculated the power factor ($S^2\sigma$) of various HH compounds, based upon their electronic structure, in order to investigate their thermoelectric efficiency. They had reported that HH compounds which were narrow band gap semiconductors showed high power factor and are most likely to be efficient thermoelectric materials. Co, Fe and Rh based materials with p -type characteristics were expected to give high ZT values.

(Zheng, 2008) has given a detailed review of works on thermoelectric materials where it had been pointed out that thermoelectric materials with ZT values as high as 14 is possible, especially with rare earth compounds. This is feasible only with the advancement of the first principles model calculations like FP-LAPW.

(Xi *et al.*, 2012) had predicted the intrinsic charge mobility of organic materials using Boltzmann's transport equations and had derived an expression for relaxation time that can be calculated using first principles models. Our calculation of relaxation time is based upon the relaxation time model of Xi and coworkers.

The Condensed Matter Theory Group of Prof. R. K. Thapa had been investigating the thermoelectric and physical properties of Heusler (Rai *et al.*, 2012), Bi₂Se₃, Bi₂S₃ (Deka *et al.*, 2015) and skutterudites systems (Shankar, 2016). The group has done works extensively related to energy bands, magnetic and optical properties of skutterudites and also studied the effect of thermal conductivity and phonon contribution so that efficiency of the thermoelectric materials is increased more than unity.

1.5. Motivation, Objective and Scope of the Thesis

The real challenge of present day technological world is the utilization of easily accessible energy source for the production of new energy materials (devices). The degradation of fossil fuel due to the over consumption is the major threat. The whole scientific world is in search for the alternative sources of energy for the sustainable life. The increase in demand for energy has accelerated the search of clean and renewable energy sources. Thermoelectric devices represent a solution to this problem as they have the potentiality to convert heat into electricity without pollutant emission. Thus, the development of thermoelectric materials will lead us to a solution of world's energy crisis.

Devices based on thermoelectric (TE) materials are very appealing as they are the kind of green energy materials which absorb waste heat and convert to electrical energy or can be used as refrigerator cooling device by applying electricity. Many thermoelectric materials were studied till date but due to low efficiency they could not be exploited

commercially. The materials based on Lead, Tellurium, Selenium and Antimony are considered to be efficient thermoelectric materials but the toxicity has restricted their applications in practical use. Thus, new environmental friendly energy materials whose performance is as good as those typical thermoelectric materials are in technological demand. Due to this, it has become necessary to develop theoretical models for study of these materials systematically to understand their scientific behaviors.

The thermoelectric properties of Heusler compounds are not subjected to intense study by using first principles theory, owing to the correlation effects involved in the electron states. Thus, in our work, the study will be carried out using full-potential linearized augmented plane wave (FP-LAPW) (Wimmer *et al.*, 1981) basis sets along with the generalized gradient approximation (GGA) (Perdew *et al.*, 1996), within the frame work of Density functional theory (DFT) (Hohenberg and Kohn, 1964 and Kohn and Sham, 1965). Most theoretical models doesn't employ the relaxation time of the charge carriers in the calculation of transport properties and hence the thermoelectric parameters are made to depend upon the relaxation time. In this work, we attempt to calculate the relaxation time of the charge carriers for the compounds under study, in order to provide a complete theoretical calculation of the transport properties, without having to depend upon the experimental references, which was found lacking in earlier theoretical methods.

Last but not the least, we intend to show a method for the calculation of lattice thermal conductivity using the Slack's equation based upon quasiharmonic approximations, which transport properties calculation codes like BoltzTraP are unable to calculate. The methods of calculation along with the associated theory are discussed in the Thesis under chapter 2 titled as "Theoretical Formalism and Methodology". Recently

ab initio codes like ShengBTE (Li *et al.*, 2014) has been developed which can calculate lattice thermal conductivity from second and third order interatomic force constants. It works by solving the Boltzmann's transport equations for phonons but is extremely computationally expensive and requires high computing facilities which we lack.

The chapters in the thesis are organized as follows:

In Chapter 2, we describe the theory and methodology used in our calculation. We will also present an outline of the density functional theory (DFT) within GGA, mBJ and FP-LAPW method. Transport properties based upon Boltzmann's transport equations is also discussed in brief.

In Chapter 3, we discuss the structural, electronic and thermoelectric properties of three HH compounds MCoSb (M=Ti, Zr, Hf). They are investigated for the purpose of comparing the experimental results with the results obtained by using the theoretical approach that we follow.

Chapter 4 deals with the new types of thermoelectric materials investigated for potential thermoelectric applications. Six new class of compounds investigated are presented in this chapter.

Chapter 5 contains the concluding part of the thesis where we have summarized the studies done on thermoelectric properties of HH compounds and it is followed by references.

Chapter 2:

***Theoretical Formalism
and Methodology***

Theoretical Formalism and Methodology

This chapter deals with the theory, methods and approximations used in the study of electronic and thermoelectric properties. The calculation of electronic structures are based upon Density Functional Theory employing the code WIEN2k (Blaha *et al.*, 2012), which comprises of a number of FORTRAN and C programmes. The calculation of thermoelectric properties involves various post DFT approach which involves program codes like BoltzTraP (Madsen and Singh, 2006) and Gibbs2 (Otero-de-la-Roza *et al.*, 2011). The results obtained from the electronic properties within the DFT framework, acts as the input to the thermoelectric properties calculation. They are discussed in details here under as follows-

2.1 Study of Electronic Properties

2.1.1 Density Functional Theory (DFT)

Condensed matter physics is related to the study of physical, electronic and other basic properties of matter. We can examine and describe the nature by various experimental science, but the interaction between the experiment and theory is extremely necessary to understand and describe the basic properties of matter. Under normal conditions, the material properties are governed by motional behaviour of electrons and the field of the nuclei of the constituent atoms. Thus, electronic band structure knowledge is essential to understand the physical properties of matter. In condensed matter physics, one studies the physical properties of the systems within the framework of already

established quantum theory. Many solids and crystals are ordered and can be successfully described mathematically neglecting the defect in the crystal, which plays a vital role in describing the material property.

In reality, a matter is more complex and is composed of infinite interacting atoms, which responds to an external field. Various techniques that are developed to describe the motion of collection of atoms and electrons are based upon Density Functional Theory. DFT is the most commonly used technique in condensed matter physics and was originally invented and developed by Kohn, Hohenberg and Sham (Hohenberg and Kohn, 1964; Kohn and Sham, 1965). It acts as a modern tool to determine the ground state properties of atoms, molecules and solids. DFT is mainly based upon two theorems, the Hohenberg and Kohn theorem and the Kohn and Sham theorem. Hohenberg and Kohn theorem reduces the many body problem by introducing the concept of electron density functional. The Kohn and Sham theorem defines energy functional and shows that the ground state density minimizes the energy functional. In short, these theorems asserts that all information available in the wave function is also available in the electronic ground state density and this density can be found through energy minimization procedures. The computational challenge of calculating the properties of a complex material is also greatly reduced. Therefore, within the framework of Kohn-Sham DFT (KS-DFT), intractable many-body problem of interacting electrons in a static external potential is reduced to a tractable problem of non-interacting electrons moving in an effective potential (Kohn and Sham, 1965). The external potential and Coulomb interaction between the electrons exchange and correlation is contained in the effective potential. Modeling the two interactions is the challenge within KS-DFT.

2.1.2 Details of Theoretical Methodology

According to Born-Oppenheimer approximation, many body system nuclei is represented by a wave function $\Psi(\vec{r}_1, \dots, \vec{r}_N)$ and satisfies the Schrodinger equation of many-electron system given by (Combes, 1977)

$$H\Psi = [T + V + U]\Psi = \left[\sum_i^N -\frac{\hbar^2}{2m} \nabla_i^2 + \sum_i^N V(\vec{r}_i) + \sum_i^N U(\vec{r}_i, \vec{r}_j) \right] \Psi = E\Psi \quad (2.1)$$

where H is the Hamiltonian of electrons, N is the number of electrons, T is the kinetic energy of N -electrons, V is the potential energy of the external field to N -electron, U is the electron-electron interaction energy for the N -electron system. The operators T and U are common for similar systems, so are called Universal operators. V is non-universal as it is system dependent. Now, the difference between a single particle problem and the complex many particle problem is the interaction term U . DFT provides a method in which the interaction term U of a many-body system can be systematically mapped onto a single particle system without U . The particle density $n(\vec{r})$ for a normalized Ψ can therefore be written as:

$$n(\vec{r}) = N \int d^3r_1 \int d^3r_2 \dots \int d^3r_N \Psi^*(\vec{r}_1, \vec{r}_2, \dots, \vec{r}_N) \Psi(\vec{r}_1, \vec{r}_2, \dots, \vec{r}_N) \quad (2.2)$$

In reverse way, this relation states that for a known ground-state density $n_0(\vec{r})$ it is possible to construct the corresponding ground-state wave-function $\Psi_0(\vec{r}_1, \vec{r}_2, \dots, \vec{r}_N)$. In other words $\Psi_0(\vec{r}_1, \vec{r}_2, \dots, \vec{r}_N)$ is a functional of $n_0(\vec{r})$ and hence the ground state expectation values of an observable \hat{O} is also a functional of $n_0(\vec{r})$.

$$O[n_0] = \langle \Psi[n_0] | T + V + U | \Psi[n_0] \rangle \quad (2.3)$$

In particular, the energy of the ground state is functional of $n_0(\vec{r})$

$$E_0 = E_0[n_0] = \langle \Psi[n_0] | T + V + U | \Psi[n_0] \rangle \quad (2.4)$$

$$= \langle \Psi[n_0] | T | \Psi[n_0] \rangle + \langle \Psi[n_0] | V | \Psi[n_0] \rangle + \langle \Psi[n_0] | U | \Psi[n_0] \rangle \quad (2.5)$$

$$= T[n_0] + V[n_0] + U[n_0] \quad (2.6)$$

where $\langle \Psi[n_0] | V | \Psi[n_0] \rangle$ is the contribution of the external potential and is expressed in terms of the ground-state density n_0 as

$$V[n_0] = \int V(\vec{r}) n_0(\vec{r}) d^3r \quad (2.7)$$

More commonly, the external potential contribution $\langle \Psi | V | \Psi \rangle$ can be written clearly in terms of the density n as

$$V[n] = \int V(\vec{r}) n(\vec{r}) d^3r \quad (2.8)$$

A system is defined by a definite non-universal functional V , as $T[n]$ and $U[n]$ are universal. For a given system with V as its external potential

$$E[n] = T[n] + U[n] + \int V(\vec{r}) n(\vec{r}) d^3r \quad (2.9)$$

In regard to $n(\vec{r})$, taking for granted one has got dependable terms for $T[n]$ and $U[n]$. A successful reduction in energy functional produces ground state density $n_0(\vec{r})$ and therefore produces all other observable ground states.

The variational principle of Rayleigh-Ritz is made capable of finding the ground-state density by the second KS-theorem. The number of possible densities are infinite, but the density which minimizes $E[n]$ is the external potential $V(\vec{r})$. This is possible only if the approximation to $\langle \Psi[n] | T + V | \Psi[n] \rangle$ is known. But knowing $n(\vec{r})$, all knowledge about the system will be within reach. It is useful to stress the meaning of the energy

functional $E[n]$ once more. This implies that, when $E[n]$ is assessed for the density $n(\vec{r})$ corresponding to a particular $V(\vec{r})$, it gives the ground state energy. However, when it is evaluated for any other density, the result has no physical meaning (Cottenier, 2002).

Neglecting the electron-electron interaction energy term, the energy functional is expressed as

$$E_s[n] = \langle \Psi_s[n] | \hat{T}_s + V_s | \Psi_s[n] \rangle \quad (2.10)$$

where \hat{T}_s is the non-interacting kinetic energy and \hat{V}_s is an external effectual potential where the particles are moving. Clearly, if \hat{V}_s is $n_s(\hat{r}) = n(\hat{r})$ selected be

$$\hat{V}_s = \hat{V} + \hat{U} + (\hat{T} - \hat{T}_s) \quad (2.11)$$

Consequently, the Kohn-Sham equations for this assisting non-interacting system can be solved as,

$$\hat{H}_{KS} \phi_i = E_i \phi_i \quad (2.12)$$

this produces the ϕ_i orbital from which the density $n(\vec{r})$ of the genuine many-body system can be reproduced.

$$n(\vec{r}) = n_s(\vec{r}) = \sum_i^N |\phi_i(\vec{r})|^2 \quad (2.13)$$

The single-particle effective potential can be detailed as

$$V_s(\vec{r}) = V(\vec{r}) + \int \frac{e^2 n_s(\vec{r}')}{|\vec{r} - \vec{r}'|} d^3 r' + V_{XC}[n_s(\vec{r})] \quad (2.14)$$

The last term V_{XC} stands for exchange correlation potential and second term for Hartree expression of Coulomb repulsion for electron-electron interaction. Now, the second and last term depends on $n(\vec{r})$ which relies on ϕ_i , which further depends on \hat{V}_s .

Now, the problem here is that K-S equation needs self-consistency solution. One typically begins with a first guess $n(\vec{r})$ then works out the corresponding \hat{V}_S and solves the Kohn-Sham equations for the ϕ_i (Kohn and Sham, 1965). DFT's techniques are different and complex and thus requires the following two approach for understanding.

Firstly the techniques that apply a local density rough calculation (LDA). The LDA is decided exclusively and based on the qualities of the electron density. The significant supposition of the approximation is, for a molecule which has large number of electrons in a gaseous state, throughout the molecule the density will be consistent. This case doesn't hold for molecules and systems where the electron density is emphatically not consistent. The approximation works well with electronic band structure of solids and hence illustrates the scope of energies in which electrons are allowed or not allowed. Outside of these applications, however, LDA's are not very acceptable.

Secondly, the technique is to unite the calculation of electron density with a gradient correction factor. Mathematically, gradient is a function which measures rate of change of a property. In this case, gradient explains the electron density non-uniformity and is thus termed as gradient-corrected.

2.1.3 Kohn-Sham Equation

Since the total energy of the system is

$$E(n) = T(n) + \int V_{ext}(r)n(r) dr + V_H[n] + E_{XC}[n] \quad (2.15)$$

where T is the kinetic energy of the system, V_{ext} is an external potential acting on the system, E_{XC} is the exchange-correlation energy and Hartree energy is given by

$$V_H = \frac{e^2}{2} \int \frac{n(r)n(r')}{|r-r'|} dr dr' \quad (2.16)$$

The straight forward application of this formula has two barriers: First, the exchange-correlation energy E_{XC} is not known precisely and second, the kinetic term must be created in terms of the charge density. As was first suggested by Kohn and Sham (1965), the charge density $n(r)$ can be written as the sum of the squares of a set of orthonormal wave functions $\phi_i(r)$:

$$n(r) = \sum_i^N |\phi_i(r)|^2 \quad (2.17)$$

where the single particle wave function $\phi_i(r)$ are the N lowest-energy solutions to the Kohn-Sham equation for N non-interacting electrons moving in an effectual potential $V_{eff}(r)$ is given by

$$-\frac{\hbar^2}{2m} \nabla^2 \phi_i(r) + V_{eff}(r) \phi_i(r) = \varepsilon_i \phi_i(r) \quad (2.18)$$

where the effectual potential is defined to be

$$V_{eff}(r) = V_{ext}(r) + e^2 \int \frac{n(r')}{|r-r'|} dr' + \frac{\delta E_{XC}[n]}{\delta n} \quad (2.19)$$

This system is then solved iteratively until self-consistency is approached. It is to be noted that the eigen values ε_i have no physical meaning but the total sum matches the energy of the entire system E through the equation:

$$E = \sum_i^N \varepsilon_i - V_H[n] + E_{XC}[n] - \int \frac{\delta E_{XC}[n]}{\delta n(r)} n(r) dr \quad (2.20)$$

There are several ways to apply Kohn-Sham theory depending on what is being examined. In solid state calculations, for electrons delocalized through an infinite solid, electron gas approach is still more suitable to use and hence the local density

approximation along with plane wave basis sets is commonly used. Molecular calculations further demand much complex functionals for chemical applications. The problem with DFT is that only for free electron gas, there exists a precise functional for exchange and correlation. However, still the calculations of certain physical parameters can be achieved with great precision, which makes LDA the most widely used approximation.

2.1.4 Local Density Approximation

The LDA has been the most widely used exchange-correlation energy approximation in the Density Functional Theory for a long time. It has been proposed by Kohn and Sham (1965). It works upon the idea of considering inhomogeneous electronic systems as locally homogeneous and then to apply exchange-correlation hole corresponding to the homogeneous electron gas. LDA has been widely applied to portray a variety of close-ranged exchange-correlation interactions for instance, covalent bonding systems. However, LDA suffers from a serious limitation that is, it cannot provide estimation to the long-ranged exchange-correlation interactions like the Van der Waals (VdW) interaction. The VdW interaction being an electronic interaction of long range mainly add to the first stage of the material reactions such as the physical absorption, crystal growth and chemical reaction. Many efforts has been made to assess the VdW interaction in order to develop the calculation of non-local exchange-correlation term. According to Hohenberg-Kohn theorem the energy of the ground state is a functional of the electronic density. This implies that XC energy is also a functional of the density. This XC functional is not identified accurately and must be addressed appropriately with correct approximation. For this functional, LDA is the simplest approximation. The electron exchange and correlation energy at any point in space is a function of electron

density at that point only, hence it is local in this sense. The XC functional is the total of correlation functional and exchange functional and is expressed as

$$E_{XC} = E_X + E_C \quad (2.21)$$

LDA uses the exchange for the uniform electron gas of a density equal to the density at the point where the exchange is to be assessed

$$E_{XC} = \int d^3r n(\vec{r}) \left(\frac{-3e^2}{4\pi} \right) \left(3\pi^2 n(\vec{r})^{1/3} \right) \quad (2.22)$$

All quantities are represented as functional of the electronic charge density. The significant point that eases the solution of such system is that the efficient possibility is local. Therefore there is no more complication added in solving Schrodinger equation. Of course, this is only true if the exchange-correlation energy can be portrayed as a function of the local charge density. A technique of doing this is LDA. As mentioned above in LDA, electronic systems XC energy is built by taking for granted that the XC energy for each electron at a point \vec{r} in an electron gas equals the XC energy for each electron in an identical electron gas that has the same electron density at the point \vec{r} . It follows therefore

$$E_{XC} [n(\vec{r})] = \int \varepsilon_{XC}(n(\vec{r})) n(\vec{r}) dr \quad (2.23)$$

with

$$\varepsilon_{XC}(n(\vec{r})) = \varepsilon_{XC}^{\text{hom}}(n(\vec{r})) \quad (2.24)$$

where $\varepsilon_{XC}^{\text{hom}}(n(\vec{r}))$ is XC energy in identical electron gas. Eq. 2.24 is the supposition that the exchange-correlation energy is purely local. Several parameterizations for $\varepsilon_{XC}^{\text{hom}}(n(\vec{r}))$ exist, such as parameterization of Perdew and Zunger (1981).

2.1.5 Generalized Gradient Approximation

The gradient expansion of XC energy is of the type

$$E_{XC}[n(r)] = \int A_{XC}[n(r)]n(r)^{4/3} dr + \int C_{XC}[n(r)]|\nabla n(r)|^2 / n(r)^{4/3} dr + \dots \quad (2.25)$$

which is asymptotically valid for densities that vary slowly in space. Only the initial term of the above Eq. 2.25 is retained by LDA. Direct evaluation of this expansion ill-behaves and is a well-known fact. It is known well that a straightforward evaluation of this expansion is ill-behaved, in this sense that it is not monotonically convergent and it exhibits singularities that cancel out only when an infinite number of terms are re-summed (Ma and Brueckner, 1968). In fact, the result is worsened by first order correction and the second order correction is plagued with divergences (Fetter and Walecka, 1971). The contribution to the correlation term from the gradient arises the largest error in this approximation. Work by Gross and Dreizler (1981) on the expansion of second order exchange density matrix was later re-analyzed and extended by Perdew (1985). Perdew's works are based on theoretical establishments that can recreate a number of exact results in some known limits. This helps to improve some drawbacks of LDA, although this not the case always. The basic idea of GGAs is to express the XC energy in the following form:

$$E_{XC}[n(r)] = \int n(r)\varepsilon_{XC}[n(r)]dr + \int F_{XC}[n(r), \nabla n(r)]dr \quad (2.26)$$

The function F_{XC} has to satisfy the XC holes formal conditions. This cannot be done by considering directly the bare gradient expansion. What is needed for the functional is a form that mimics a re-summation to infinite order and this is the main idea of the GGA, for which there is not a unique recipe. Naturally, not all the formal properties can be enforced at the same time and differentiates one functional from another (Filippi *et al.* 1994).

The main attraction of GGA is its low computational workloads and its abstract simplicity. At present, two GGA functional, suggested by Becke and Perdew (BP) and the other suggested more recently by Perdew and Wang (PW), are the most popular ones in the literature (Perdew *et al.*, 1996). Many calculations assessing the accuracy of the GGA have been reported and they commonly demonstrate the rectification of errors by GGA which the LDA yields in the cohesive energies of solids. Generalized gradient approximations (GGA's) to the exchange-correlation (XC) energy in density-functional theory are at present receiving increasing attention as a straightforward substitute to improve over the local-density approximation (LDA) in *ab initio* total-energy calculations (Kresse and Furthmuller, 1996). The lattice parameters always rise in comparison with the LDA, experimental data are reported closest for *3d*, some *4d* and alkali metals.

2.1.6 Local Spin density approximation (LSDA)

In magnetic systems or, in systems which involve open electronic shells, a much better approximation of the XC functional can be obtained by introducing two spin densities such as $n^\uparrow(\rho(r))$ and $n^\downarrow(\rho(r))$ in LDA to obtained LSDA. The $E_{xc}[n^\sigma(r)]$ energy is a functional of both the spin-up and down spin densities. With such distinction, the Kohn-Sham equation can be written as:

$$\left[-\frac{1}{2}\nabla^2 + V_{KS}^\sigma \right] \phi_i^\sigma(r) = \varepsilon_i^\sigma \phi_i^\sigma(r) \quad (2.27)$$

where V_{KS}^σ and $n^\sigma(r)$ are the spin extension of the previous quantities and

$$V_{KS}^\sigma(r) = v(r) + e^2 \int \frac{\rho(r')}{|r-r'|} dr' + \frac{\delta E_{xc}[n^\uparrow, n^\downarrow]}{\delta \rho^\sigma(r)}$$

$$v(r) = \frac{\delta E_{xc}[n \uparrow, n \downarrow]}{\delta \rho^\sigma(r)}, \rho^\sigma(r) = \sum_i |\phi_i^\sigma|^2, \rho(r) = \sum_\sigma \rho^\sigma(r) \quad (2.28)$$

The XC potential $U_{\sigma xc}(r)$ gives the imbalance between $n \uparrow$ and $n \downarrow$ producing the magnetization $M = n \uparrow - n \downarrow$, which accounts for the different populations $n \uparrow$ and $n \downarrow$ by the derivative. In LSDA, the exchange and correlation contributions are separated as:

$$E_X^{LSDA}[\rho(r)] = \sum_\sigma \int \varepsilon_{XC}^{\text{hom}}(\rho^\sigma(r)) \rho^\sigma(r) dr \quad (2.29)$$

$$E_C^{LSDA}[\rho(r), \xi(r)] = \int \left[\varepsilon_C^U(\rho(r)) + f(\xi(r))(\varepsilon_C^P(\rho(r)) - \varepsilon_C^U(\rho(r))) \right] \rho(r) dr$$

where $\xi(r) = |n \uparrow(\rho(r)) - n \downarrow(\rho(r))| / (n \uparrow(\rho(r)) + n \downarrow(\rho(r)))$ is the normalized magnetization, $f(\xi(r))$ is a smoothing function, ε_C^P and ε_C^U are proper functional representing the correlation energies for the spin-polarized and unpolarized systems, respectively.

2.1.7 The Full-Potential Linearized Augmented-Plane Wave (FP-LAPW) Method

The full-potential linearized augmented-plane wave (FP-LAPW) technique is one among the most precise methods of study of the electronic structures, magnetic and optical properties of crystals and surfaces. The application of atomic forces has greatly maximized its applicability, but it is still commonly supposed that FP-LAPW computations need considerable higher computational effort in comparison with the pseudopotential plane wave (PPW) based techniques. FP-LAPW has recently showed important progress which is evident by use of researchers to work out several properties in magnetism and nuclear quantities, for example, electric field gradients, hyperfine fields, isomer shifts and core level shifts. Nevertheless, because the computational expense and memory requirements are still fairly high, FP-LAPW implementations are

suitable to fairly complicated systems. One successful implementation of the FP-LAPW method is in the program package WIEN2k, a code enhanced by Blaha, Schwarz and coworkers (Blaha *et al.*, 2012). It has been successfully implemented to a various scope of difficulties such as electric field gradients and systems such as high-temperature superconductors, minerals, surfaces of transition metals, or anti-ferromagnetic oxides and even molecules (Ernst *et al.*, 2005). So far the main disadvantage of the FP-LAPW-technique in comparison with the pseudopotential plane-wave (PPW) method has been its higher computational expense. This may be largely because of an inconsistency in optimization efforts spent on both techniques and so we have investigated the FP-LAPW technique from a computational arithmetical viewpoint. Lately, the development of the Augmented Plane Wave (APW) techniques from Slater's APW to LAPW and the new APW+lo was portrayed by Schwarz and Blaha (2003).

FP-LAPW is the one of the most distinct technique for performing calculations on electronic structure of solids and is based on DFT. The valence states are treated relativistically incorporated with either scalar relativistic or with including spin-orbit coupling. Core states are treated fully relativistically. The FP-LAPW technique, like most of the energy-band techniques is a method of solving the K-S equations for the ground state density, total energy and (Kohn-Sham) eigen values (energy bands) of a many-electron system by presenting a basis set which is particularly modified to the problem. This alteration is achieved by partitioning the unit cell (Fig. 2.1.1) into (I) non-overlapping atomic spheres (with its center at the atomic sites) and (II) an interstitial region (i. e. the region between two spheres). In the two sorts of regions, diverse basis sets are used:

i) Inside atomic sphere \mathbf{t} of radius \mathbf{R}_t a linear combination of radial functions times spherical harmonics $Y_{lm}(r)$ is used:

$$\phi_{k_n} = \sum_{lm} [A_{lm} u_l(\vec{r}, E_l) + B_{lm} \dot{u}_l(\vec{r}, E_l)] Y_{lm}(\vec{r}) \quad (2.30)$$

where $u_l(r, E_l)$ is the (at the origin) normal way out of the radial Schrodinger equation for energy E_l and the spherical part of the potential inside sphere, $\dot{u}_l(r, E_l)$ is the energy derived of u_l taken at the similar energy. A linear mixture of these two functions comprise the linearization of the radial function; the coefficients A_{lm} and B_{lm} are functions of k_n decided by requiring that this root function \dot{u}_l goes with the equivalent basis function of the interstitial region; u_l and \dot{u}_l are achieved by numerical integration of the radial Schrodinger equation on a radial mesh inside the sphere.

(ii) In the interstitial zone a plane wave extension is applied

$$\phi_{k_n} = \frac{1}{\sqrt{w}} e^{ik_n r} \quad (2.31)$$

where $k_n = k + K_n$; K_n being the reciprocal and k the wave vector in the first Brillouin zone.

The solutions of K-S equations are extended in this joint basis set of LAPW's according to the linear dissimilarity technique

$$\psi_k = \sum_n C_n \phi_{k_n} \quad (2.32)$$

and the coefficients C_n are decided by the Rayleigh-Ritz variation rule. The union of this basis set is controlled by a parameter $R_{MT} \times K_{max}$, whose value lies between 6 and 9. R_{MT} is the Muffin-Tin radius defined as the radius of the smallest atomic sphere in the unit cell and K_{max} is the largest K vectors magnitude. The linearization can be highly improved

by adding K_n independent basis functions. This addition also improves the treatment of semi, core and the valence electronic states. These independent basis functions are commonly known as “local orbitals” and can be expressed as

$$\phi_{lm}^{LO} = [A_{lm}u_l(\vec{r}, E_{1,l}) + B_{lm}\dot{u}_l(\vec{r}, E_{1,l}) + C_{lm}u_l(\vec{r}, E_{2,l})]Y_l(\hat{r}) \quad (2.33)$$

It consist of a linear combination of two radial functions at two dissimilar energies and one energy derivative. The coefficients A_{lm} , B_{lm} , and C_{lm} , are decided by the necessities that ϕ_{lm}^{LO} should be regularized and has zero value and slope at the sphere border. The general form of potentials in the core region (I) and interstitial region (II) using FP-LAPW technique can be written as

$$V(\vec{r}) = \begin{cases} \sum_{lm} V_{lm}(\vec{r})Y_{lm}(\hat{r}) & \text{inside sphere} \\ \sum_K V_K e^{iKr} & \text{outside sphere} \end{cases} \quad (2.34)$$

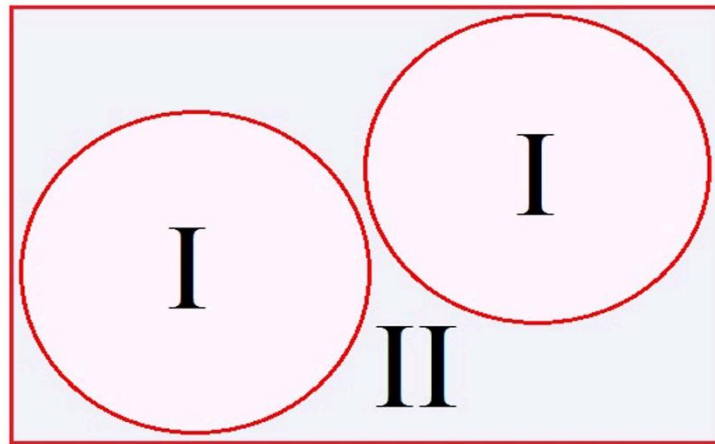


Fig. 2.1.1: Unit cell partitioning into atomic spheres (I) and an interstitial region (II)

2.1.8 Modified Becke Johnson Potential (mBJ)

The LDA and GGA approximations are the standard choice for the exchange–correlation energy to perform calculations on periodic solids within the framework of density functional theory. In many cases, the LDA and GGA functionals (Perdew *et al.*, 1996, 1997) provides consistently good results for the equilibrium and electronic structure of solids. However, the approximation is not error free. The most well-known is the under estimation of the band gap, which is often too small, or even absent, compared to experimental results (Perdew, 1986). The self-interaction error that is contained in the LDA and GGA exchange–correlation potentials is the reason for these band gap discrepancies (Perdew and Zunger, 1981). Many alternative ways exists to determine the experimental band gap. Use of non-multiplicative potential that lies outside the KS framework is a common approach. Hybrid functionals (e.g., HSE (Heyd *et al.*, 2005)) where a fraction of the LDA or GGA exchange is replaced by the exact exchange. This approach is found to improve the band gap largely. However, they are very much computationally expensive and also does not produce satisfactory results in all cases.

Other approach is the LDA+U (Anisimov *et al.*, 1991, 1997) method, but is applicable only to localized and correlated electrons, e.g., $3d$ or $4f$ in transition elements and rare-earth oxides. Very successful but also very expensive methods are the combination of LDA with dynamical mean-field theory (LDA + DMFT) (Georges *et al.*, 1996). If one wants to stay inside the KS framework and still use a computationally cheap semi-local method that leads to KS band gaps which are close to the experimental band gaps, the potential of Becke and Johnson (BJ) (Becke and Johnson, 2006) can be a good starting point.

2.1.9 Equation of States

The behaviour of a solid under hydrostatic pressure can be described by using equation of states which is the pressure-volume or energy volume relation. All physical properties are related to the total energy of the crystal. Equilibrium lattice constant, the isothermal bulk modulus, its pressure derivative etc. are calculated by fitting the calculated total energy to the Murnaghan's equation of state (Murnaghan, 1944), which is given by

$$E(V) = E_0 + \left[\frac{(V_0/V)^{B_0'}}{B_0' - 1} + 1 \right] - \frac{B_0 V_0}{B_0' - 1} \quad (2.35)$$

Here E_0 is the energy minimum at temperature of 0K, V_0 is the equilibrium volume corresponding to minimum energy of the crystal. B_0 and B_0' are the bulk modulus and pressure derivative of the bulk modulus at the equilibrium volume respectively.

$$\text{Pressure } (P) = -\frac{dE}{dV} \text{ and Bulk modulus, } (B_0) = -V \frac{dP}{dV} = V \frac{d^2E}{dV^2}$$

2.1.10 Elastic Constants

In this thesis, the calculation of elastic constant is mainly used for the computation of relaxation time while calculating the thermoelectric properties. Let E_{tot}^0 be the total energy of an initial crystal, and V_0 its volume. By deforming the crystal the energy E_{tot} of the resulting strained state can be expressed as

$$E_{tot} = E_{tot}^0 + P(V - V_0) + \Phi_{elast} \quad (2.36)$$

Here, V is the volume of the strained lattice, Φ_{elast} the elastic energy and the pressure (P) is defined by

$$P = - \left(\frac{\partial E_{tot}^0}{\partial V} \right) (V_0) \quad (2.37)$$

Up to first order elastic constants, the strained and unstrained lattice is related by $(1 + \bar{\varepsilon})$, where 1 is the identity matrix and $\bar{\varepsilon}$ is the strain tensor. According to Hook's law, the linear elastic constants C_{ijkl} are then defined by using the second order development of the elastic energy (Charpin, 2001)

$$\Phi_{elast} = \frac{V}{2} C_{ijkl} \varepsilon_{ij} \varepsilon_{kl} \quad (i, j, k, l = 1, 2, 3)$$

Above equation in Voigt's notation is given by

$$\Phi_{elast} = \frac{V}{2} C_{ij} \varepsilon_i \varepsilon_j \quad (2.38)$$

where $(V - V_0)$ term in Eq. 2.36 is linear with respect to the strain i.e.

$$V - V_0 = V_0 \cdot Tr(\bar{\varepsilon}) = V_0 \sum_{i=1}^3 \varepsilon_i$$

Thus, it is possible to derive elastic constants from the second order derivative of E_{tot} as:

$$C_{ij} = \frac{1}{V_0} \cdot \frac{\partial^2 E_{tot}}{\partial \varepsilon_i \partial \varepsilon_j} \quad (2.39)$$

2.1.11 The WIEN2k Code

The calculations in this work employs the WIEN2k computer code (Blaha *et al.*, 2012). This code contains several sub-programs, few of which are described briefly below. The program contains two major parts, the initialization and the self-consistent field (SCF) cycle. The flow chart of the code is given in Fig. 2.1.2.

- **Initialization** (Setting the unit cell to generate the initial density):

In this sub-program, atomic densities are generated and superimposed to obtain an initial crystal density for the SCF calculation. Additionally, the atomic potentials and

optionally, atomic valence densities are created. Information about l , m values of the lattice harmonics representation and number of Fourier coefficients of the interstitial charge density are inserted as input file in this part (Blaha *et al.*, 2012).

- **LAPW0** (Construction of the effective potential):

This program computes the total potential. Firstly, solution of the Poisson equation is obtained and then the total potential is computed as the sum of the Coulomb and the exchange-correlation potential. The spherical ($l = 0$) and the non-spherical parts of the potential are generated by using electron (spin) density as input. The determination of the Hellmann-Feynman force component, which contributes to the total force is also done.

- **LAPW1** (Solving the Kohn-Sham equations of valence electrons):

The Hamiltonian and the overlap matrix are set up in LAPW1. The eigenvalues and eigenvectors are provided by their diagonalization. The LAPW and the APW+lo method are both supported. The APW+lo basis functions generates l values which are physically meaningful, while LAPW gives higher l -values. Mixing of both the basis functions yields higher efficiency.

- **LAPW2** (Construction of the new electron density):

This program computes the Fermi-energy. The charge density of electrons gets expanded here in accordance to Eq. 2.30. The partial charges that corresponds to the inside of the atomic spheres can be obtained by integration.

- **LCORE** (Treatment of the core electrons):

This program computes the charge density and potential of the core electrons.

- **LMIXER** (Generating the input density for the next iteration):

The total new density is obtained by combining the electron densities of valence, semi-core and core states. The new density can be obtained, ensuring the stability of the SCF cycle by mixing the old and new densities.

$$n_{new}^{m+1} = (1 - \alpha)n_{new}^m + \alpha n_{old}^m \quad (2.40)$$

where α is known as mixing parameter. Broyden scheme is mainly used in WIEN2k code to achieve this. The mixture also computes the atomic forces and total energies. The localized electrons of some systems are strongly correlated and cannot be accurately describes by LDA and GGA methods. Therefore, WIEN2k has the implementation of methods like LDA+U and Orbital polarization. In WIEN2k the LDA+U calculations is based upon effective Coulomb- exchange interaction ($U_{\text{eff}} = U - J$) (Anisimov *et al.*, 1991, 1997). The LDA+U method is excluded in the thesis and will be considered for further works.

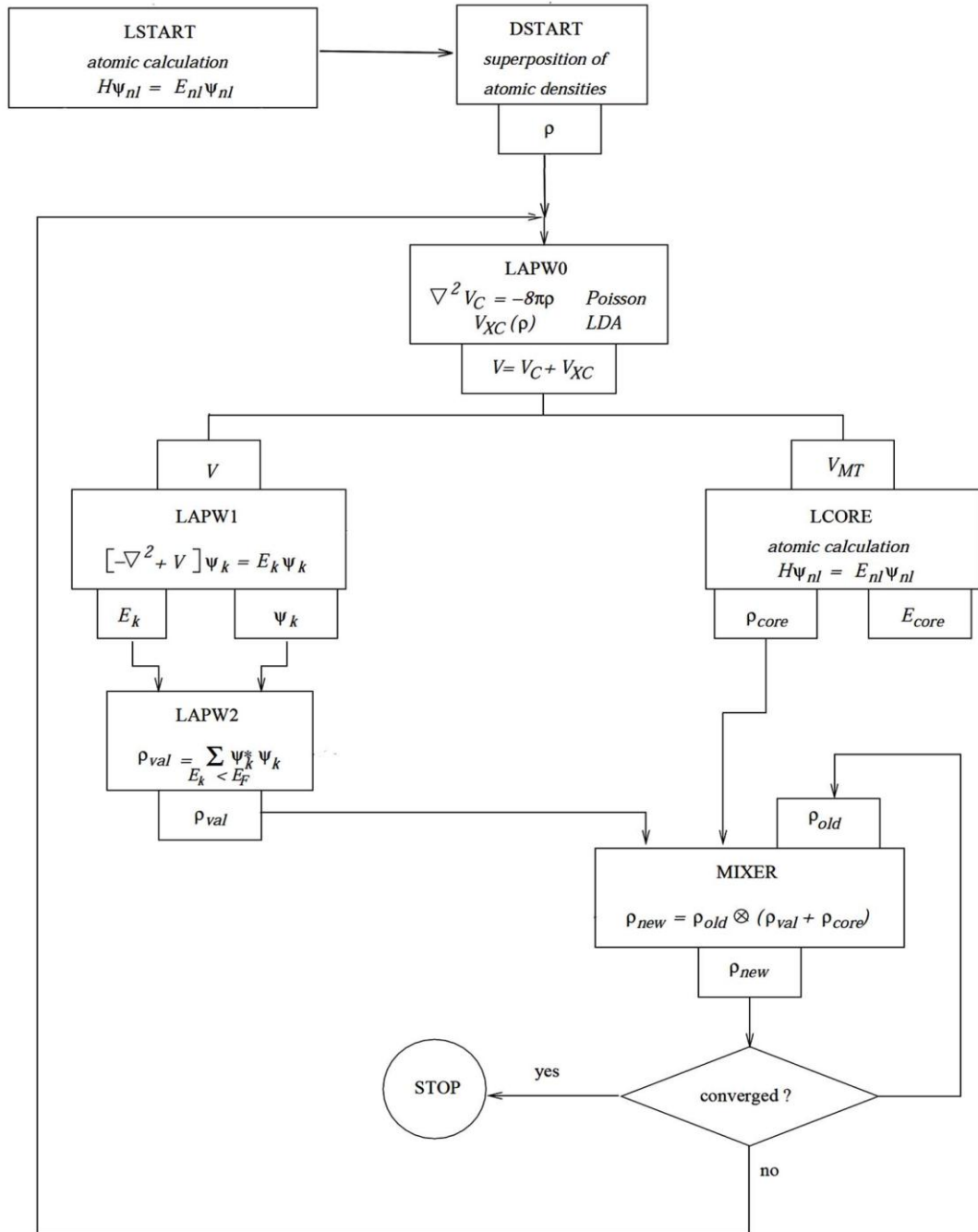


Fig. 2.1.2: Flow chart of WIEN2k code

2.2 Study of Thermoelectric Properties

Thermoelectric investigation requires a post DFT calculation which involves a program cord called BoltzTraP (Madsen and Singh, 2006). The electronic properties obtained after the DFT treatment and the master input files of Wien2K code employed in the electronic structure calculations, acts as the key input for BoltzTraP code.

2.2.1 BoltzTraP (Boltzmann Transport Properties) code

It calculates band structure dependent quantities like electrical conductivity, electronic thermal conductivity, Seebeck coefficient etc. and is based upon the semi-classical Boltzmann transport theory (Allen, 1996). The code employs the rigid band approximation and assumes the relaxation time (τ) to be a directional independent constant. According to this approximation, the band structure of a material remains unchanged with the application of temperature, changing only the chemical potential of the material. This approximation holds good for low doping levels and are found to yield results close to the experimental results (Madsen and Singh, 2006).

The solution of the semi-classical Boltzmann equations are obtained by performing Fourier interpolation of the band energies which yields the conductivity tensor and the other transport coefficients. The electrical conductivity tensor is expressed as

$$\sigma_{\alpha,\beta} = e^2 \sum_{i,j} \left[-\frac{\partial f_0(T, \varepsilon, \mu)}{\partial \varepsilon} \right] v_{\alpha} v_{\beta} \tau \quad (2.41)$$

Here, α and β denotes tensor indices, v_{α} and v_{β} are the group velocities, e is the electronic charge and f_0 is the Fermi- Dirac distribution function. The electrons contribute in a range of $\mu - k_B T < \varepsilon < \mu + k_B T$, near the chemical potential (μ) (Yamamoto *et al.*, 2014).

The transport distribution can then be expressed as the kernel of the transport coefficients (Mahan and Sofo, 1996) given by-

$$\Xi_{i,k} = \sum_{i,k} v_{\alpha} v_{\beta} \tau_k \quad (2.42)$$

Thus, the Seebeck coefficient (S), the electronic thermal conductivity (κ_e) and the electrical conductivity (σ) can be obtained as a function of chemical potential (μ) and temperature (T) by integrating the following expressions-

$$\sigma = e^2 \int \Xi_{i,k} \left[-\frac{\partial f_0(T, \varepsilon, \mu)}{\partial \varepsilon} \right] d\varepsilon \quad (2.43)$$

$$\kappa_e = k_B^2 T \int \Xi_{i,k} \left(\frac{\varepsilon - \mu}{k_B T} \right)^2 \left[-\frac{\partial f_0(T, \varepsilon, \mu)}{\partial \varepsilon} \right] d\varepsilon \quad (2.44)$$

$$S = \frac{ek_B}{\sigma} \int \Xi_{i,k} \left(\frac{\varepsilon - \mu}{k_B T} \right) \left[-\frac{\partial f_0(T, \varepsilon, \mu)}{\partial \varepsilon} \right] d\varepsilon \quad (2.45)$$

One of the demerits of BoltzTraP is that the transport properties are obtained as a function of relaxation time and there is no provision, what so ever, to compute the unknown relaxation time. The calculated thermoelectric parameters from BoltzTraP like the electrical conductivity (σ) and the electronic thermal conductivity (κ_e) are relaxation time dependent. The Seebeck coefficient (S) is independent of τ . One of the assumption made in the code is that, τ is an energy independent constant equal to 0.8×10^{-14} seconds. However, relaxation time highly depends upon the nature of the material and considering a fixed value of τ would highly affect the precision of the calculated transport properties. In general, we believe that the order of τ assumed in the code, holds only for higher temperatures as relaxation time would be low at higher temperatures. Owing to the law of conservation of momentum, for lower temperatures, the order of τ for most materials has to be high. Therefore, we have made an attempt to calculate the relaxation time (τ)

and has been calculated based upon the deformation potential theory of Bardeen and Shockley (Bardeen and Shockley, 1950)

2.2.2 Computation of Relaxation time (τ)

The relaxation time is calculated as a function of temperature using the expression given by Xi and coworkers (Xi *et. al.* 2012).

$$\tau = \frac{2\sqrt{2\pi} \hbar^4 C_\beta^{3D}}{3E_\beta^2 (m^* k_B T)^{3/2}} \quad (2.46)$$

Here, C_β^{3D} is the elastic constants of 3D systems and is given by, $C_\beta^{3D} = \frac{1}{V_0} \frac{\partial^2 E}{\partial(\delta a_0 / a)^2}$

with E = Energy, a_0 = equilibrium lattice constant along the direction β and V_0 = equilibrium volume. C_β^{3D} was calculated within the DFT framework, as explained in

section 2.1.10, using the code Elastic (Golesorkhtabar *et. al.*, 2013). The parameter E_β is

the coefficient of deformation potential along the direction β and is defined as $\frac{\partial E}{\partial s}$,

where s is the strain given by $s = \frac{\Delta a}{a_0}$, ($\Delta a = a - a_0$) and a_0 the equilibrium lattice

constant. ∂E is calculated as the energy change in conduction band minimum (CBM)

(for n -type material) or the energy change in the valence band maximum (VBM) (for p -

type material) with the application of strain. The change in the band edge energy is fitted

in a linear manner using the equation of the straight line given by-

$$E = ms + c \quad (2.47)$$

Where, m and c are constants known as the slope and intercept respectively, of the straight line.

The slope m in equation 2.47 gives the coefficient of deformation potential, which is obtained by differentiating 2.47 with respect to the strain s , such that $\frac{\partial E}{\partial s} = m = E_{\beta}$.

The effective mass, m^* was calculated by the parabolic fit of the wave vector (K) vs energy (E) of the CBM or the VBM, depending upon the nature of the charge carriers and is determined by the expression (Singh *et. al.*, 2016)-

$$m^* = \frac{\hbar^2}{dE^2 / dK^2} \quad (2.48)$$

The E vs K plot is fitted according to a second order polynomial fit using the equation

$$E = AK^2 + BK + C \quad (2.49)$$

Here, A , B and C are constants. The second order derivative of equation 2.49, with respect to K gives dE^2 / dK^2 .

The relaxation time is calculated with respect to temperature (T) and the relaxation time dependent electrical conductivity (σ/τ) and the electronic thermal conductivity (κ_e/τ), calculated from BoltzTraP is finally made τ independent as $\sigma = \sigma/\tau \times \tau$ and $\kappa = \kappa_e/\tau \times \tau$.

2.2.3 Computation of Lattice thermal conductivity (κ_p)

The maximum thermoelectric efficiency condition known as the Figure of Merit (ZT) is the most important parameter involved in the calculation of efficiency. It is given in accordance to equation 1.10 by

$$ZT = \frac{S^2 \sigma T}{\kappa_e + \kappa_p} \quad (2.50)$$

As already mentioned, Seebeck coefficient (S) and the relaxation time dependent electrical conductivity (σ) and electronic thermal conductivity (κ_e) is calculated using BoltzTraP code. However, BoltzTraP cannot compute the phononic contribution to

thermal conductivity (κ_p) and therefore we have obtained it by solving the Slack's equation (Morelli and Slack, 2006)

$$k_p = A \frac{\overline{M} \Theta_D^3 \delta^{1/3}}{\gamma^2 n^{2/3} T} \quad (2.51)$$

Here, \overline{M} is the average Molecular weight, Θ_D the Debye's temperature, δ the equilibrium volume, γ is the Grüneisen parameter, n is the number of atoms per unit cell and T is the absolute temperature. A is a coefficient dependent upon γ in units of W mol/kg/m²/K³.

Debye's temperature (Θ_D) and the Grüneisen parameter γ are calculated in the framework of quasi-harmonic Debye model (Blanco *et. al.*, 2004) as implemented in the Gibbs2 package (Otero-de-la-Roza *et. al.*, 2011). The most severe defect of the Harmonic approximation is the independency of the temperature and geometry of the system. This means that in the frame work to this assumption, thermal expansion of a system cannot be explained as the distance between the atoms in a crystal is independent of temperature. The quasiharmonic approximation in turn assumes the volume dependence of phonon frequencies, to achieve the volume and temperature dependence such that the thermal expansion of a crystal can be predicted. In the framework of quasiharmonic approximation, from Debye's model, the Gibbs function can be defined as

$$G^*(V; P, T) = E(V) + PV + A_{vib}(\theta_D(V); T) \quad (2.52)$$

$E(V)$ is the total energy per unit cell, PV denotes constant pressure, $\theta_D(V)$ is the Debye temperature and A_{vib} is the vibrational parameter expressed by

$$A_{vib}(\theta_D, T) = nk_B T \left[\frac{9\theta}{8T} + 3 \ln(1 - e^{-\theta/T}) - D\left(\frac{\theta_D}{T}\right) \right] \quad (2.53)$$

where, $D\left(\frac{\theta_D}{T}\right)$ is the Debye integral. The Debye temperature θ_D for an isotropic solid can therefore be expressed as

$$\theta_D = \frac{\hbar}{k_B} (6\pi V^{1/2} n)^{1/3} f(\sigma) \sqrt{\frac{B}{M}} \quad (2.54)$$

$f(\sigma)$ is a function dependent on the Poisson's ratio (σ) defined as

$$f(\sigma) = \left[3 \left\{ 2 \left(\frac{2(1+\sigma)}{3(1-2\sigma)} \right)^{3/2} + \left(\frac{(1+\sigma)}{3(1-\sigma)} \right)^{3/2} \right\}^{-1} \right]^{1/3} \quad (2.55)$$

Thus, the Gibbs free energy is obtained with respect to volume at constant temperature and pressure as-

$$\left[\frac{\partial G^*(V; P, T)}{\partial V} \right]_{P, T} = 0 \quad (2.56)$$

Therefore, the Debye integral can now be defined by,

$$D\left(\frac{\theta_D}{T}\right) = \frac{3}{(\theta_D/T)^3} \int_0^{\theta_D/T} \frac{x^3}{e^x - 1} dx \quad (2.57)$$

The Grüneisen parameter (γ) is computed as

$$\gamma = - \frac{d \ln \theta_D(V)}{d \ln V} \quad (2.58)$$

Finally ZT is computed by using equation 2.50 by combining the results obtained after solving Slack's equation and after making the transport parameters obtained from Boltzmann transport equation τ independent.

Chapter 3:

***Electronic and
Thermoelectric Properties
of Half-Heusler MCoSb
(M=Ti, Zr and Hf)***

Electronic and Thermoelectric Properties of Half-Heusler MCoSb (M=Ti, Zr and Hf)

In this chapter the electronic and thermoelectric investigation of three HH compounds TiCoSb, ZrCoSb and HfCoSb is shown. We have investigated these three compounds in order to compare our theoretical results with the available experimental and theoretical results. To obtain a better description of the electronic structure and thermoelectric properties, the crystal structure of the three compounds has been optimized such as to calculate the equilibrium volume and the lattice constants. Structure optimization based upon Murnaghan's equation of state was performed to obtain the relaxed structure with minimum energy. The lattice constants obtained as a result of optimization is then used for calculations of electronic and thermoelectric properties.

3.1. Structural Optimization

The half-Heusler MCoSb crystallizes in MgAgAs type structure, possessing cubic phase with space group $F\bar{4}3m$ (Sun *et al.*, 2015). The unit cell of MCoSb consists of four formula units with M, Co and Sb atoms located at the Wyckoff positions $4c$: (0.25, 0.25, 0.25); $4a$: (0, 0, 0) and $4d$: (0.75, 0.75, 0.75), while the $4b$ (0.5, 0.5, 0.5) position is vacant (Stadnyk *et al.*, 2001). Its unit cell structure is shown in Fig. 3.1 (a). Some previous studies had reported that MCoSb compounds crystallizes in AlLiSi type structure (Melnyk *et al.*, 2000). Also, MgAgAs type structure can have Wyckoff positions $4a$:

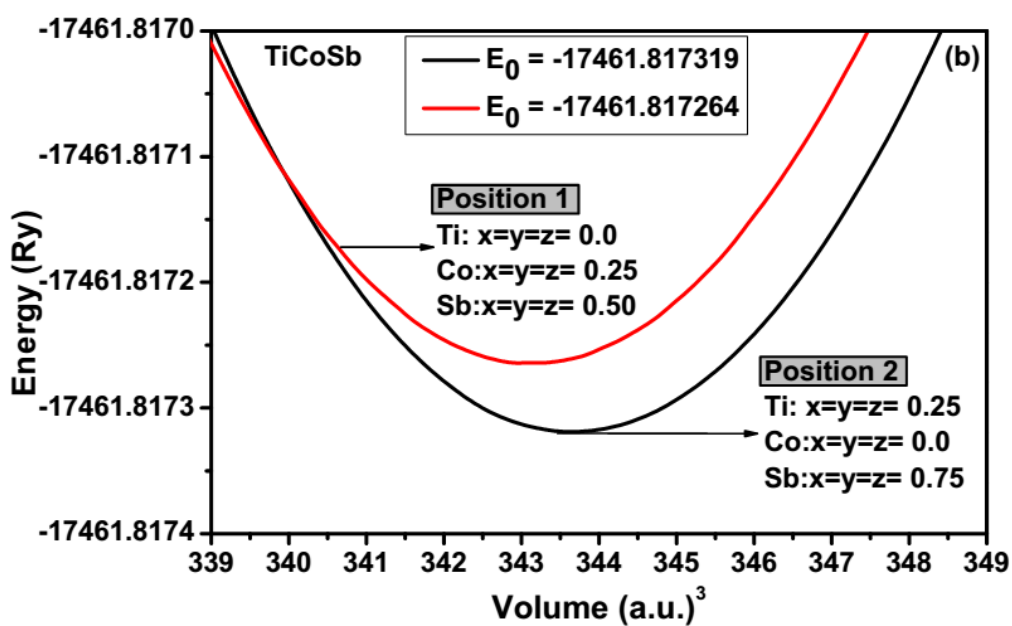
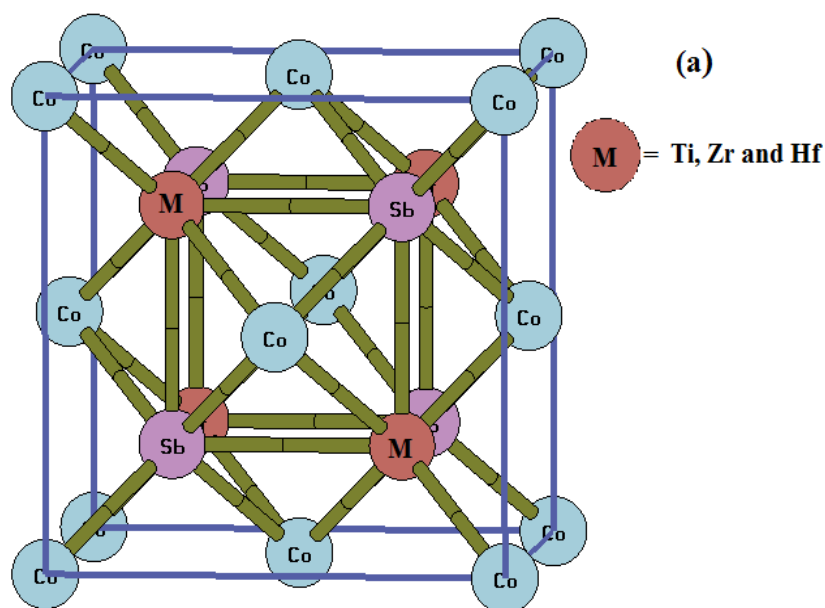
(0,0,0); 4c: (0.25, 0.25, 0.25) and 4b: (0.5, 0.5, 0.5), with the 4d (0.75, 0.75, 0.75) position empty (Offernes *et al.*, 2007 and Kaur *et al.*, 2017). Thus, a simple investigation is made to find the most favorable structure. It is done by fitting for both the positions the Energy vs Volume curve with respect to Murnaghan's equation of state (Murnaghan *et al.*, 1994) given by equation

$$E_{tot}(V) = \frac{B_0 V}{B_0^* (B_0^* - 1)} \left[\left(\frac{V_0}{V} \right)^{B_0^*} + B_0^* \left(1 - \frac{V_0}{V} \right) - 1 \right] + E_0$$

Where the symbols have their usual meaning and is described in Chapter 2. The energy vs volume curves are shown in Fig. 3.1 (b), 3.1 (c) and 3.1 (d). The curves are fitted for two positions of MCoSb (M = Ti, Zr, Hf). Position 1: M = (0, 0, 0); Co = (0.25, 0.25, 0.25); Sb = (0.5, 0.5, 0.5), Position 2: M = (0.25, 0.25, 0.25); Co = (0, 0, 0); Sb = (0.75, 0.75, 0.75). The position with lowest equilibrium energy would be the most favorable position in nature and would correspond to a stable structure (Wang *et al.*, 2009).

It was found that the minimum energy corresponds to position 2 and therefore all calculations done for MCoSb are considering this structure. After performing the volume optimization it gives equilibrium lattice constant, bulk modulus, its pressure derivative etc. as output. The lattice constants calculated are respectively 5.8839 Å, 6.0912 Å and 6.0574 Å for TiCoSb, ZrCoSb and HfCoSb. The obtained lattice constants values are compared with the available theoretical and experimental results of Sekimoto *et al.*, 2005, Stadnyk *et al.*, 2001, Wang *et al.*, 2009 and Yuan *et al.*, 2017. The experimental obtained values are found to be in close match with our calculated results and are presented in table 3.1. The EOS fitting overestimates the lattice constant by 0.034 %, 0.38 % and 0.28 % in an average respectively for TiCoSb, ZrCoSb and HfCoSb, when compared with the available experimental data. The higher values in the calculated result is because of the

choice of functional used for optimization. Structure optimization are based upon GGA XC functional and several authors (Haas *et al.*, 2009 and Zoroddu *et al.*, 2001) have reported the overestimation of lattice parameters when GGA is employed. The over estimation by GGA can be upto ~9%. However, GGA is still preferred over LDA for optimization of lattice parameters, where it was found to underestimate the parameters on comparison with the experimental results. The overestimation by GGA and the underestimation by LDA also highly depends upon the type of solid under study (Haas *et al.*, 2009). The calculated structure parameters are listed in table 3.1.



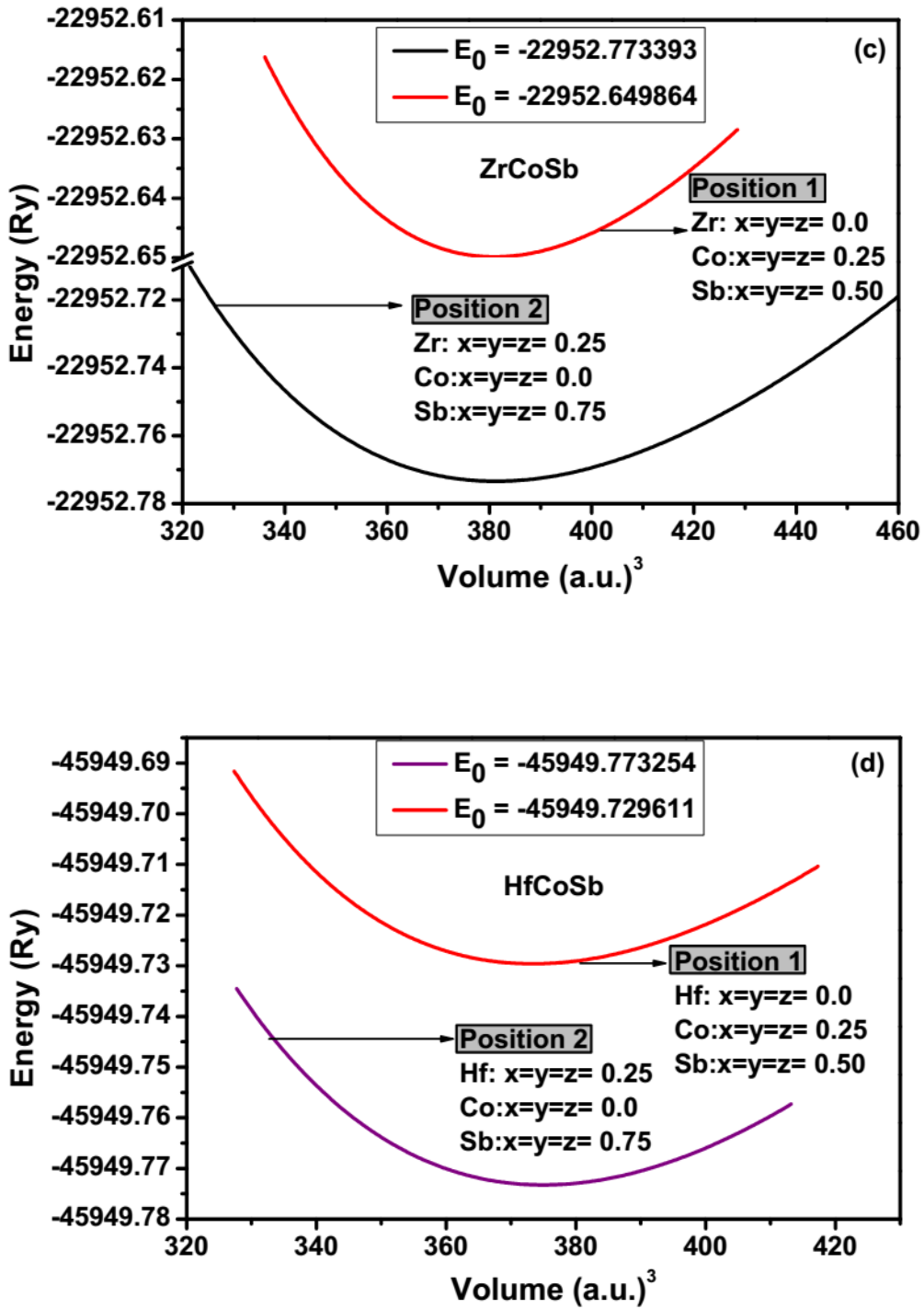


Fig. 3.1: (a) Unit cell structure of MCoSb (M=Ti, Zr and Hf), (b) Volume optimization curve for TiCoSb, (c) ZrCoSb and (d) HfCoSb, fitted using the Murnaghan's equation of state.

Table 3.1: Lattice constants (a), Bulk modules (B) and pressure derivative of bulk modules (B') obtained using Murnaghan's equation of state.

Compounds	Lattice constant (a) Å		B (GPa)	B'	References
	Previous result	Calculated result			
TiCoSb	5.90	5.8839	146.914	4.5942	Wang <i>et al.</i> (Theo.)
	5.8845				Sekimoto <i>et al.</i> (Expt.)
	5.8819				Stadnyk <i>et al.</i> (Expt.)
ZrCoSb	6.0700	6.0912	139.8650	4.8515	Sun <i>et al.</i> (Theo.)
	6.0650				Sekimoto <i>et al.</i> (Expt.)
	6.0648				Yuan <i>et al.</i> (Expt.)
HfCoSb	6.0541	6.0574	145.1177	4.9312	Lee <i>et al.</i> (Theo.)
	6.040				Morelli <i>et al.</i> (Theo.)
	6.0411				Sekimoto <i>et al.</i> (Expt.)

3.2. Electronic properties

The electronic properties are investigated using the lattice constants obtained after performing the volume optimization. The obtained TDOS, PDOS and the electronic band structures are calculated employing both GGA and mBJ approximations for all of MCoSb and are shown in Fig. 3.2.1 to 3.2.5.

From the TDOS Fig. 3.2.1, it can be seen that the difference the plots with respect to GGA exchange correlation and mBJ potential is very little. However, with mBJ, most of the DOS peaks are reduced slightly and are shifted towards higher energy ranges by a very little amount. The shifts are more distinguished towards the conduction region. DOS has a functional dependence on energy and mBJ being only a potential, has no corresponding energy functional dependence. Whereas, GGA includes orbital energy obtained from self-consistent calculations, such that DOS results depends strongly on the energy exchange correlation functional. Thus, due to this reason, the mBJ DOS peaks are slightly lower than that obtained from GGA approximation. Near the Fermi level (E_F), both approximations give sharp peaks and also indicates the absence of pseudogap in the compound MCoSb since no DOS exists at E_F .

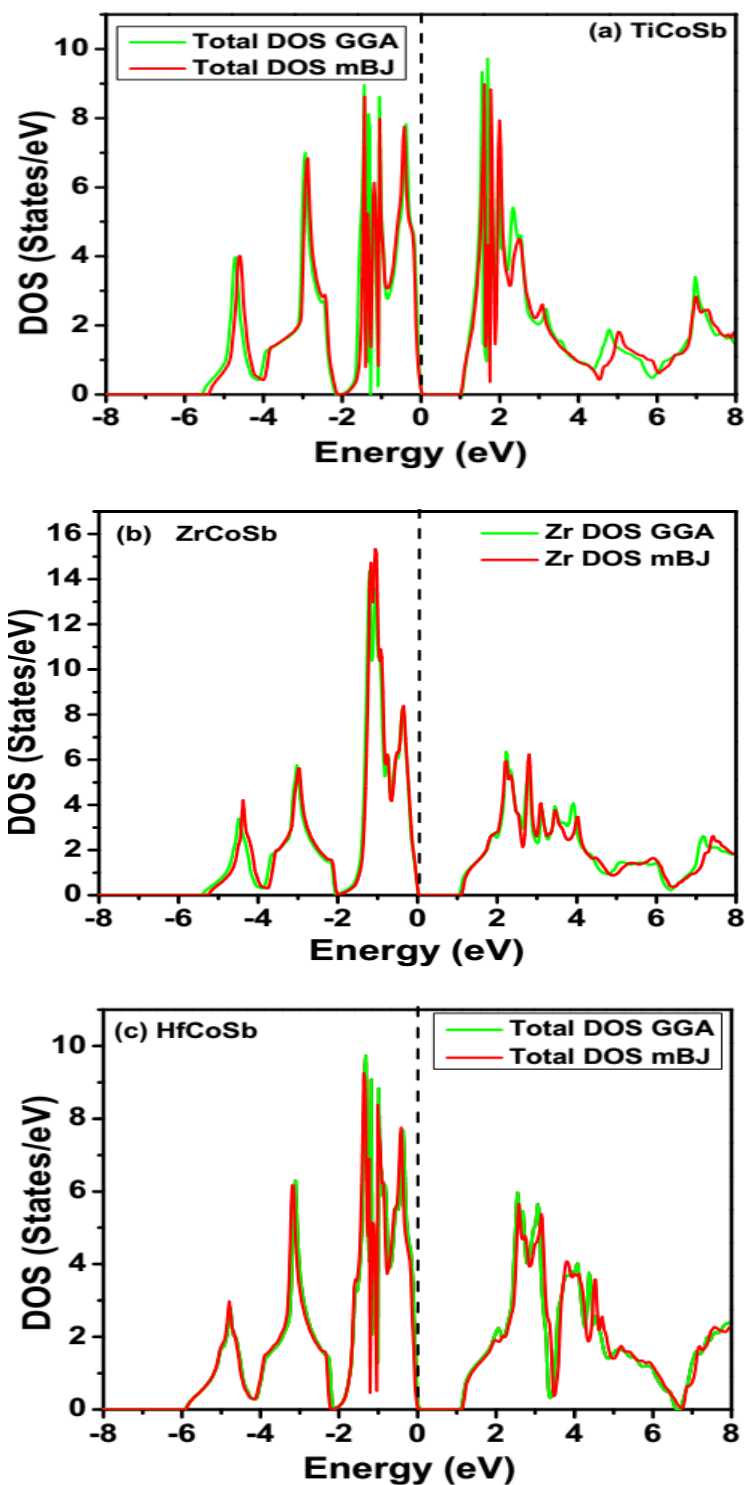


Fig. 3.2.1: Total DOS of (a) TiCoSb, (b) ZrCoSb and (c) HfCoSb (Green-GGA, Red-mBJ).

From the partial DOS plots, Fig. 3.2.2 to 3.2.4, it is observed that the atom that contributes the most to the total DOS of MCoSb is the Co. In all of TiCoSb, ZrCoSb and HfCoSb HH compounds, the atom Sb shows the least contribution to the total DOS. This implies that the maximum number of atomic states available for occupation is that of Co. For simplicity and to ease the explanation of partial DOS, we have divided the DOS valence region into the following category: lower valence region (between -8eV to -6 eV), middle valence region (between -6 eV to -4 eV), upper valence region (between -4 eV to 0 eV). Similarly, the conduction region is also divided as the lower conduction region (between 1 eV to 4 eV) and upper conduction region (between 4 eV to 8 eV). Fig. 3.2.2 (d-e) shows that Ti-3*d* and Co-3*d* states contributes the most to the total DOS of TiCoSb. No contribution is observed from the lower valence region in TiCoSb. Mixed DOS are noted in decreasing order from Co-3*d*, Ti-3*d* and Sb-5*p* states in the middle valence region.

In the upper valence region high peaks are observed at 1 eV and 1.5 eV, and is dominated by the 3*d* states of atom Co. Moderate contribution <1.5 states/eV is observed from 3*d* states of atom Ti and a very small (~0.54 states/eV) contribution is seen from Sb-5*p* states. Strong dominance of Ti-3*d* (*d-e_g*, *d-t_{2g}*) states contributing upto ~5 states/eV is noteworthy in the lower conduction region. Almost no contribution from Co and Sb atoms is noticed in upper conduction region. Therefore, total DOS in the conduction region is mainly due to 3*d* states of Ti atom in half-Heusler TiCoSb. Similar DOS characteristics are observed for ZrCoSb (Fig. 3.2.3) and HfCoSb (Fig. 3.2.4), except that for both these compounds, the conduction region is completely dominated by the 3*d* (*d-e_g*, *d-t_{2g}*) states of Zr and Hf atoms respectively.

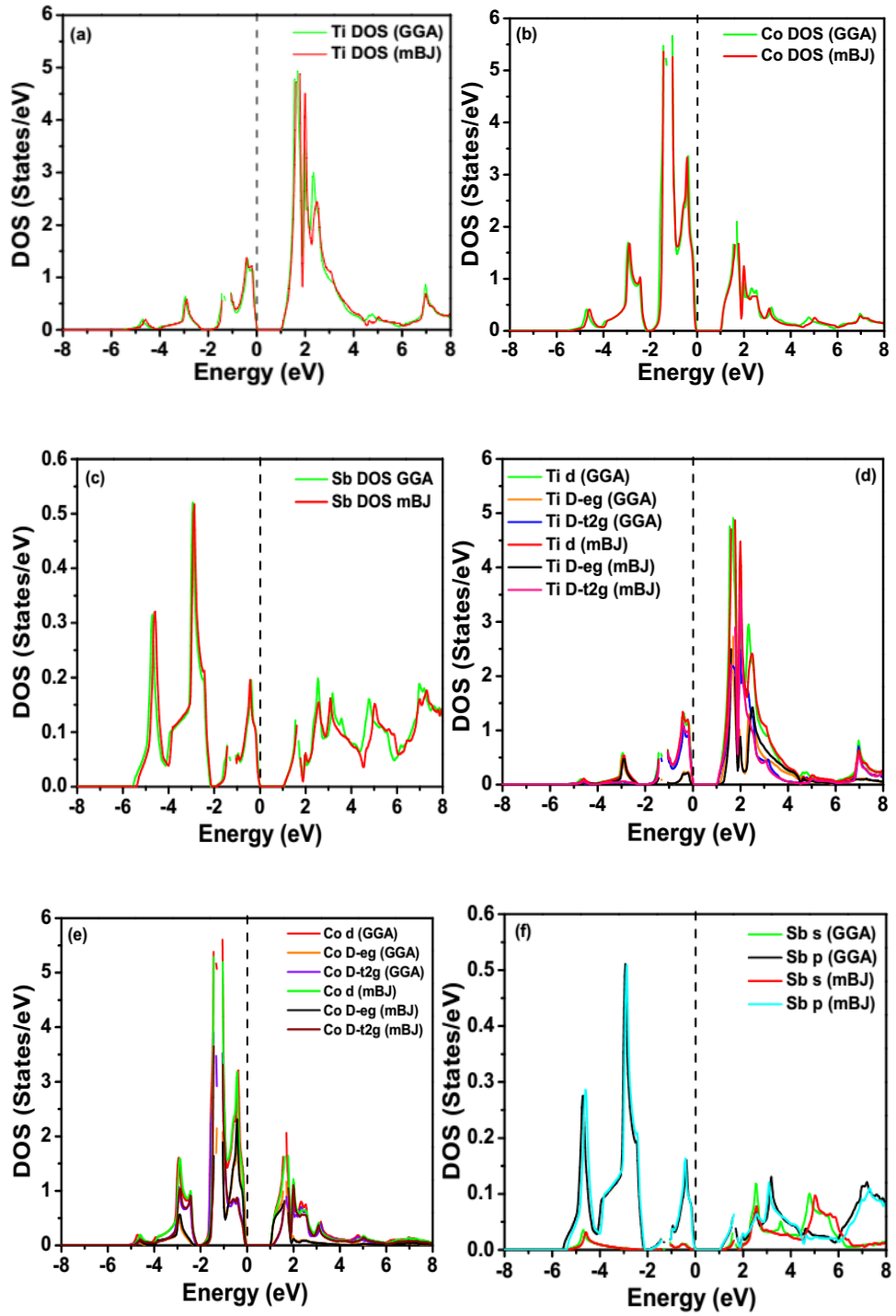


Fig. 3.2.2: Partial DOS plot of TiCoSb (a) Ti contribution, (b) Co contribution, (c) Sb contribution, (d) d -states of Ti, (e) d -states of Co and (f) p -states of Sb (Green-GGA and red-mBJ).

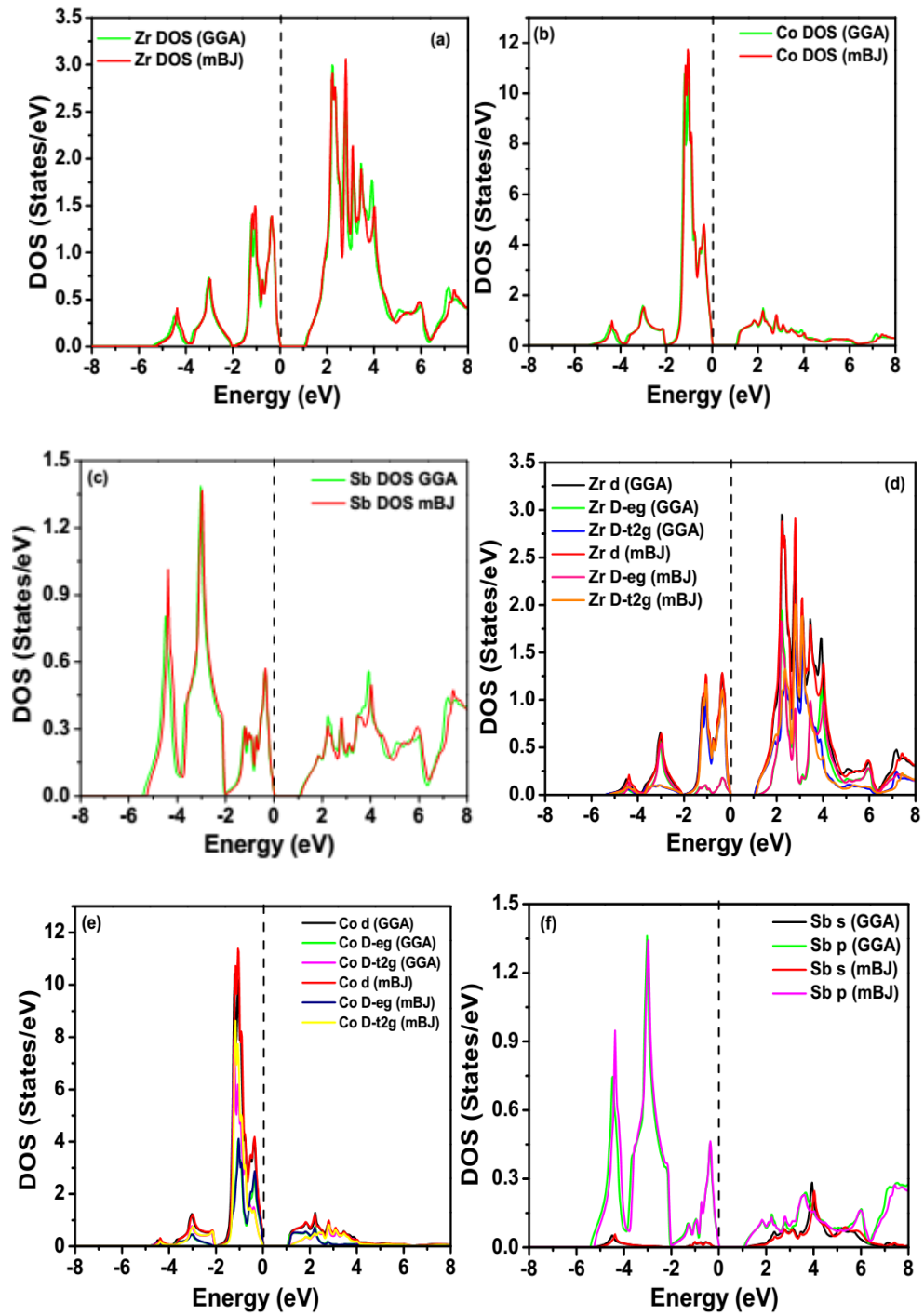


Fig. 3.2.3: Partial DOS plot of ZrCoSb (a) Zr contribution, (b) Co contribution, (c) Sb contribution, (d) d -states of Zr, (e) d -states of Co and (f) p -states of Sb (Green-GGA and red-mBJ).

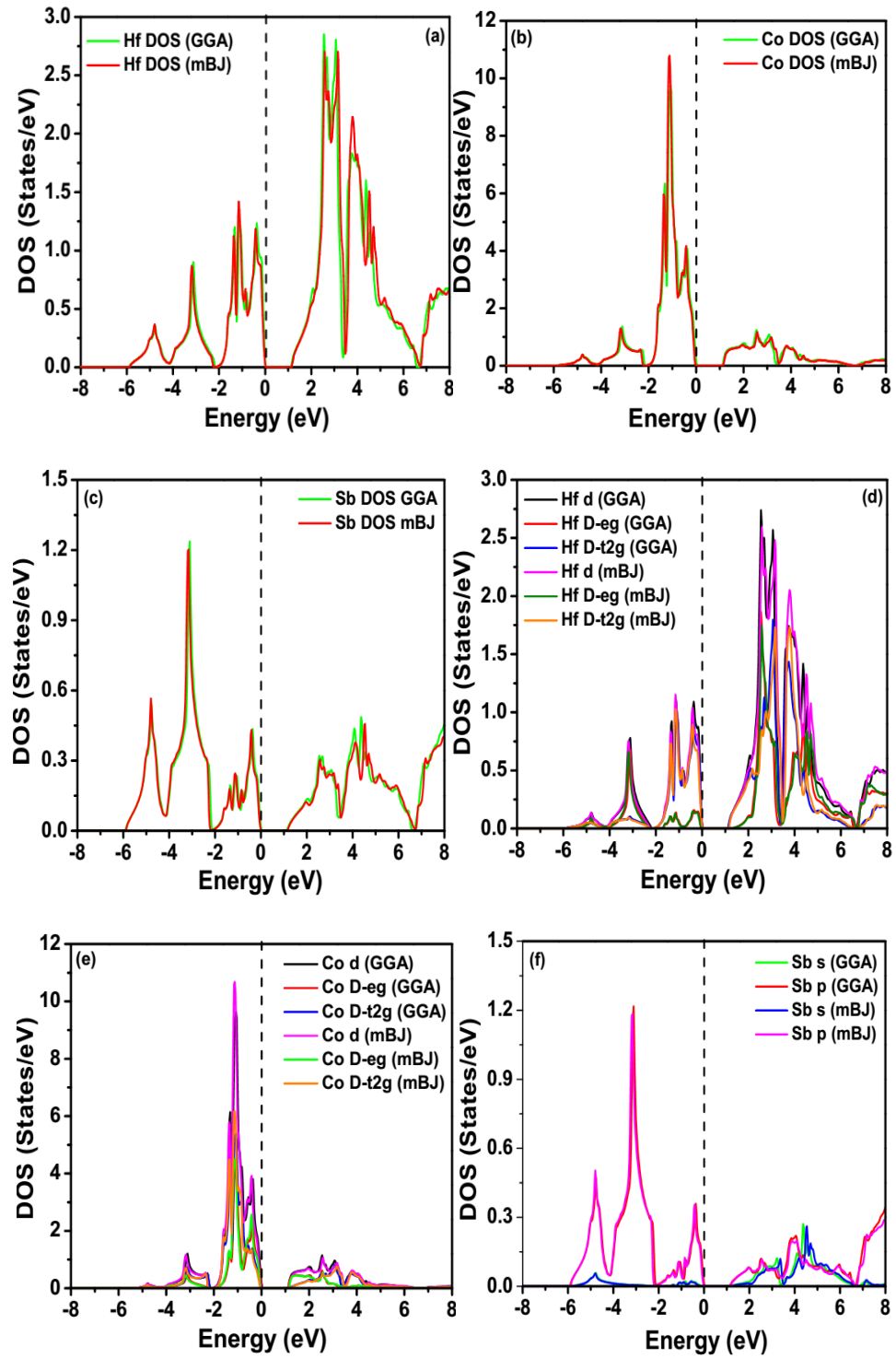


Fig. 3.2.4: Partial DOS plot of HfCoSb (a) Hf contribution, (b) Co contribution, (c) Sb contribution, (d) d -states of Hf, (e) d -states of Co and (f) p -states of Sb.

Thus, the high DOS peaks in the conduction region of HH MCoSb is due to the *d*-states of M atom (M=Ti, Zr and Hf) and that in the valence region is mainly due to the *d*-states of Co atom.

The band structure of MCoSb is plotted along high symmetry directions *W-L- Γ -X-W-K* in the irreducible part of Brillouin zone (Fig. 3.2.5). The Fermi level is set to be at zero energy. These compounds exhibit narrow band gaps and are characterized as narrow band semiconductors. In the Fig. red lines denotes the band structure plot from mBJ approximation, while the green lines are those from GGA. TiCoSb and HfCoSb has the valence band maxima on the symmetry point Γ and the conduction band minima on the symmetry point X. Thus, indirect band gaps along Γ -X direction is observed in both the compounds. ZrCoSb has a shift on the valence band maxima to the symmetry point L, while the conduction band minima remains at the symmetry point X. An indirect band gap along L-X symmetry direction is observed. Similar trends in the band gap had been reported in the previous literature (Sun *et al.*, 2005 and Lee *et al.*, 2011). The band gap values obtained from GGA and mBJ approximation are quiet close to one another with gaps from mBJ being slightly higher. The energy band gaps obtained from both approximations are presented in table 3.2, where a comparison between the calculated and the available theoretical and experimental results are also made. The highest band gap value obtained under GGA scheme was that for HfCoSb (1.137 eV) and the lowest for TiCoSb (1.04 eV). These obtained values are in close agreement with the available theoretical results (references are shown in table 3.2). However, huge deviation from the experimental values were found. The discrepancy is attributed to the temperature influence. The band gap values that we report are observed at 0 K, whereas the values reported in experiments are observed in the temperature range of 300 K – 900 K. The

obtained values of band gap varies as $\Delta E_G(\text{TiCoSb}) < \Delta E_G(\text{ZrCoSb}) < \Delta E_G(\text{HfCoSb})$. The improvement of the band gap under mBJ scheme is almost negligible and it can be said that the calculation of electronic structure with mBJ potential for MCoSb ((M=Ti, Zr and Hf)) is ineffective. Several authors (Heyd *et al.*, 2003 and Rai *et al.*, 2016) has reported the inefficiency of mBJ potential on narrow band gap HH compounds. Even highly sophisticated hybrid functional proposed by Heyd-Scuseria-Enzerhof (HSE06) may have negligible effect on the band gap of such type of semiconductors (Rai *et al.*, 2016). The values of the band gaps calculated from mBJ potential are reported for the first time, to the best of my knowledge, for these HH compounds.

In the upper valence band region (0 eV to -4 eV), threefold degenerate bands are observed at the Γ point, whereas a twofold degenerate bands exists at L point. The bands just above -2 eV at the Γ point does not participate in carrier transport directly, but its position affects the transport properties associated with the valence band (Lee *et al.*, 2011). These bands are mainly formed due to the d orbitals (dt_{2g}) of Co atoms. Other bands seen at the top of the valence band at the same symmetry point comes from the hybridization of d_{eg} and dt_{2g} orbitals of M and Co atoms (M = Ti, Zr, Hf) (Lee *et al.*, 2011). The band structure also reveals the dopant characteristics of the material, ZrCoSb will be more suitable to dope with p -type impurity instead of the n -type. This is because, the VBM for ZrCoSb lies in the L -symmetry point instead of Γ as in case of TiCoSb and HfCoSb, which will be more effective towards n -type dopant (Lee *et al.*, 2011).

Similar type of band characteristics is found for all of MCoSb HH compound. Here also we have divided the conduction band into two regions for simplicity, the lower conduction band (between 0 to 4 eV) and the upper conduction band (between 4 to 8 eV). In the lower conduction band at the Γ point (near about 2 eV) for ZrCoSb and HfCoSb, a

rapid dispersion downwards towards the X point is observed. The dispersion continues until it flattens out at the X symmetry point. This increases the effective mass of electron, near the conduction band minima, along the $X-\Gamma$ direction (Gibbs *et al.*, 2017). This band is a result of hybridization between the dt_{2g} states of M atom and the de_g states of Co atom. The sharp peaks at the Γ point in the lower conduction band region (near about 4 eV) are due to the s orbitals of Sb atom (Lee *et al.*, 2011). The bands originating at the upper conduction band region is mainly due to the d states of M atom and p states of Sb atom. Thus the origin of band gap in HH MCoSb can be explained as, due to the hybridization of dt_{2g} orbitals of M atom and p orbitals of Sb atom with de_g orbitals of Co atom (Cottenier, 2002).

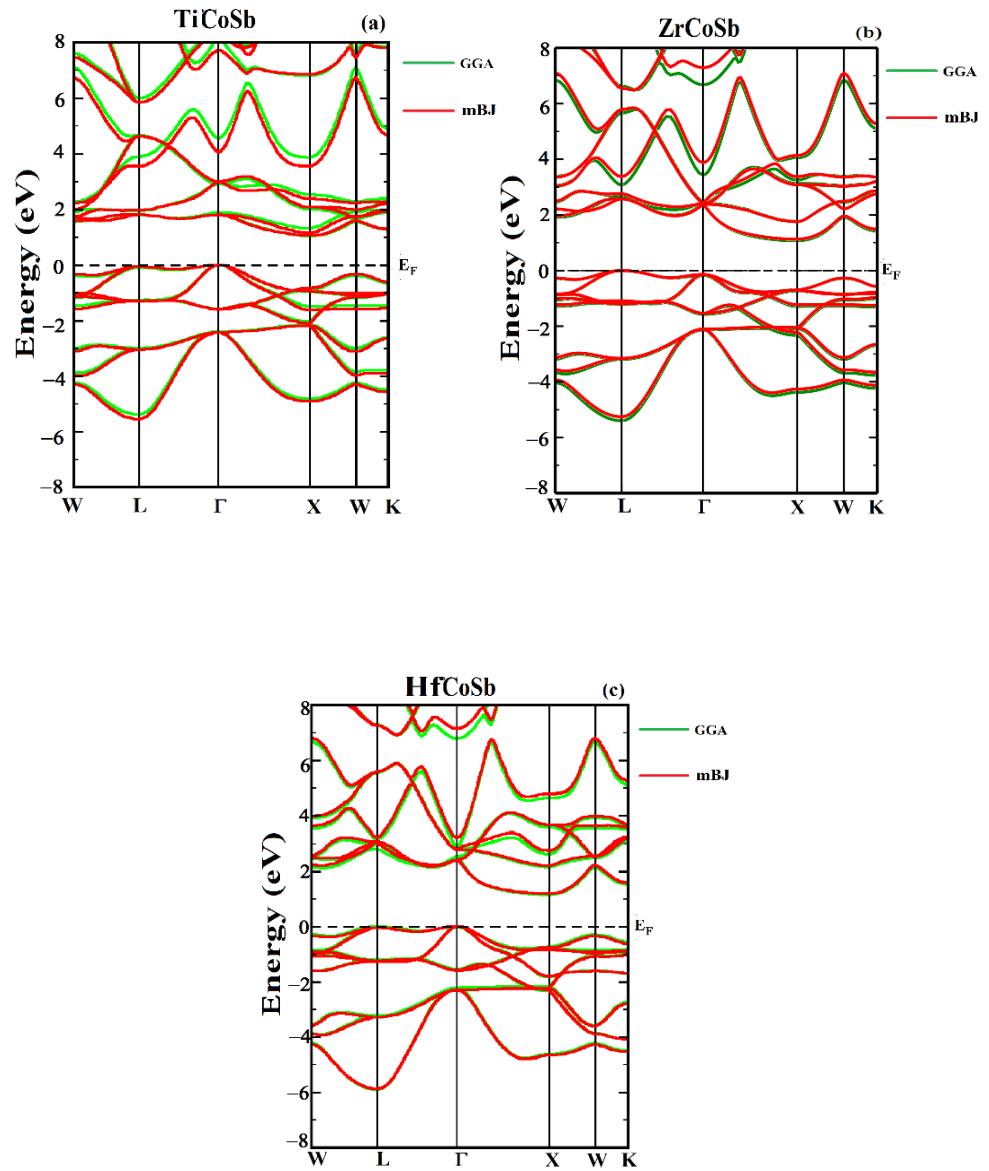


Fig. 3.2.5: Electronic band structure of (a) TiCoSb, (b) ZrCoSb and (c) HfCoSb (Green-GGA and red-mBJ).

Table 3.2: Calculated band gap for TiCoSb, ZrCoSb and HfCoSb

Compounds	Energy Gap (eV)			References
	Previous result (GGA)	Calculated result (GGA)	mBJ	
TiCoSb	1.05	1.04	1.057	Sun <i>et al.</i> (Theo.)
	1.06			Singh <i>et al.</i> (Theo.)
	0.95			Xia <i>et al.</i> (Expt.)
ZrCoSb	1.061	1.073	1.13	Sun <i>et al.</i> (Theo.)
	1.0650			Zoroddu <i>et al.</i> (Theo.)
	0.14			Sekimoto <i>et al.</i> (Expt.)
HfCoSb	1.13	1.137	1.178	Sun <i>et al.</i> (Theo.)
	1.135			Zoroddu <i>et al.</i> (Theo.)
	0.07			Sekimoto <i>et al.</i> (Expt.)

In the valence band region, large peaks of DOS are observed near the band edges. This indicates good mobility of charge carriers in MCoSb compounds and is beneficial for high S values. Since the valence band maxima differs in case of ZrCoSb, change in the nature of charge carriers contributing to transport is expected. It will be discussed in more details in the thermoelectric properties section.

3.3. Thermoelectric properties

In this section, the thermoelectric properties of HH compound MCoSb are presented. We have calculated the Seebeck coefficient (S), the electrical conductivity (σ), thermal conductivity (κ) and the thermoelectric figure of merit (ZT). These parameters are sufficient to characterize the efficiency of a material for thermoelectric energy applications and are calculated from the semi classical transport equation of Boltzmann using rigid band approximation (Chaput *et al.*, 2005). According to this approximation, the band structure of a material remains unchanged with the application of temperature, changing only the chemical potential of the material. This approximation holds good for low doping levels and are found to yield results close to the experimental results (Madsen *et al.*, 2006). The band structure is directly related to the Seebeck coefficient of the material and the Seebeck coefficient to the other thermoelectric parameters. Except the Seebeck coefficient, the electrical conductivity and the electronic thermal conductivity (κ_e) obtained from BoltzTraP are found to be dependent on the relaxation time (τ). Therefore, the dependence of the relaxation time on temperature does not affect the dependence of Seebeck coefficient on temperature. The calculated electrical conductivity and the electronic thermal conductivity from BoltzTraP are expressed in the ratio σ/τ and κ_e/τ .

For better computation purpose, a dense k-mesh of 50,000 k-points were used for successful conversion of the self-consistency criterion. The results obtained from the first principle calculations using WIEN2k code acts as the key input for the calculation of thermoelectric properties. The following Fig. 3.3.1, shows the plot of different thermoelectric parameters as a function of chemical potential (μ) at different temperatures. They are plotted in the chemical potential range of 0.58569 Ry - 0.96469 Ry, 0.475 Ry – 0.825 Ry and 0.525 Ry -0.875 Ry respectively for TiCoSb, ZrCoSb and HfCoSb at different temperatures.

In Fig. 3.3.1 (a), the negative trend in the Seebeck coefficient represents *n*-type carriers, while the positive trend represents *p*-type. For each temperature range from 100 K – 1000 K, distinct positive trend of the Seebeck coefficient indicates the involvement of only *p*-type of charge carriers for the range of chemical potential below Fermi level (E_F). When the chemical potential (μ) becomes equal to E_F , the contribution of both the *p* and *n* type charge carriers becomes maximum. As the μ value increases from E_F , only *n*-type charge carriers contributes to *S*. This is beneficial for a thermoelectric material as it ensures high *S* value. Mixed *n* and *p*-contribution cancels the induced Seebeck voltage thus decreasing the *S* value. The DOS peaks near the band edges and the band gap affects the Seebeck coefficient of the material and thus the thermoelectric properties. The flat valence and conduction band near the fermi level in the band structure prevents the Seebeck coefficient from attaining high values. The band degeneracy and the bands along the *L-Γ* direction in the valence band are responsible for positive values of *S*, while that along the *Γ-X* direction in the conduction band contributes to negative *S* values. The band degeneracy is beneficial for high Seebeck coefficient. The *S* value decreases with respect to chemical potential as the temperature increases. Fig. 3.3.1 (b) and (c) shows the

variation of relaxation time dependent electrical and electronic thermal conductivity with μ . Unlike to S , here both the electrical and thermal conductivity tends towards zero as the values of chemical potential approaches near E_F . κ_e/τ increases with the increase of chemical potential and temperature, whereas σ/τ decreases with the increase of temperature, for those ranges of μ near to E_F . This is because, the charge carrier concentration and the mobility of the charge carriers increases near E_F due to the electronic distribution near the Fermi level. With the increase in temperature, scattering becomes strong leading to high thermal conductivity and hence reducing the electrical conductivity. Therefore, in general, Fig. 3.3.1 reveals that the material MCoSb will be more efficient when doped with n -type impurity and will have maximum efficiency in the chemical potential range above E_F , where the electronic thermal conductivity is minimum.

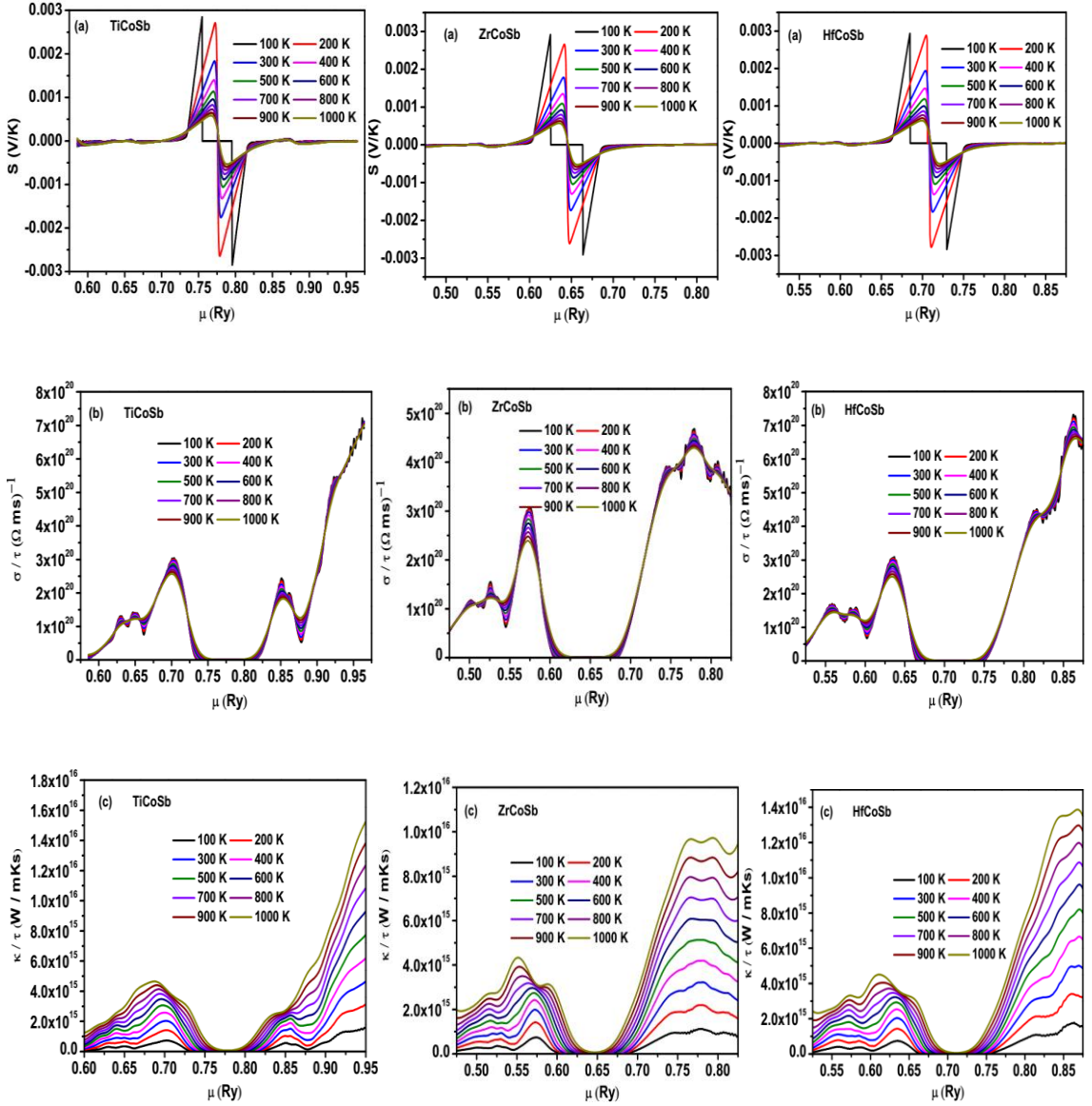


Fig. 3.3.1: Thermoelectric parameters (a) Seebeck effect, (b) Electrical properties and (c) Thermal conductivity as a function of chemical potential.

Among different parameters present in the efficiency expression given by equation 2.50, the one that BoltzTraP is incapable of calculating is the lattice thermal conductivity (κ_l). We have calculated κ_l by solving the Slack's model expressed by equation 2.51. Considering the temperature dependence of the Grüneisen parameter (γ), the Debye temperature (Θ_D) and volume (V), equation 2.51 can be rewritten as-

$$k_p = A \frac{\overline{M} \Theta_D^3(T) \delta(T)^{\frac{1}{3}}}{\gamma^2(T) n^{2/3} T} \quad (3.1)$$

The quantity Θ_D and γ are calculated with the variation of temperature by using equation 2.54 and 2.58 respectively, within the framework of quasiharmonic approximation and is shown in Fig. 3.3.2.

The lattice thermal conductivity of MCoSb compound increases in the order TiCoSb>ZrCoSb>HfCoSb. The calculated values of thermal conductivity are plotted in Fig. 3.3.3 with respect to temperature. Andrea *et al.*, 2014 had calculate κ_p for ZrCoSb by using the many body perturbation theory and the Boltzmann transport equation, in the temperature range of 300K-900K. We have compared our results with that obtained by Andrea *et al.*, and are presented in Fig. 3.3.3 (b). In the temperature range of 300K-700K our calculated values are bit higher than the compared theoretical results. For HH compounds TiCoSb and HfCoSb, no results were found for comparison.

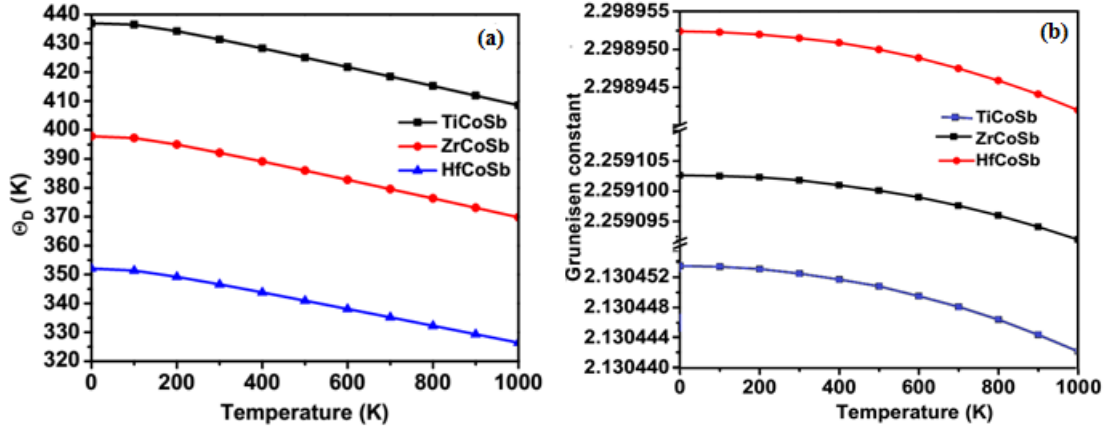


Fig. 3.3.2: Thermodynamic parameters (a) Debye's temperature and (b) Grüneisen parameter used in calculating lattice thermal conductivity, as a function of temperature.

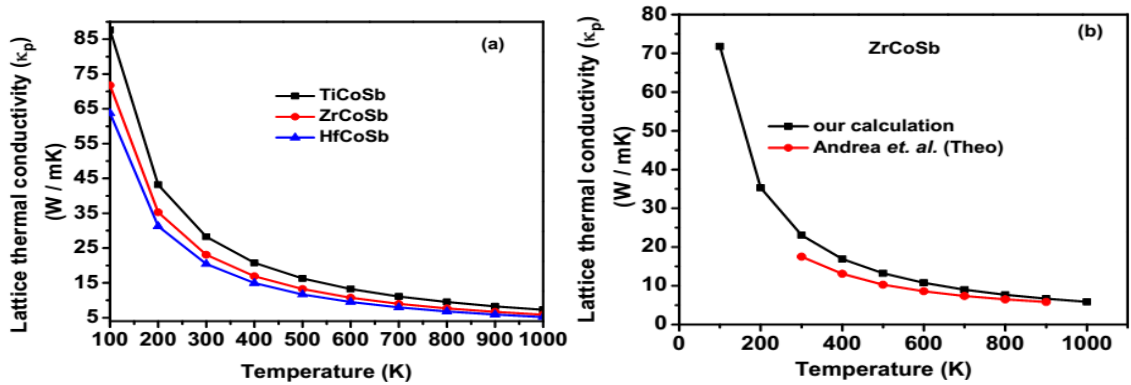


Fig. 3.3.3: (a) Lattice thermal conductivity of MCoSb (M=Ti, Zr and Hf) (b) Comparison of lattice thermal conductivity of ZrCoSb with the theoretical results of

Andrea *et al.*

In order to proceed further to get the ZT results, two methods can be chosen. One can calculate ZT with respect to temperature at constant chemical potential or can calculate ZT with respect to constant carrier concentration. In this present work, we will use the later method, our previous works are reported using the former method (Joshi *et al.*, 2017). The following Fig. 3.3.4 shows the plot of Seebeck constant at different carrier concentration of n - and p -type charge carriers, with temperature. For both n - and p -type doping, the Seebeck coefficient is found to increase with temperature except for the carrier concentration of 10^{19} cm^{-3} , where the carrier concentration decreases from 900K. At higher values of temperature, we expect the Seebeck coefficient value to decrease because of increasing presence of thermally excited charge carriers. The Seebeck coefficient is highest in all MCoSb compound, at a carrier concentration of 10^{19} cm^{-3} for p -type carrier. Thus, p -type charge carriers dominates the charge transport in HH compound MCoSb. This indicates the fact that the maximum thermoelectric ZT value is achievable for p -type case at a carrier concentration of 10^{19} cm^{-3} and will play an important role to achieve high ZT values at high temperatures. Therefore, our further results are reported on this concentration. Yang *et al.*, 2008 have also reported the high power factor of these materials for p -type than the n -type charge carriers. The highest value of the Seebeck coefficient observed are respectively 675 ($\mu\text{V/K}$), 654 ($\mu\text{V/K}$) and 672 ($\mu\text{V/K}$) at 800 K for Ti, Zr and Hf of MCoSb. Since, the band gap values of TiCoSb, ZrCoSb and HfCoSb are close to each other, hence their S values are also close to each other. ZrCoSb has the lowest S value in comparison to the other MCoSb compounds. This is because of the reduced degeneracy leading to reduced effective mass of the carriers which results due to the band gap originating between L - X symmetry directions. S value decreases with the increase in concentration from 10^{19} cm^{-3} and below 10^{19} cm^{-3}

concentration range, mixed *n*- and *p*-type contribution was observed at higher temperatures (not shown in the Fig.). Similar decrease in *S* with the increasing value of concentration was reported by (Lee *et al.*, 2011). The value of *S* is limited by the slopes of the DOS near the Fermi energy which indicates high effective mass of holes in the upper valence band region. The high Seebeck coefficient at 800 K indicates good thermoelectric performance at higher temperatures.

The variation of electrical conductivity (σ), total thermal conductivity (κ) and the thermoelectric Figure of merit (*ZT*) is shown in Fig. 3.3.5. The calculated relaxation time with respect to temperature is shown in figure 3.3.6 and is found to decrease with the increase in temperature. The obtained thermal conductivity results are compared with the available experimental results and it can be seen that our calculated values of κ are in close agreement to the available experimental data. The total thermal conductivity decreases in the higher temperature regions, representing the thermoelectric applicability of these materials in higher temperature domains. The thermal conductivity value calculated at 800 K are presented in table 3.3. The calculated value of electrical conductivity and the Figure of merit *ZT* is higher than the available experimental results, this may be because of the optimized carrier concentration in our results, which showed optimum thermoelectric performance for *p*-type MCoSb, while the experiments report for *n*-type characteristics of the compound. The highest *ZT* values were observed at 800K in TiCoSb (0.29) and ZrCoSb (0.24). HfCoSb had the highest *ZT* at 900K (0.23). As mentioned, our *ZT* values are about ten times higher than those reported by (Sekimoto *et al.* 2005). However, authors have reported *ZT*~0.5, when doped with suitable impurities (Sekimoto, *et al.*, 2007).

The electronic thermal conductivity (κ_e), is very low when compared with the lattice thermal conductivity and is found to decrease with temperature in the range 300 K to 900 K, see Fig. 3.3.5 (b). This indicates phase change from semiconductor to metal in this temperature range, as the thermal conductivity decreases with the increasing temperature only in metals. This change in phase is indeed the key for high electrical conductivity in these compounds. However at temperatures above 2000 K, it is expected that κ_e will be significantly high and will contribute solely to the total thermal conductivity as κ_p will be negligibly small in those temperature ranges. Unfortunately no experimental data are available to compare with the obtained κ_e results and the available theoretical results on κ_e lacks the computation of relaxation time. The ZT values for these materials are much lower than the benchmark value (~ 1), however, owing to the high Seebeck coefficient values and the low thermal conductivity, MCoSb would be a promising thermoelectric material on further optimization of the thermoelectric parameters.

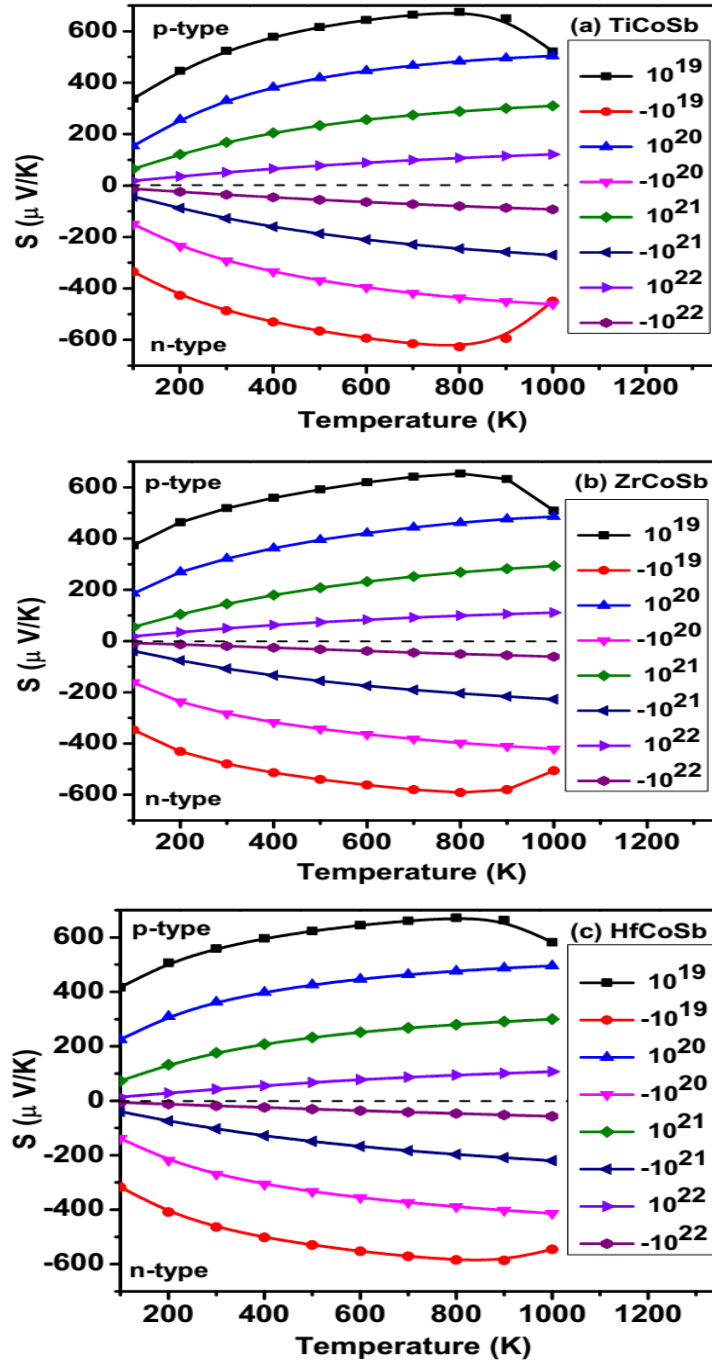


Fig. 3.3.4: Seebeck coefficient of (a) TiCoSb, (b) ZrCoSb and (c) HfCoSb, for different carrier concentration.

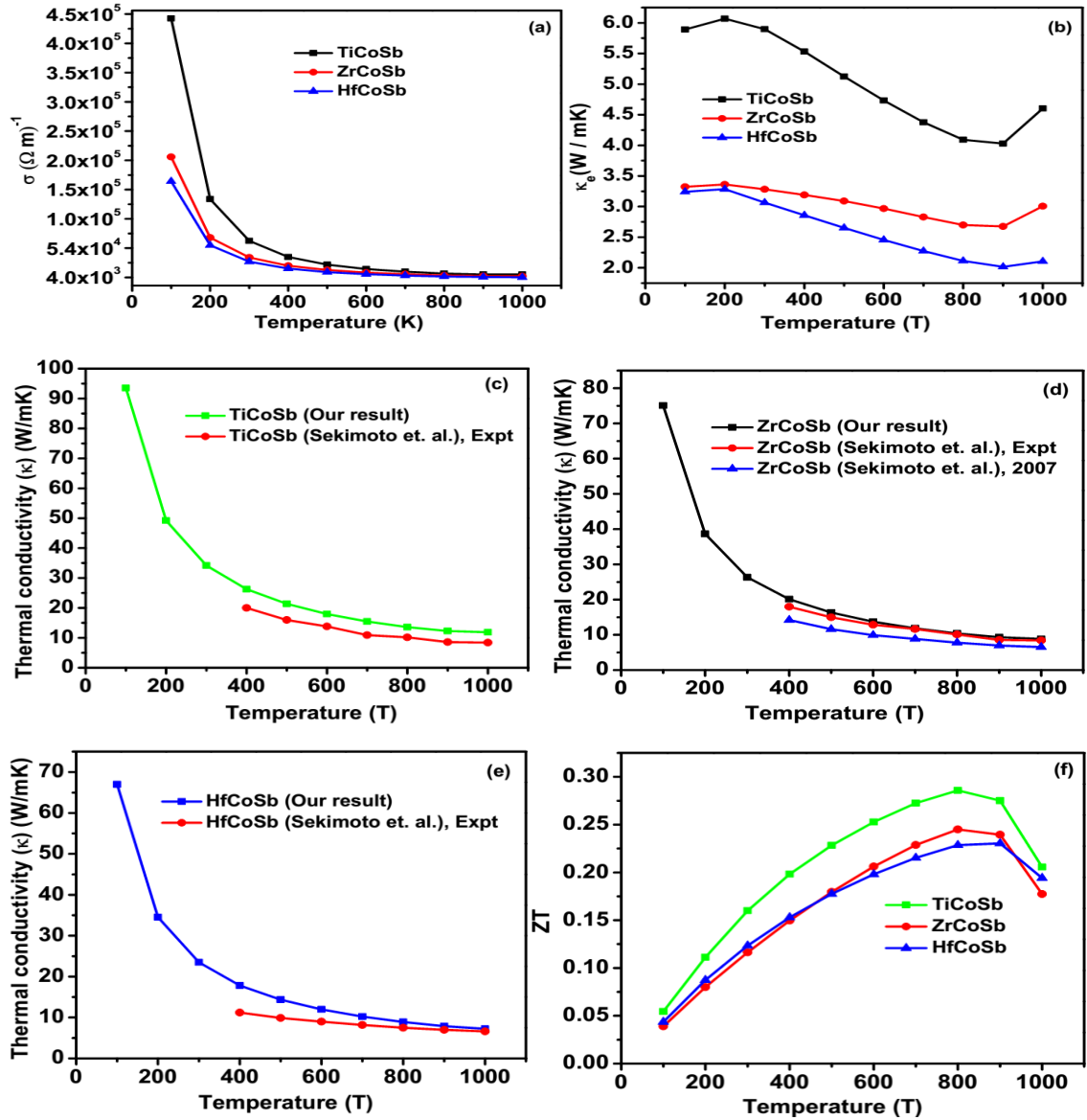


Fig. 3.3.5: (a) Electrical conductivity, (b) Electronic thermal conductivity, (c) Total thermal conductivity of TiCoSb (d) ZrCoSb (e) HfCoSb and (f) the Figure of merit.

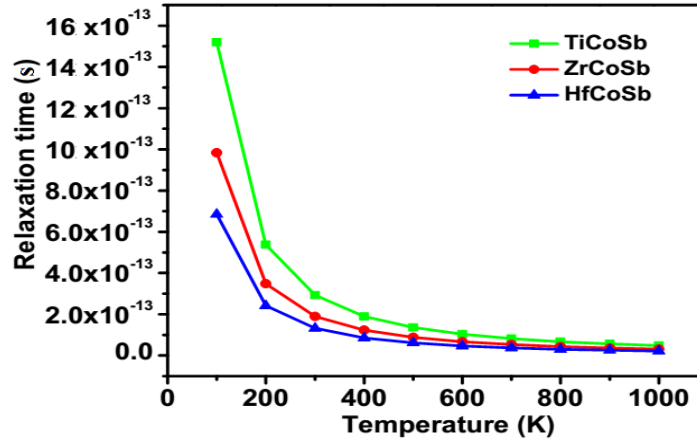


Fig. 3.3.6: Relaxation time calculated as a function of temperature.

Table 3.3: Thermoelectric parameters at 800 K where S was found to be maximum.

Thermoelectric parameters	TiCoSb	ZrCoSb	HfCoSb
Relaxation time (τ) (sec^{-1})	6.71×10^{-14}	4.346×10^{-14}	3.03×10^{-14}
Seebeck coefficient (S) ($\mu\text{V/K}$)	675	672	654
Electrical conductivity (σ) (Ωm^{-1})	10.644×10^3	7.437×10^3	5.627×10^3
Electronic thermal conductivity (κ_e) (W/mK)	4.09	2.698	2.114
Lattice thermal conductivity (κ_p) (W/mK)	9.506	7.689	6.791
Total thermal conductivity (κ) (W/mK)	13.596	10.388	8.905
Figure of merit (ZT)	0.29	0.245	0.23

Chapter 4:

***Investigation of New
Class of Heusler
Thermoelectric Materials***

Investigation of New Class of Heusler Thermoelectric materials

New types of Heusler compounds that has not yet been reported for thermoelectric application is discussed in this chapter. In total, six new types of compounds has been investigated, and are grouped in three categories, according to the nature of the compound, with two compounds each in one group. The groups are namely XAuSn (X=Sc, Lu); CoX'Y'Si (X'=Y, Zr; Y'=Fe, Mn) and XSiSb (X=Hf, Ti). Their crystal structure, electronic and thermoelectric properties, applying the methodology described in chapter 2 has been discussed in details. The equilibrium lattice constants required to begin the calculations has been calculated according to the Murnaghan's equation of state.

4.1 XAuSn (X=Sc, Lu) Half-Heusler Compounds

The compound ScAuSn and LuAuSn was first reported by Sebastian *et al.* (Sebastian *et al.*, 2006). The authors reported the synthesis of the compounds and studied their crystal structures. These compounds have a valence electron count of 18, which according to Slater-Pauling rule are regular semiconductor and would thus interest thermoelectric applications. In our previous work, we have reported the high thermoelectric efficiency of ScAuSn (Joshi *et al.*, 2017) neglecting its lattice thermal conductivity. Here an extended study including lattice thermal conductivity is presented. The rare earth materials are mostly excluded in the combination of Heusler compounds when one is interested in its thermoelectric efficiency. This may be because Heusler

compounds containing rare earth materials are mostly found to be magnetic and such compounds does not interest thermoelectric applications. Further, majority of such materials have variety of crystal structures other than cubic, like hexagonal (TbAuSn, PrAuSn), orthorhombic (YbAuSn), tetragonal (YAuSn) etc. and would thus restrict higher thermoelectric efficiency due to its crystal anisotropy. The compounds XAuSn (Sc, Lu) has a cubic crystal structure with zero magnetic moment and are thus considered to show potential thermoelectric behavior.

4.1.1 Crystal Structure of XAuSn (X=Sc, Lu)

Like other half-Heusler compounds, XAuSn has a space group $F\bar{4}3m$ (Space group no. 216) and crystalizes with MgAgAs type crystal structure with cubic phase. The atoms Sc, Au and Sn in the compound ScAuSn occupy the Wyckoff's position $4b$ (1/2, 1/2, 1/2), $4d$ (3/4, 3/4, 3/4) and $4a$ (0, 0, 0) respectively, whereas Lu, Au and Sn in the compound LuAuSn occupies the position $4b$ (1/2, 1/2, 1/2), $4c$ (1/4, 1/4, 1/4) and $4a$ (0, 0, 0) respectively. The $4c$ position is vacant in case of ScAuSn and the $4d$ position remains vacant in case of LuAuSn. The crystal structure of the compound along with the volume optimization curve is shown in Fig. 4.1. The experimental lattice constants given by Sebastian *et al.* was initially used to calculate the equilibrium lattice constants. The calculated lattice constants along with the Bulk modulus and its pressure derivatives are tabulated in table 4.1.1. Our calculated theoretical lattice constant values are about 1.3% higher, in an average, when compared to the experimental values of XAuSn. A bit higher lattice constant values is because of the choice of exchange correlation functional (i. e. GGA), which tends to overestimate the experimental lattice constants.

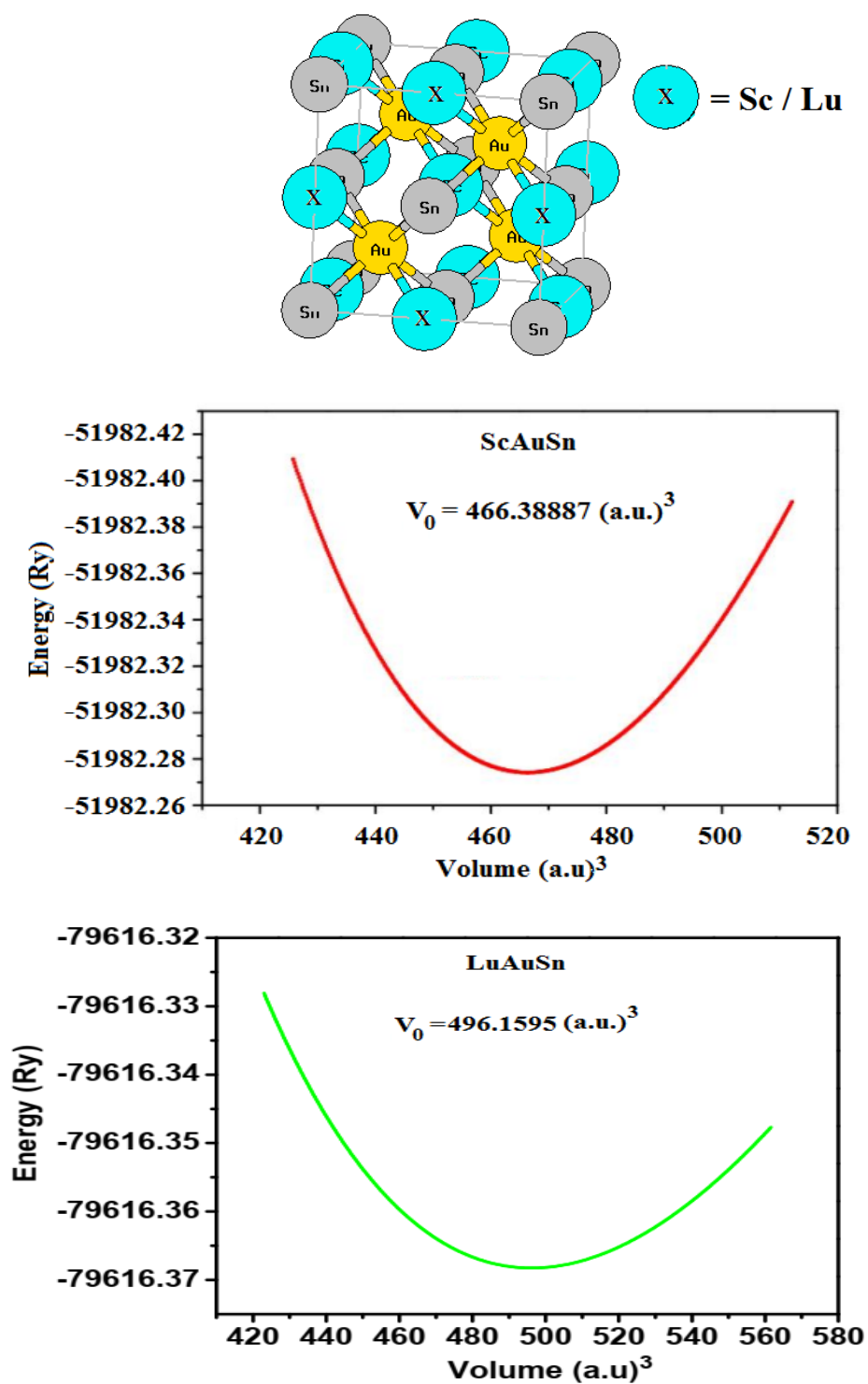


Fig. 4.1: Crystal structure of XAuSn (X=Sc, Au) and their respective volume optimization curves.

Table 4.1.1: Lattice constants (a), Bulk modules (B) and pressure derivative of bulk modules (B') obtained using Murnaghan's equation of state for XAuSn ($X=\text{Sc, Lu}$). The lattice constants values are compared with the experimental results of Sebastian *et al.*, 2006.

Compounds	Lattice constant (a) Å		B (GPa)	B'	Difference in a (Δa)
	Experimental result	Calculated result			
ScAuSn	6.4194	6.5134	92.3875	5.2478	0.094
LuAuSn	6.5652	6.6501	84.8223	3.6871	0.0849

4.1.2 Electronic properties and band structures of XAuSn (X=Sc, Lu)

The lattice constants obtained after volume optimization were used for the calculation of electronic properties. The DOS and band structures of ScAuSn are reported using GGA exchange correlation functional and it shows semiconducting characteristics. In our previous work, we have reported ScAuSn using mBJ potential (Joshi *et al.*, 2017). In case of LuAuSn, no band gap was observed when treated with GGA. With mBJ, LuAuSn also showed semiconducting characteristics. It is well known that GGA tends to underestimate the band gap of a material (Jones and Gunnarsson, 1989) and our studies on LuAuSn shows that this compound has a very narrow band gap. It may be due to this reason that GGA failed to recognize its energy gap. It is to be noted that mBJ is not used for opening a band gap of a gap less material, instead is used to determine the band gap value close to the experimental results which GGA and LDA usually underestimates. However, in LuAuSn, mBJ opened up a band gap which initially was shown gapless by GGA functional. The following Fig. 4.1.2 shows the total DOS plot of the compounds plotted simultaneously along with their band structures. Sharp DOS peaks are observed at the conduction region, in case of ScAuSn, which are mostly dominated by the Sc atoms. In the valence region, a mixed contribution (less than 1 state/eV) from all of Sc, Au and Sn atoms are observed. Also in the conduction region, Au and Sn atoms have very low contribution to the total DOS (< 1 states/eV) and is almost negligible compared to Sc atom which contributes about 7 states/eV at the energy range of 1.4 eV. In case of LuAuSn, it is seen that sharp DOS peaks are missing both in the conduction and the valence region, near the Fermi level. Lu atom dominates the total DOS in the upper conduction region (above 2 eV) but a low mixed contributions by all of three Lu, Au and Sn atoms are observed in the other energy ranges.

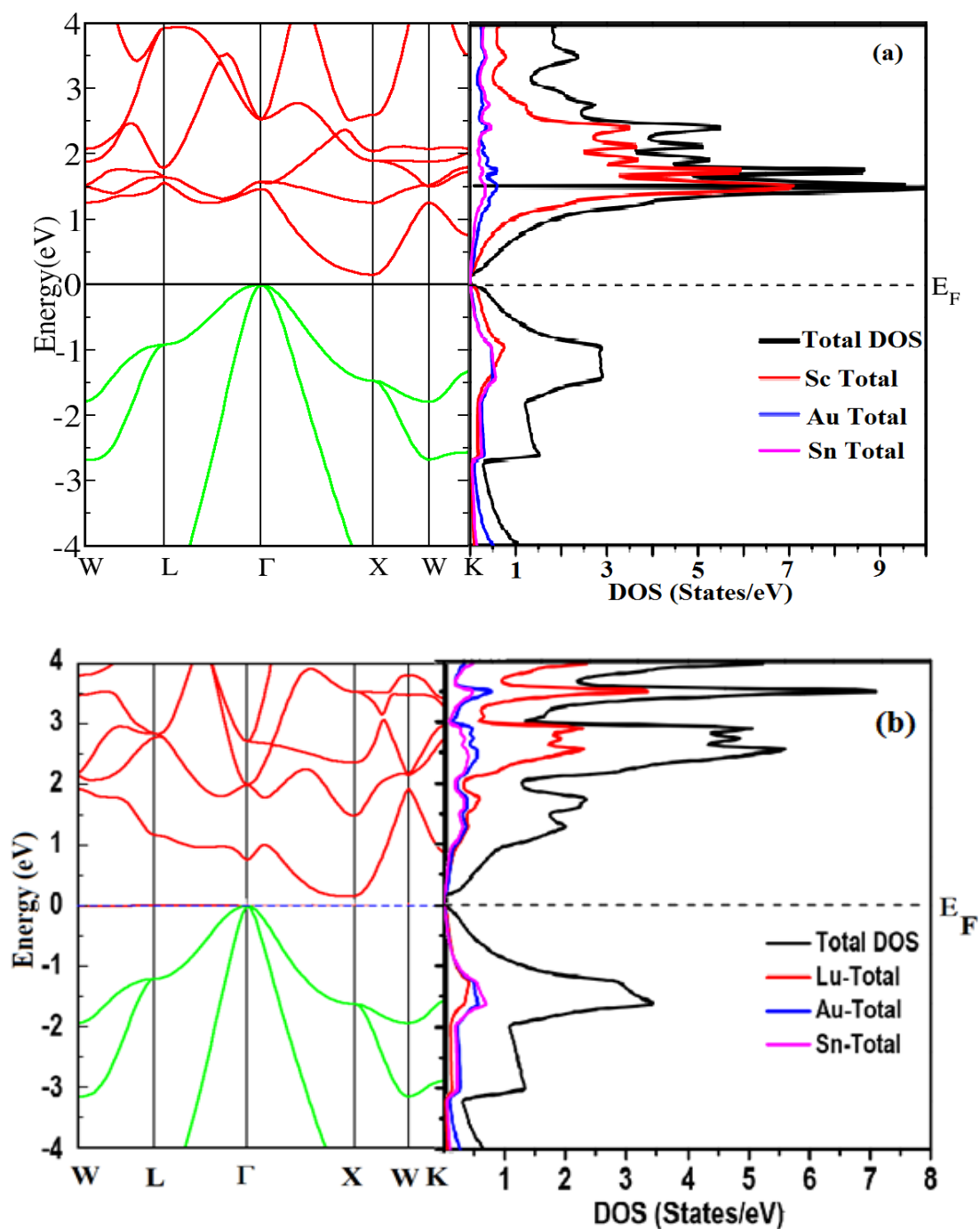


Fig. 4.1.2: Total DOS plotted along with the band structure for

(a) ScAuSn and (b) LuAuSn.

It is clear from the partial DOS plots shown in Fig. 4.1.3 that the maximum contribution to the total DOS comes from the $3d$ -states of Sc atoms in case of ScAuSn. This indicates that d -states of Sc atoms are available for occupation more than other electronic states. The Sc contribution is more pronounced in the conduction region than in the valence region. The highest Sc DOS peak is observed at 1.45 eV and is due to the d -electronic states. Among d -states, the d_{eg} and the dt_{2g} components both have significant contribution in the conduction region. The d_{eg} component comprises of d_{x^2} , d_{y^2} and d_{z^2} states and has maximum DOS contribution of 4.6 states/eV at an energy range of 1.4 eV. Likewise, the dt_{2g} component comprises of d_{xy} , d_{xz} and d_{yz} states and has a maximum contribution of 4.1 states/eV at an energy range of 1.75 eV.

Similarly in case of Au atoms, the $5d$ -states of Au contribute the most in both the valence as well as the conduction region. However, the contribution is not much, with the highest being only about 0.4 states/eV in the conduction region. From 1.75 eV of energy from the Fermi level, the contribution of d -states is solely dominated by the dt_{2g} component of d -states in Au atom. The Sn s -states have almost no contribution in the valence region and are dominated by the $5p$ -states of Sn with the highest contribution coming at -1.4 eV of about 0.5 states/eV. The conduction region has a mixed contribution from both of s and p -states of Sn with the highest s -peak at 2.36 eV and p -at 2.7 eV. Therefore, it can be concluded that the conduction region in ScAuSn is strongly dominated by the $3d$ -states of Sc atom, whereas the valence region has a low occupancy of DOS, with $3d$ -states of Sc, $5d$ -states of Au and $5p$ -states of Sn atom being available for occupation. The sharp DOS features near the Fermi level of ScAuSn favor thermoelectricity.

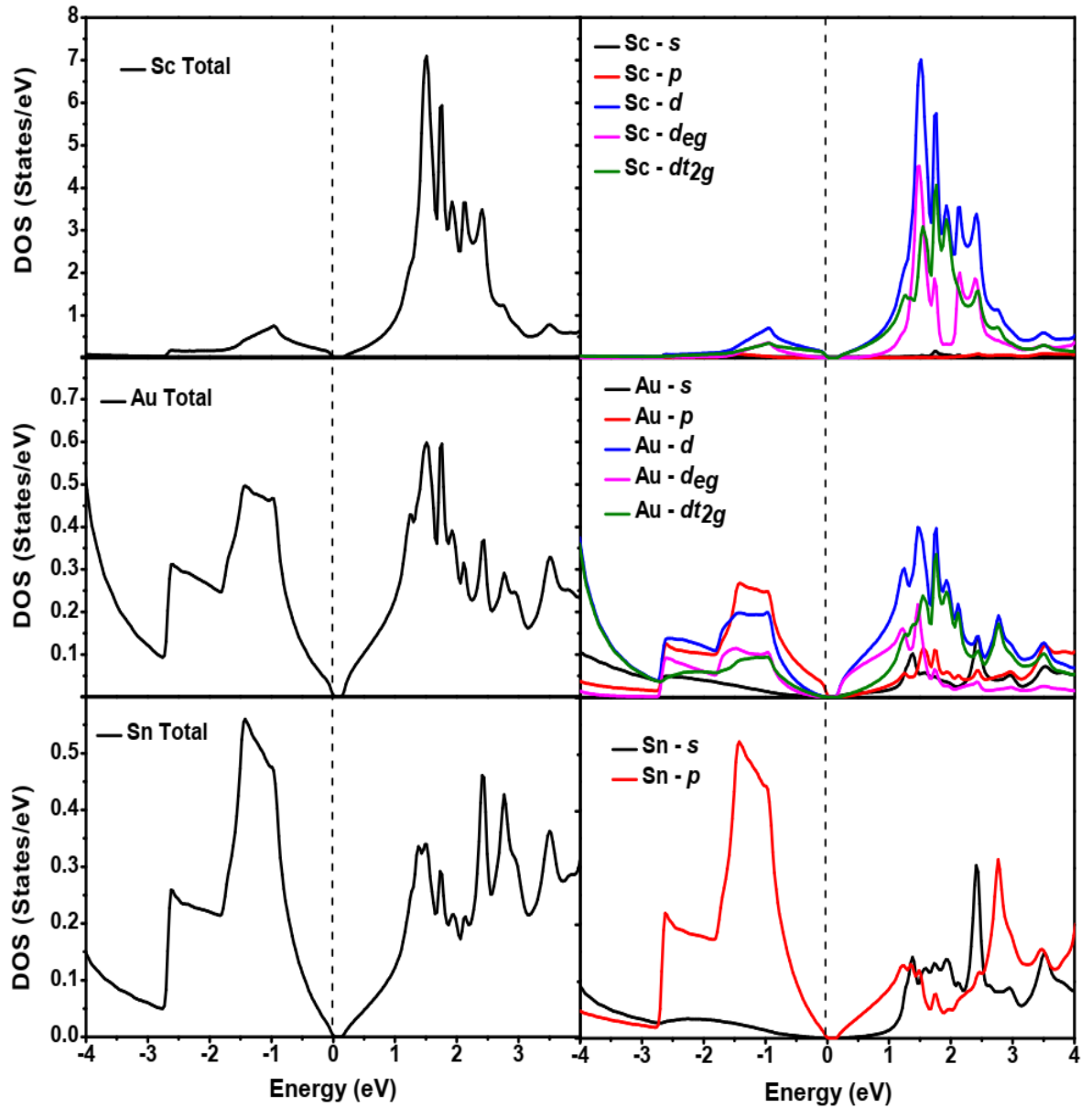


Fig. 4.1.3: Partial DOS plot of ScAuSn, plotted to show the contributions from different electronic states to the total DOS.

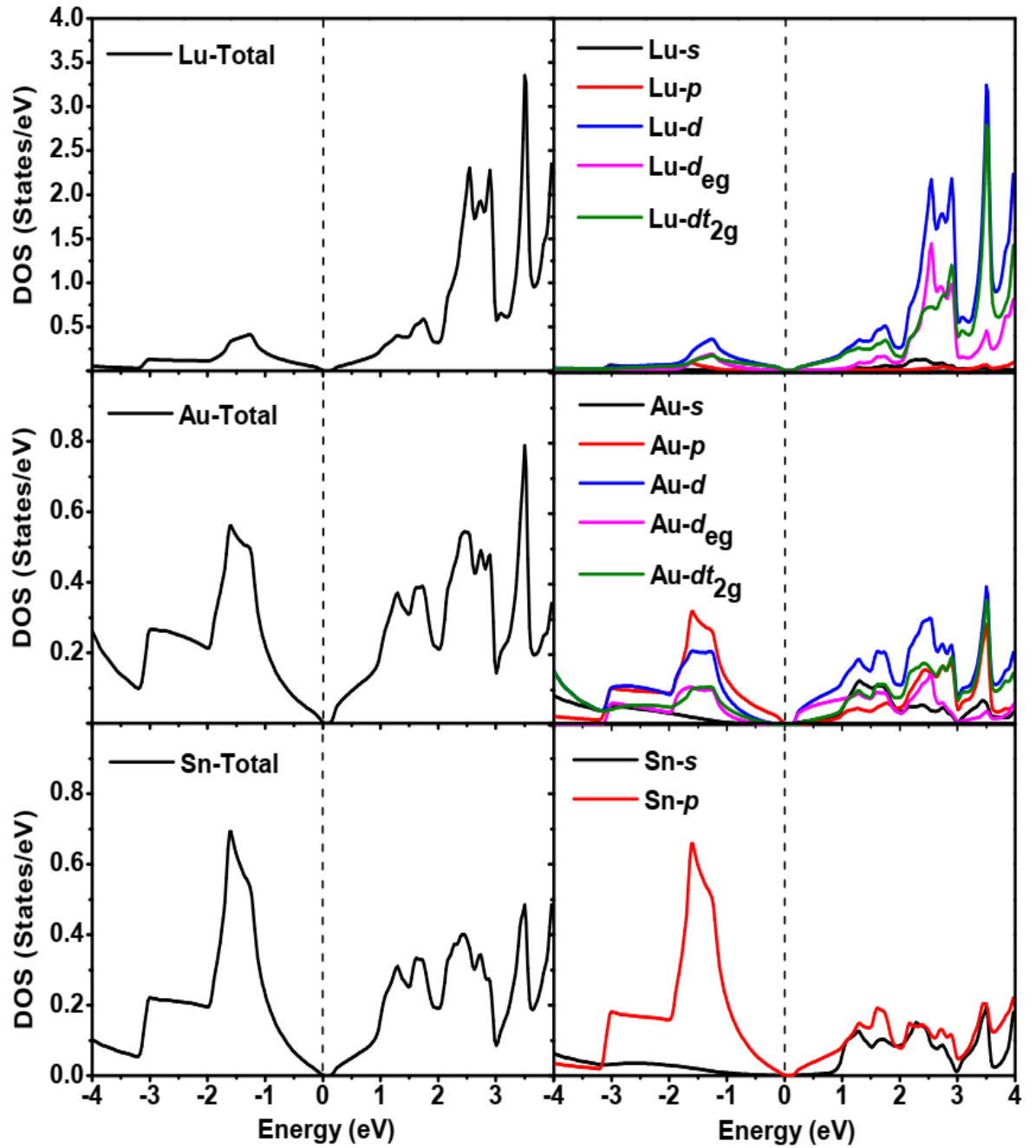


Fig. 4.1.4: Partial DOS plot of LuAuSn, plotted to show the contributions from different electronic states to the total DOS.

Unlike ScAuSn, sharp DOS peaks near the Fermi level is absent in case of LuAuSn. Sharp DOS peaks are observed only in the lower conduction region above 2 eV and in the valence region at -1.8 eV. The Lu $5d$ -states dominates the total DOS plot of the compound. The DOS characteristics in the valence region is similar to ScAuSn, low and mixed. At about 2.5 eV in the conduction region, the d_{eg} component of the Lu d -state shows sharp peaks. Above this the conduction region is solely dominated by the dt_{2g} component. The Au and Sn atom of LuAuSn shows almost similar DOS characteristics like in case of ScAuSn (see Fig. 4.1.4).

The band structure is plotted along the symmetry direction $W-L-\Gamma-X-W-K$ in the irreducible part of Brillouin zone and is shown in Fig. 4.1.5. A narrow indirect band gap along $\Gamma-X$ direction is observed for both the materials with energy gap values of 0.156 eV and 0.164 eV respectively for ScAuSn and LuAuSn. Previously, we had reported a band gap of about 0.344 eV when ScAuSn was studied in the framework of mBJ potential (Joshi *et al.*, 2017). The green and red curves of band structure respectively represents valence and the conduction band curves. For both the compounds the valence band maximum is observed at a symmetry Γ and the conduction band minima on the symmetry point X . Thus, indirect band gaps along $\Gamma-X$ direction is observed in both the compounds. Yang *et al.* had reported a band gap of 0.145 eV for ScAuSn. A closer look in the band structure of LuAuSn also shows a presence of a direct band gap along the symmetry point Γ . The direct band gap measured with respect to GGA functional is about 0.566 eV and that with mBJ potential is about 0.818 eV. Similar direct and indirect band gap characteristics of LuAuSn has recently been reported by Shi and coworkers (Shi *et al.*, 2018). The direct band gap value reported was about 0.666 eV. The zero band gap observed in case of GGA indicates the topological insulator behavior of LuAuSn (Sawai

et. al., 2010 and Shi *et. al.*, 2018). The presence of gap in ScAuSn is attributed due to the large bonding-antibonding splitting (Sawai *et. al.*, 2010) which in case of LuAuSn is small and fails to open up a gap when treated with GGA functional.

The valence band characteristics of both the compounds are closely similar and is due to the almost similar DOS characteristics of the two compounds. Degenerate bands are observed at L and X symmetry points in the valence band region and are found to be missing in the Γ symmetry points near the valence band maximum. These non-degenerate bands limits the thermoelectric efficiency of the compound. The bands originating in the conduction band region is mainly due to the d states of Sc and Lu atoms in each of ScAuSn and LuAuSn. The absence of dense bands near the band edges is due to the low peaks of DOS near the Fermi level. The low peaks of DOS near the Fermi level also restricts the compounds from attaining high Seebeck coefficient value. The band gap originates due to the hybridization of dt_{2g} orbitals of X (Sc/Lu) atom and p orbitals of Sn atom with d_{eg} orbitals of Au atoms. The low density of states near the Fermi level affects the mobility of the charge carriers which will result in low electrical conductivity.

Unfortunately no previous literature on the indirect band gap of LuAuSn is available to the best of our knowledge. Most works on LuAuSn reports the topological insulator property and thus mentions mostly about direct band gap. The narrow band gap of the materials make these compounds narrow band gap semiconductors which is highly favorable for thermoelectric applications.

4.1.3. Thermoelectric properties of XAuSn (X=Sc, Lu)

The parameters such as the Seebeck coefficient (S), the electrical conductivity (σ), thermal conductivity (κ) and the thermoelectric Figure of merit (ZT), which are sufficient to characterize the thermoelectric efficiency of a material are investigated. Except the

Seebeck coefficient, the electrical conductivity and the electronic thermal conductivity (κ_e) obtained from BoltzTraP are found to be dependent on the relaxation time (τ) and hence the relaxation time is also calculated as a function of temperature. The band structure results obtained from WIEN2k under the framework of DFT acts as the input to calculate the thermoelectric properties using BoltzTraP. In an attempt to find the maximum efficiency of the two materials ScAuSn and LuAuSn, the charge carrier concentration near the Fermi level is optimized such as to give the maximum Figure of merit ZT . Due to the inter-dependence of the different thermoelectric parameters, it becomes challenging to obtain high ZT values. Varying the carrier concentration at the Fermi level is one of the method to obtain high ZT but this method also has some limitations. Increasing the carrier concentration ensures high Seebeck coefficient and also decreases the lattice thermal conductivity but reduces the electrical conductivity as well. The Seebeck coefficient being squared in the ZT formula makes it necessary to opt for high S values which otherwise would make S^2 very low. The Seebeck coefficient plotted for different concentration of the charge carriers is shown in Fig. 4.1.5. It is plotted for three different levels of the concentration $\pm 10^{20}$, $\pm 10^{21}$ and $\pm 10^{22}$ cm^{-3} . When the concentration level was increased above $\pm 10^{22}$ cm^{-3} , the charge flow ceased due to the over population of the Fermi level and below the concentration of $\pm 10^{20}$ cm^{-3} mixed flow of charge carriers was observed, which drastically decreased the S value.

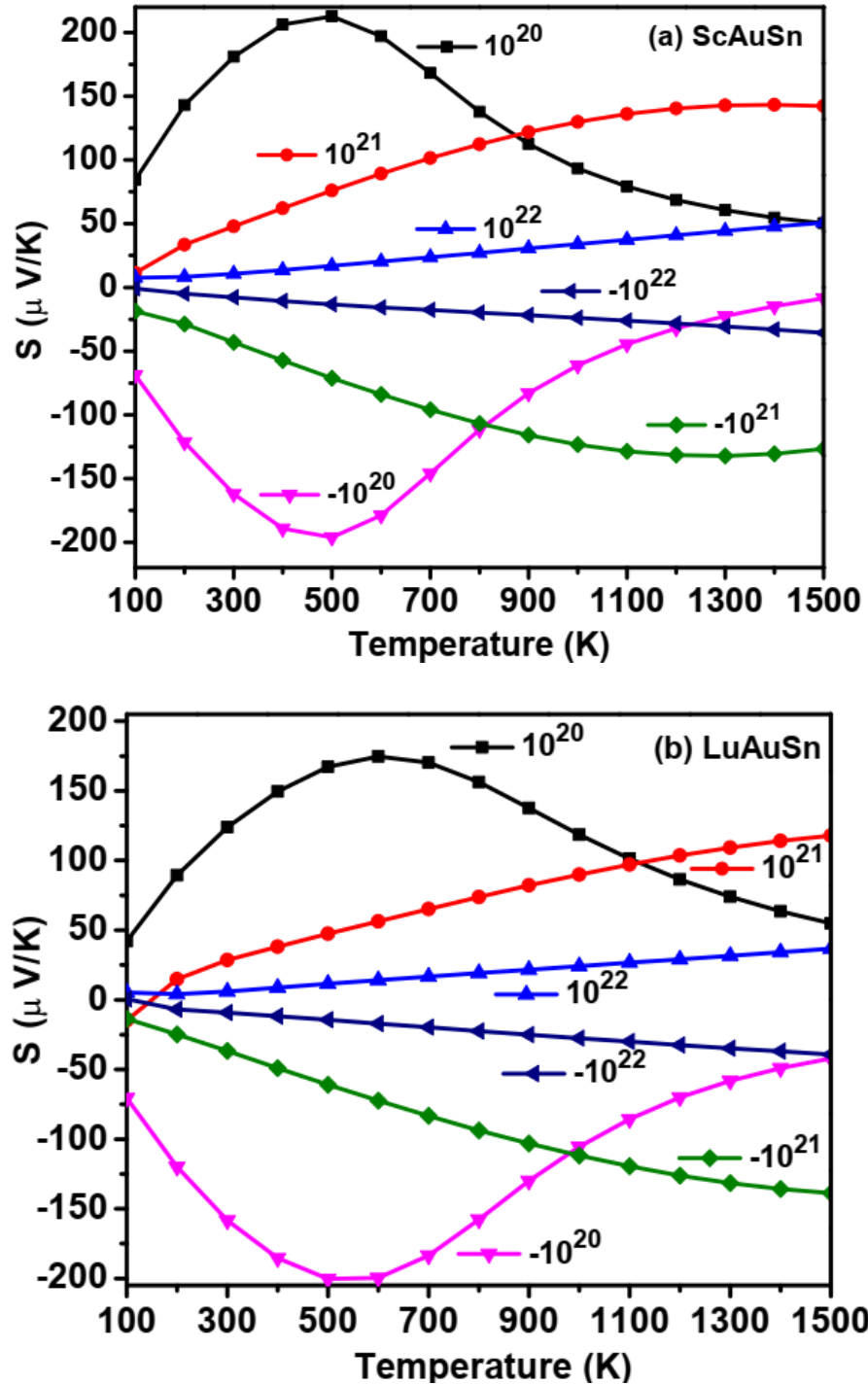


Fig. 4.1.5: Seebeck coefficient of (a) ScAuSn and (b) LuAuSn plotted for different levels of charge carrier concentration.

High S values are observed at $\pm 10^{20} \text{ cm}^{-3}$ at a temperature range of 400 K- 600 K for both of ScAuSn and LuAuSn. In the higher temperature range, the S values rapidly tends towards zero. For application in high temperature range this level of carrier concentration is not suitable and thus we have based our ZT calculation in a concentration of $\pm 10^{21}$ where the S value is found to increase with the increase in temperature, which ensures high thermoelectric efficiency at higher temperature ranges.

The positive trends in ScAuSn dominates the S -value and thus the material will be more efficient in p -type case, unlike LuAuSn which will be more efficient for n -type case. The thermoelectric properties are reported for a carrier concentration of 10^{21} cm^{-3} for ScAuSn and -10^{21} for LuAuSn, where the S value is found to be highest for higher temperature ranges. The following Fig. 4.1.6 shows the plot of different thermoelectric parameters as a function of temperature. The relaxation time is calculated to be of the order of 10^{-14} s for both of ScAuSn and LuAuSn and it decreases with the increase in temperature. The electrical conductivity is found to be of the order of 10^5 , which is quiet high despite of the low DOS of the materials near the Fermi level. The electrical conductivity decreases with the increase in temperature, which is expected as the resistivity would increase with rise in temperature and thus restricts high conductivity at higher temperatures. It is to be noted that the electronic thermal conductivity for both ScAuSn and LuAuSn decreases with the increase in temperature upto 900K, after this temperature, κ_e increases very slowly with the increase in temperature. Such behavior of electronic thermal conductivity is observed in case of highly efficient Heusler thermoelectric materials like TiCoSb and is highly favorable for thermoelectric applications.

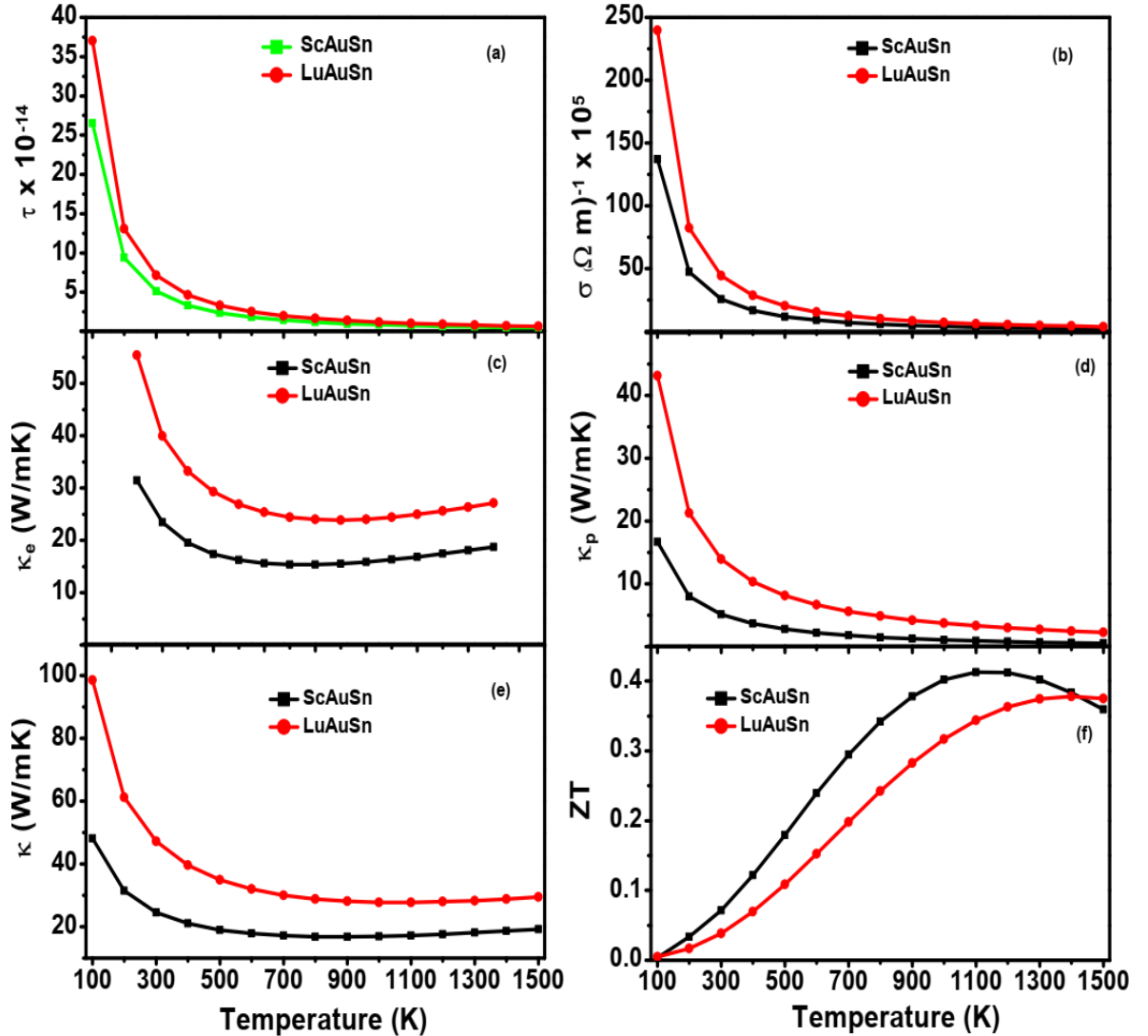


Fig. 4.1.6: Thermoelectric parameters of XAuSn (X= Sc, Lu) plotted as a function of temperature (a) Relaxation time (b) electrical conductivity (c) electronic thermal conductivity (d) lattice thermal conductivity (e) total thermal conductivity and (f) the Figure of merit.

The temperature dependence of Θ_D , the equilibrium volume (δ) and the Grüneisen parameter (γ) required for the calculation of lattice thermal conductivity, as given by equation 3.1 is calculated using quasiharmonic approximations and is shown in Fig. 4.1.7. The total thermal conductivity shows similar characteristics like κ_e . For higher temperatures κ also increases very slowly with the rise in temperature. The increase in κ at higher temperatures is almost negligible in case of LuAuSn and can be considered to have attained a constant value at higher temperatures. Usually the thermal conductivity should increase with the increase in temperature in case of semiconductors but the opposite behavior of the materials can be attributed due to the change in phase from semiconducting to metallic nature of the compounds which as a result decreases the thermal conductivity. In metals, when the temperature increases, the atomic vibrations also increases which as a result decreases the mean free path and thus the relaxation time of the material. Therefore, the flow of electrons is obstructed by the decrease in their mean free path and relaxation time which leads to the decrease in thermal conductivity. The phase change of the compounds ScAuSn and LuAuSn is also supported by the low relaxation time values at higher temperatures and the decrease in electrical conductivity with increasing temperatures.

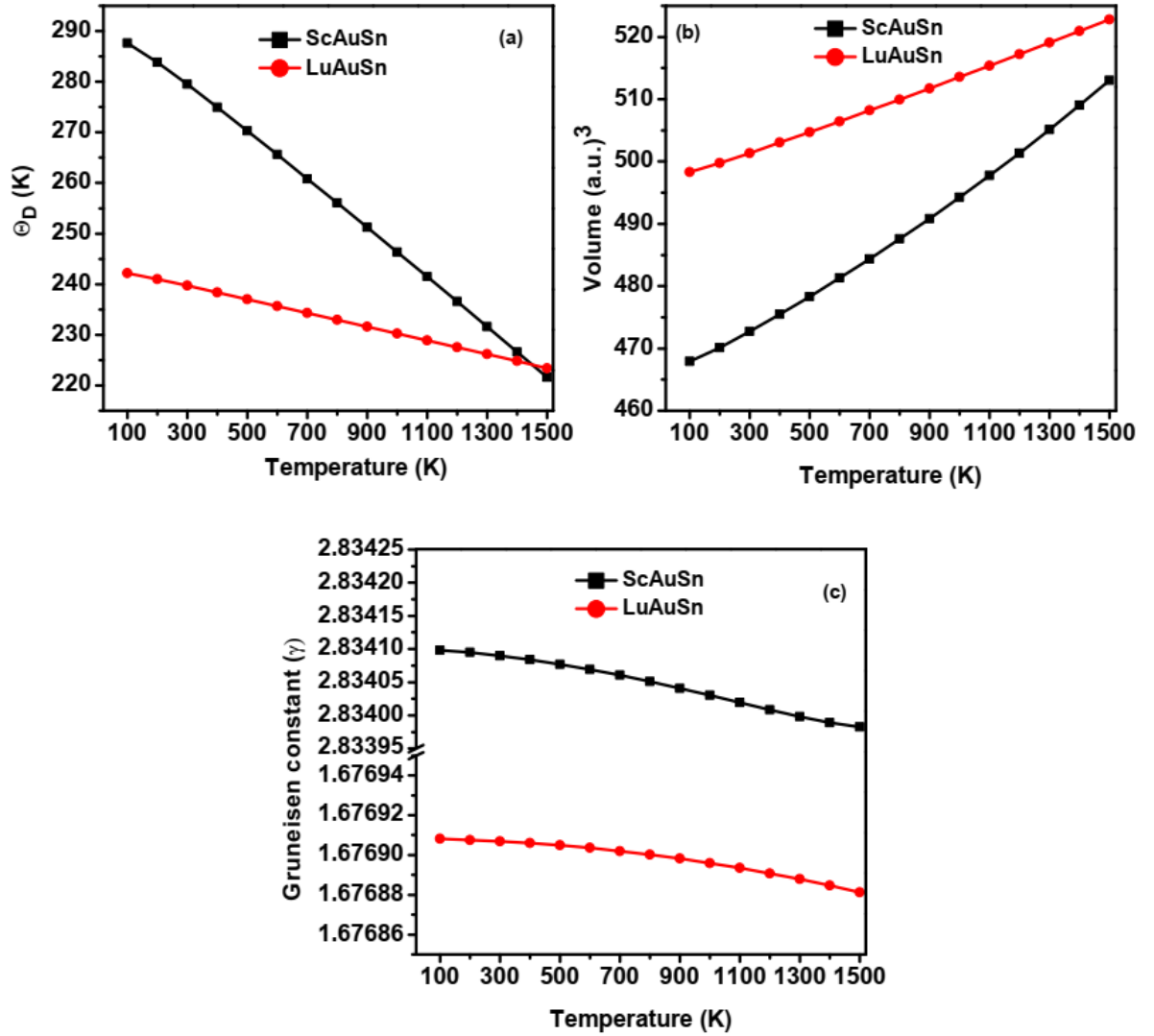


Fig. 4.1.7: Thermodynamic parameters (a) Debye's temperature, (b) Equilibrium volume and (c) Grüneisen parameter used in calculating lattice thermal conductivity, as a function of temperature.

Table 4.1.2: Thermoelectric parameters of ScAuSn and LuAuSn, for those temperatures where ZT is found to be maximum. ScAuSn gives maximum ZT at 1100 K and LuAuSn gives that at 1400 K.

Thermoelectric parameters	ScAuSn	LuAuSn
Relaxation time (τ) (sec^{-1})	7.26×10^{-15}	7.06×10^{-15}
Seebeck coefficient (S) ($\mu \text{ V/K}$)	136.06	-136
Electrical conductivity (σ) (Ωm^{-1})	3.08×10^5	4.21×10^5
Electronic thermal conductivity (κ_e) (W/mK)	16.31	26.32
Lattice thermal conductivity (κ_p) (W/mK)	0.79	2.5
Total thermal conductivity (κ) (W/mK)	17.2	28.8
Figure of merit (ZT)	0.413	0.38

4.2 CoX'Y'Si (X'=Y, Zr; Y'=Fe, Mn) Quaternary Heusler Compounds

Quaternary Heusler (QH) compounds are a new class of Heusler compounds which are recently being considered for thermoelectric and other applications. We have taken two such compounds under investigation namely CoYFeSi and CoZrMnSi, which has a VEC of 24 and thus is predicted to have semiconducting properties favoring thermoelectric applications. Both the compounds were first investigated using GGA energy exchange correlation (XC) functional. With this, CoZrMnSi was identified as narrow band gap semiconductor whereas CoYFeSi appeared to be gapless showing metallic properties. When GGA energy exchange correlation functional was replaced with mBJ potential in case of CoYFeSi, it showed semiconducting band structure with narrow energy gap. The opening of band gap of CoYFeSi, like in case of LuAuSn, indicates that the band gap of this QH compound is very narrow and hence GGA failed to determine it. The gapless behavior of QH CoYFeSi when treated with GGA XC functional further indicates the topological insulator nature of the compound.

CoX'Y'Si (X'=Y, Zr; Y'=Fe, Mn) QH Compounds were reported by Kundu *et al.* and was found to exhibit zero magnetic moment (Kundu *et al.*, 2017). Such property of a Heusler compound interests thermoelectric applications and are thus considered for investigation in the thesis.

4.2.1 Crystal Structure of CoX'Y'Si (X'=Y, Zr; Y'=Fe, Mn)

The structure of QH compound is bit complex in comparison with the FH and HH compounds. Their basic structure is discussed in Chapter 1 section 1.2. The crystal structure of CoX'Y'Si (X'=Y, Zr; Y'=Fe, Mn) consists of Co atoms occupying the Wyckoff position $4c$ (1/4, 1/4, 1/4), Zr/Y atoms the position $4d$ (1/2, 1/2, 1/2), Mn/Fe atoms the position $4b$ (3/4, 3/4, 3/4) and the remaining Si atoms in the position $4a$ (0, 0,

0). Both the compounds crystalizes with space group $F\bar{4}3m$ (Space group no. 216). Their crystal structure and the volume optimization curve based upon the Murnaghan's equation of state is shown in Fig. 4.2.1. The table 4.2.1 shows the comparison of the calculated lattice constants with the available results. Our calculated values of lattice constants are approximately 0.2% higher than the previous theoretical results of Kundu *et al*, 2017. A bit higher values of lattice constants are expected because GGA XC usually overestimates the lattice constants (Zoroddu *et al.*, 2001). Unfortunately, no experimental data are available for comparison of the calculated lattice constants.

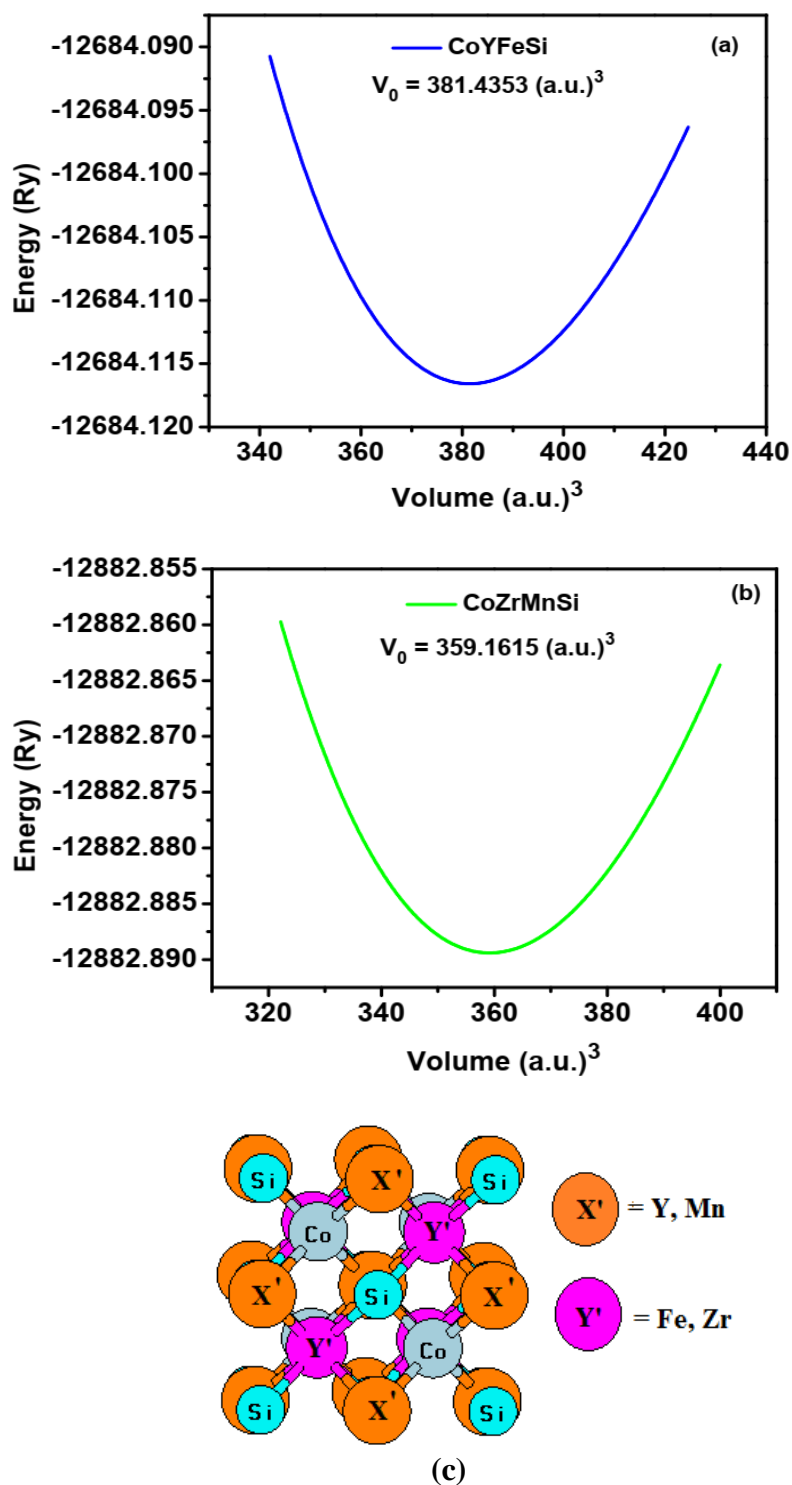


Fig. 4.2.1: Volume optimization curve of (a) CoYFeSi (b) CoZrMnSi and (c) Crystal structure of Quaternary Heusler $\text{CoX}'\text{Y}'\text{Si}$ ($\text{X}'=\text{Y}, \text{Zr}; \text{Y}'=\text{Fe}, \text{Mn}$).

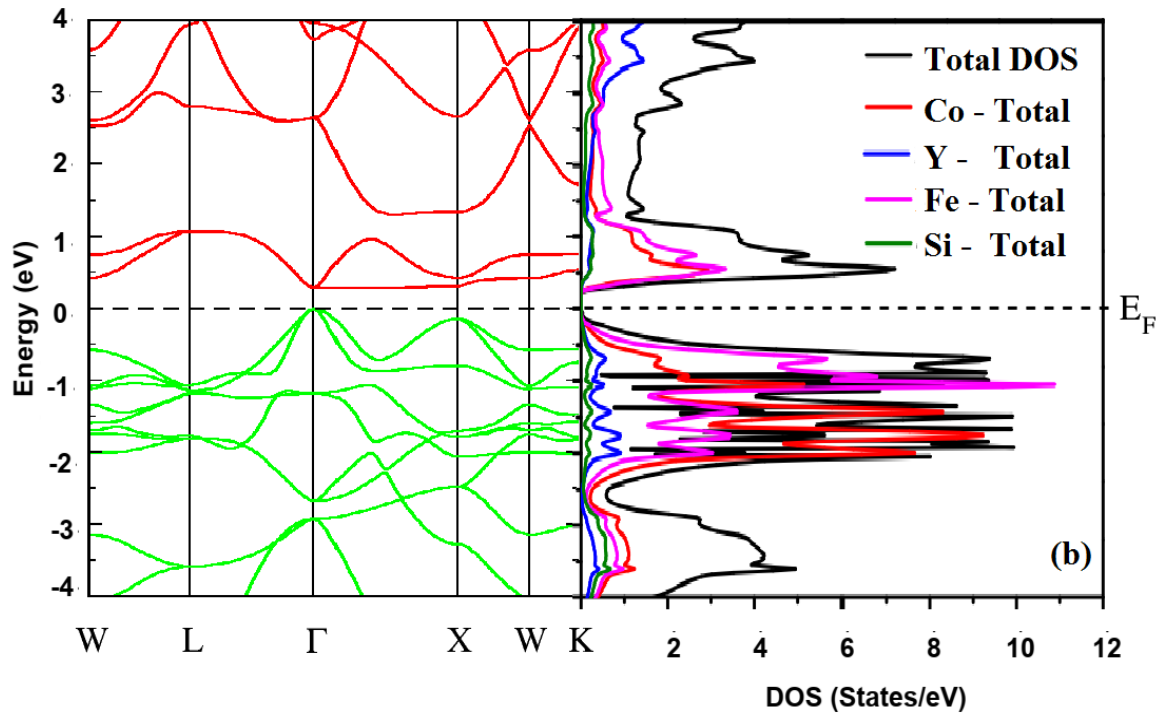
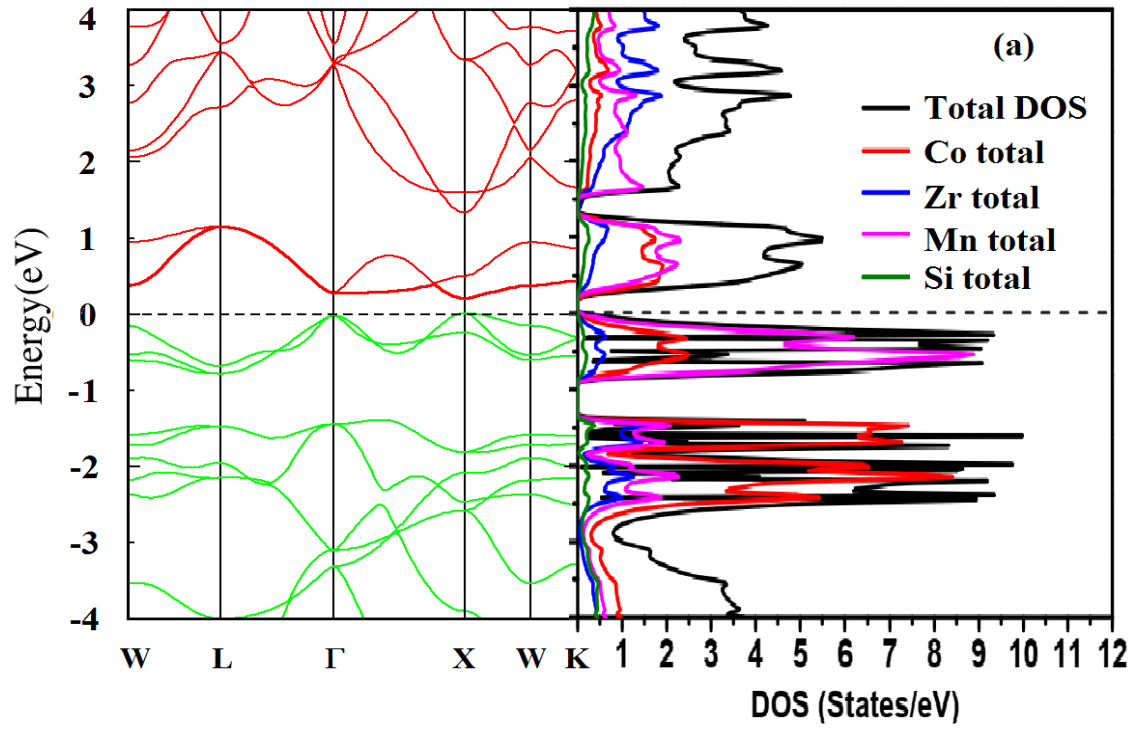
Table 4.2.1: Lattice constants (a), Bulk modules (B) and pressure derivative of bulk modules (B') obtained using Murnaghan's equation of state for $\text{CoX}'\text{Y}'\text{Si}$ ($X'=Y$, Zr; $Y'=\text{Fe}$, Mn). The lattice constants values are compared with the theoretically obtained results of Kundu *et al.*, 2017.

Compounds	Lattice constant (a) Å		B (GPa)	B'	Difference in a (Δa) Å
	Previous result	Calculated result			
CoYFeSi	6.080	6.0920	149.7743	4.8951	0.012
CoZrMnSi	5.96	5.9711	193.0188	3.6542	0.011

4.2.2 Density of States and Electronic Structure of $\text{CoX}'\text{Y}'\text{Si}$ ($\text{X}'=\text{Y}$, Zr; $\text{Y}'=\text{Fe}$, Mn)

The electronic properties of both the QH compounds CoYFeSi and CoZrMnSi were initially investigated using the GGA exchange correlation functional. Since both the compounds have a VEC of 24, so even before starting the calculation it can be predicted that both of them would have a magnetic moment (M) = 0 μ_{B} and would show semiconducting properties, following the Slater-Pauling rule [Slater, (1936) and Pauling, (1938)]. As expected, we found both the compounds to have zero magnetic moment and our results were further verified with the results obtained by Kundu *et al.*, 2017. However, when the calculations were done, the semiconducting prediction was applicable only for CoZrMnSi , whereas CoYFeSi showed no energy gap indicating metallic characteristics. When mBJ potential was applied to CoYFeSi , a narrow band gap opened up and thus our semiconducting prediction also validates for both the compounds. As mentioned earlier, mBJ is not a tool to open up a band gap for a gapless semiconductors but the opening of the band gap in CoYFeSi indicated a presence of very narrow band gap which GGA failed to recognize because of its nature of underestimating the band gap of materials.

In the following Fig. 4.2.2, we have shown the total DOS of $\text{CoX}'\text{Y}'\text{Si}$ ($\text{X}'=\text{Y}$, Zr; $\text{Y}'=\text{Fe}$, Mn) plotted alongside of its band structure for better comparison. We have also shown the band structure of CoYFeSi plotted using GGA XC functional. CoYFeSi is therefore categorized as topological insulator because of its gapless characteristics and would thus slightly differ from CoZrMnSi in terms of its electronic properties. Both the compounds shows high DOS peaks near the fermi level and such compounds are highly preferred for thermoelectric applications.



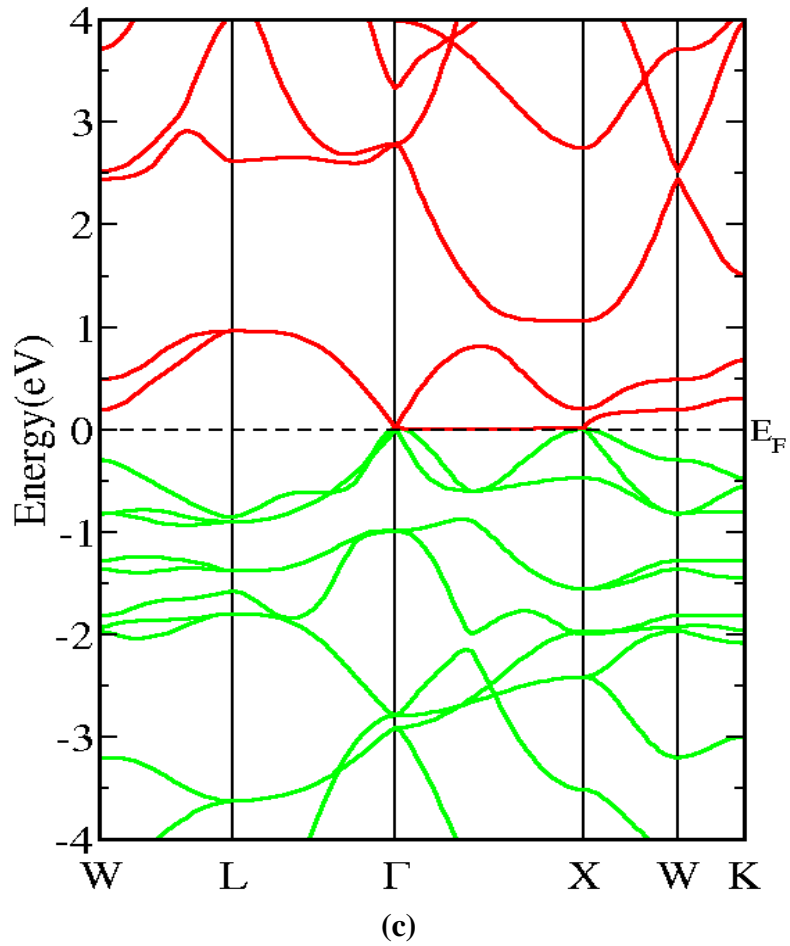


Fig. 4.2.2: DOS plot alongside with the band structure plot for
(a) CoZrMnSi (b) CoYFeSi and (c) the band structure plot of CoYFeSi,
plotted using GGA XC functional.

In reference to the total DOS plots Fig. it can be seen that high DOS peaks are observed in the valence region just below E_F . In the conduction region, just above the Fermi level, sharp DOS peaks as high as 5.5 states/eV and 6.62 states/eV are observed respectively for CoZrMnSi and CoYFeSi. We have divided the valence and the conduction band region in the band structure into the following parts, the upper valence region lies between 0 to -0.85 eV, between -0.91 eV to -4 eV is the lower valence region. From 0 to 1.16 eV is the lower conduction region and the region above 1.32 eV to 4 eV is the upper conduction region in case of CoZrMnSi. It can be seen that multiple energy gaps exist in the band structure of CoZrMnSi and is also evident from its DOS plot. It may be due to this multiple gaps that dense bands are absent both in the conduction as well as in the valence region. In the upper conduction and the lower valence region, the bands are dense compared to those near E_F . The maximum contribution to the total DOS also varied among different energy regions in case of CoZrMnSi. Zr atoms has the maximum contribution to the total DOS in the upper conduction region from 2.4 eV. Upto 2.4 eV, the total DOS contribution is dominated by Mn atoms in the upper conduction region. A small energy gap of about 0.16 eV is observed below the upper conduction region from 1.16 eV to 1.32 eV. In the lower conduction region, Mn and Co atoms contribute the most to the total DOS. In the upper valence region, the Mn atoms completely dominates the total DOS contribution and again an energy gap of approximately 0.6 eV is observed below this region from -0.85 eV to -0.91 eV. In the lower valence region, the Co atoms completely dominates the DOS contribution. The valence and the conduction bands separates out in the Fermi level and thus a band gap of about 0.217 eV is observed, making these compounds semiconductor in nature. Such

multiple energy gaps in DOS of CoZrMnSi is also seen in the plots obtained by Kundu *et al.*, 2017.

Similarly, in case of CoYFeSi, we again have divided the valence and the conduction band region in the band structure into the following parts, the upper valence region lies between 0 to -3.5 eV, between -03.6 eV to -4 eV is the lower valence region. From 0 to 1.25 eV is the lower conduction region and the region above 1.26 eV to 4 eV is the upper conduction region. The DOS contribution in the conduction band region is mostly dominated by Fe atoms except in the upper conduction region between 2.6 eV to 4 eV where Y atoms dominates the contribution. Co atoms also shows significant contribution in the lower valence region. The difference however is not much between the highest contributing to the second highest contributing in the conduction region. Unlike CoZrMnSi, in the upper valence region, very high DOS contributions are seen both from Co and Fe atoms. High peak in DOS of about 10.5 states/eV is observed in case of Fe atoms in this region. All other atoms contributes less than 1 states/eV in the entire valence region. Here also the valence and the conduction bands separate out of each other in the Fermi level and hence a band gap of 0.276 eV is found to exist when treated with mBJ. The GGA band structure showing zero energy gap is shown in figure 4.2.2 (c). The overall DOS plot of both the compounds CoX'Y'Si (X'=Y, Zr; Y'=Fe, Mn) matches with those reported by Kundu *et al.*, with some minor differences in the position and height of the DOS peaks. The differences occur because the authors have included the spin orbit interaction of different electronic states of various atoms that constitute the compound, whereas in our case we have neglected such effects. The various electronic states involved in the DOS contribution and their role in forming the energy bands can be illustrated with the help of PDOS plots which is shown in the Fig. below.

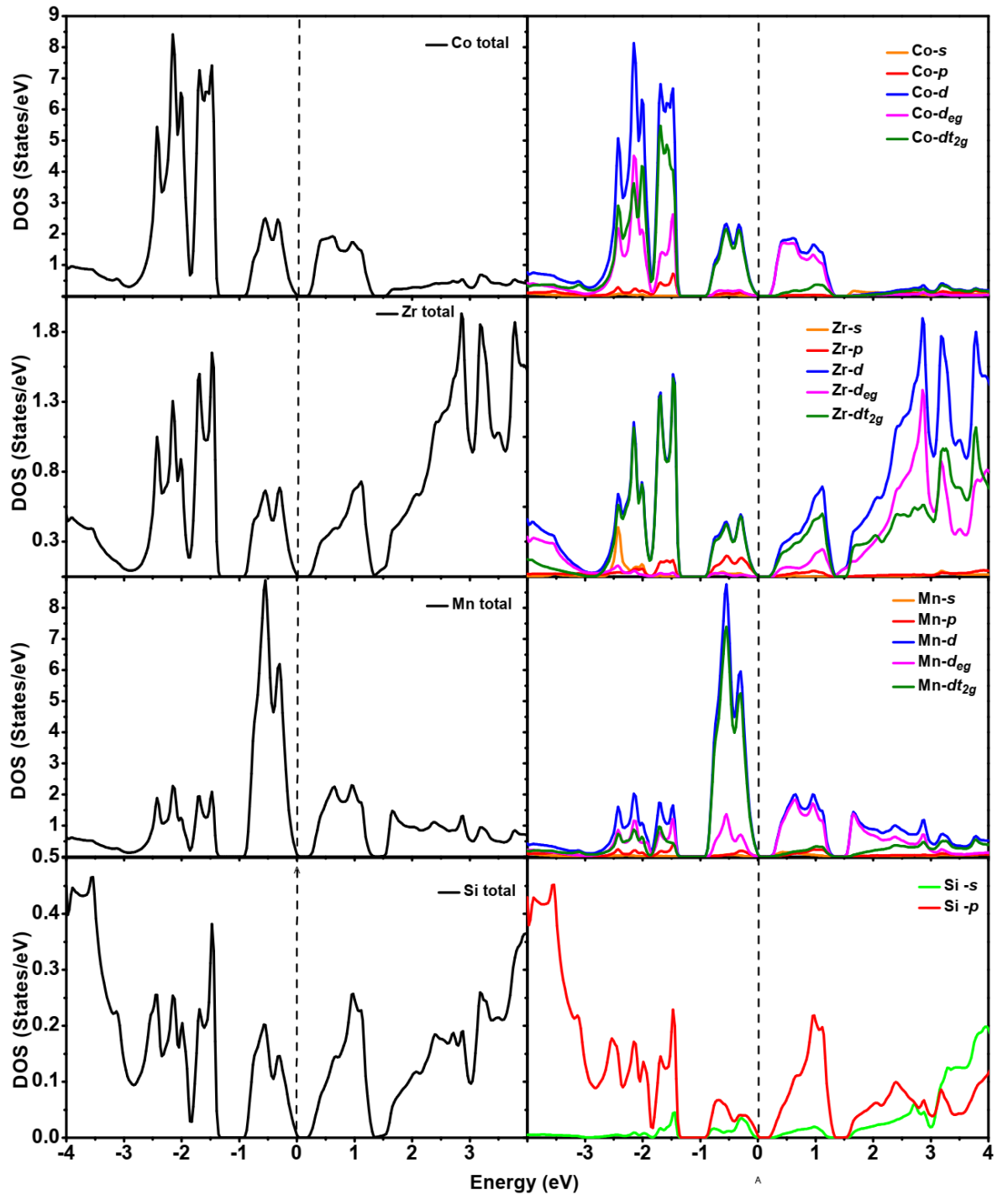


Fig. 4.2.3: Partial DOS plot of CoZrMnSi, representing different electronic states contributing to the total DOS.

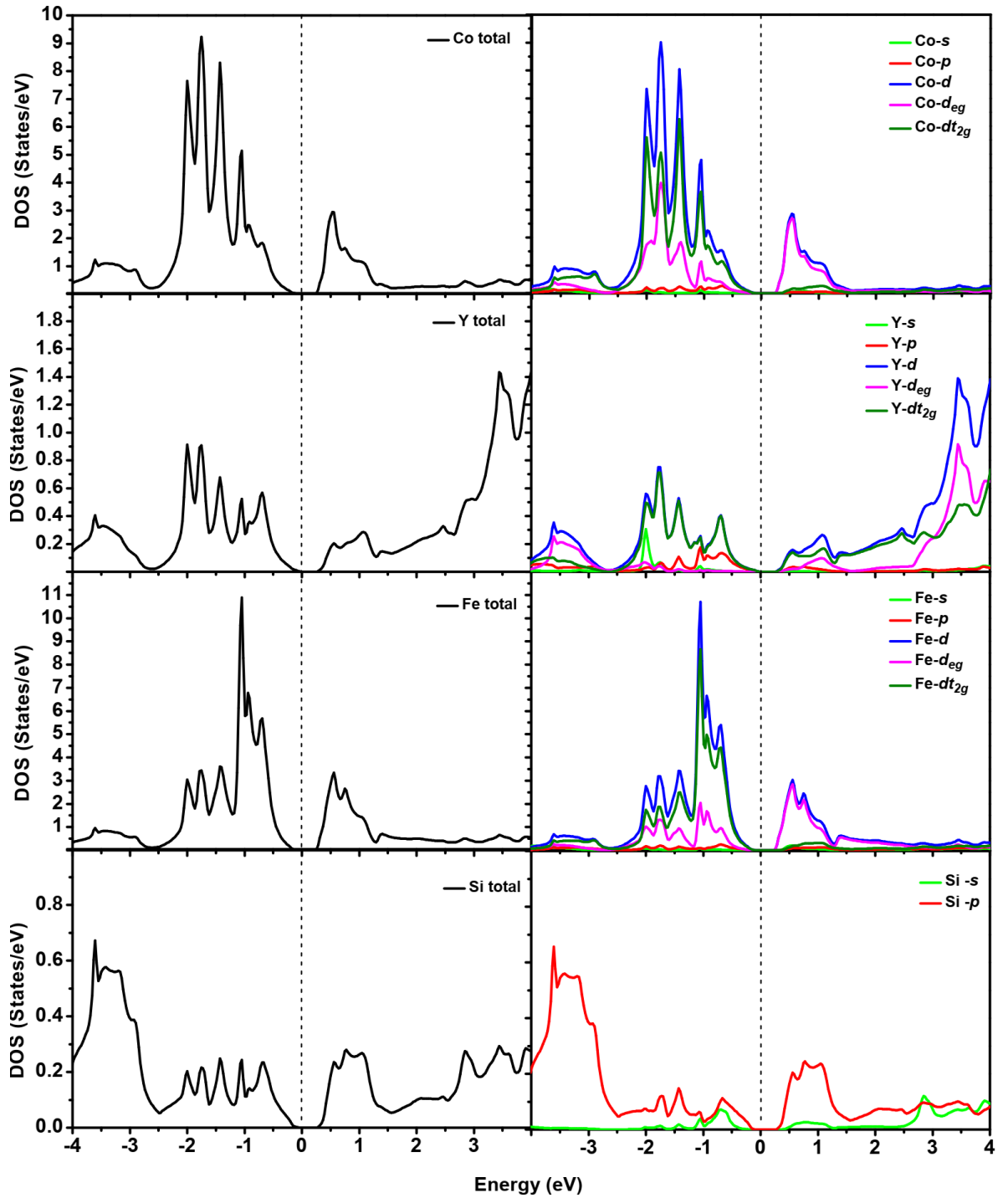


Fig. 4.2.4: Partial DOS plot of CoYFeSi, representing different electronic states contributing to the total DOS.

From the partial DOS plots (Fig. 4.2.3 and 4.2.4), it is seen that the DOS due to Co, Zr/Y and Mn/Fe atoms are mainly due to their d -states, whereas for Si is due to its p -states. In the upper valence region in case of CoZrMnSi, the dt_{2g} sub-states of Co and Mn has the maximum contribution. Therefore the bands in this region is mainly due to the dt_{2g} sub-states of d -states of Co and Mn atoms with some small contributions from dt_{2g} of Zr and p -states of Si atoms. Similarly in case of CoYFeSi, the bands in the upper valence region is from dt_{2g} sub-states of Co and Fe atoms with some small contributions from dt_{2g} sub-states of Y and p -states of Si atoms. Likewise in the lower conduction region, the bands are formed mainly due to Co- d_{eg} and Mn/Fe- d_{eg} with minor contributions from Zr/Y - dt_{2g} and p -states of Si. The formation of band gap in CoX'Y'Si ($X'=Y$, Zr; $Y'=Fe$, Mn) QH compounds can then be explained as due to of dt_{2g} orbitals of Co atom and p -orbitals of Si atom with d_{eg} and dt_{2g} orbitals of X' and Y' atom.

Highly degenerate bands are observed near the Fermi level in both the conduction and the valence band region. Such bands highly favors thermoelectricity. The band structures are plotted along the $W-L-\Gamma-X-W-K$ symmetry directions and an indirect band gap is observed in case of CoZrMnSi along the $\Gamma-X$ direction. In addition to this indirect band gap, a direct gap slightly bigger than the indirect one also exists along the Γ symmetry point of magnitude 0.23 eV. CoYFeSi also shows a direct band gap along Γ symmetry point but it is lesser than the direct band gap observed along the $\Gamma-X$ direction which has a magnitude of about 0.282 eV. The calculated values of band gaps are presented in table 4.2.2. Unfortunately, to the best of our knowledge, there are no theoretical or experimental evidence to validate the precision of the calculation.

Table 4.2.2: Calculated energy band gaps of CoX'Y'Si (X'=Y, Zr; Y'=Fe, Mn)

Compounds	Energy Gap (eV)			
	Direct (GGA)	Indirect (GGA)	Direct (mBJ)	Indirect (mBJ)
CoZrMnSi	0.23	0.217	-	-
CoYFeSi	0	0	0.276	0.282

4.2.3 Transport properties of CoX'Y'Si (X'=Y, Zr; Y'=Fe, Mn)

The electronic structure obtained after *ab initio* DFT calculations shows properties that supports thermoelectric applications. The multiple maxima and minima in the band structure of CoX'Y'Si (X'=Y, Zr; Y'=Fe, Mn) along with degenerate and dense bands near E_F are the key factors for achieving high ZT values. However, the presence of very flat degenerate bands near the band edges will limit the compound from achieving high thermoelectric figure of merit. It is because flat bands results in high effective masses which is unfavorable for high thermoelectric efficiency and also reduced the limit to electronic thermal conductivity which as a result produces high thermal conductivity values. The high effective mass problem can be easily taken care of by doping the material with suitable impurities and therefore we predict that doped CoX'Y'Si (X'=Y, Zr; Y'=Fe, Mn) QH compounds would attain ZT values much closer to unity.

The following Fig. 4.2.5 demonstrates the Seebeck coefficient plotted as a function of temperature at different levels of carrier concentration. The charge carrier concentration considered are $\pm 10^{20} \text{ cm}^{-3}$, $\pm 10^{21} \text{ cm}^{-3}$ and $\pm 10^{22} \text{ cm}^{-3}$. Above $\pm 10^{22} \text{ cm}^{-3}$ the Fermi level becomes too dense and hence would cease the charge flow and below $\pm 10^{20} \text{ cm}^{-3}$, mixed contribution by *n*- and *p*-type charge carriers to S was observed, which would ultimately drastically reduce the electrical conductivity. As seen from the Fig., S value is higher for *n*-case, which indicates that the compound will be more efficient in the *n*-case. But as seen from the band structure, the effective mass is too high in its conduction region even to slightly support thermoelectricity. Therefore, both these compounds are investigated as a *p*-type compound.

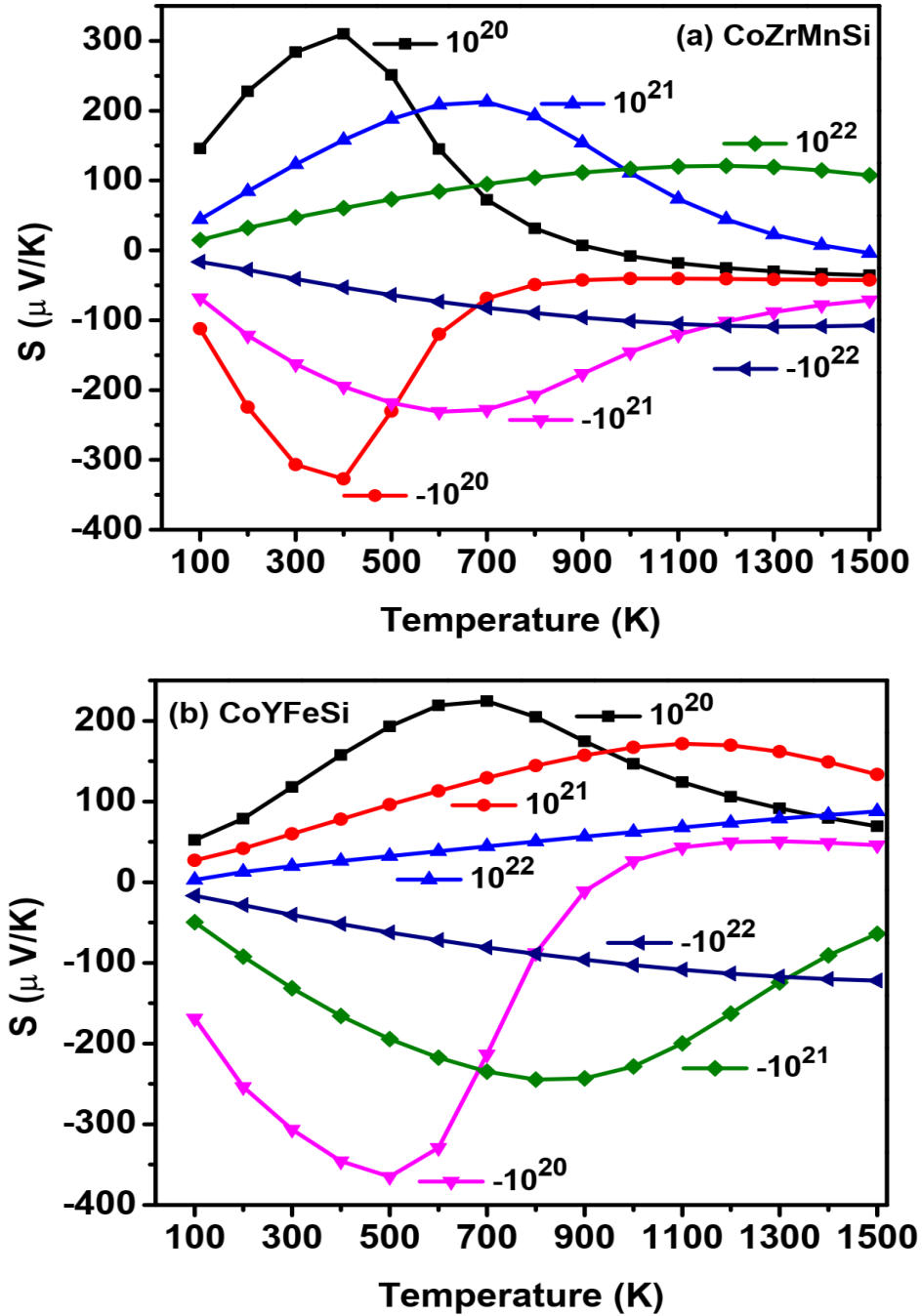


Fig. 4.2.5: Seebeck coefficient as a function of temperature plotted at different levels of carrier concentration

In CoZrMnSi, we have considered the carrier concentration level of 10^{22} cm^{-3} . This is because for higher temperatures other levels of concentration showed mixed contribution to S despite of their higher values. For CoYFeSi, the carrier concentration level of 10^{21} cm^{-3} shows highest unmixed S values and is thus considered for further calculation. The increase in S with the increase in temperature is an indication of the high working temperature range of these compounds. The following Fig. 4.2.6 shows the parameters required to calculate lattice thermal conductivity as a function of temperature.

The calculated lattice thermal conductivity decreases with the increase in temperature and thus these QH compounds prove their potentiality as thermoelectric materials. The different transport parameters calculated as a function of temperature is shown in Fig. 4.2.7. The relaxation time is plotted as a function of temperature and it decreases with the increase in temperature. CoZrMnSi showed very high electrical conductivity but its thermoelectric applications are limited by high thermal conductivity. Very high electrical and lattice thermal conductivity is observed in case of CoZrMnSi and no thermoelectric material has thermal conductivity value close to it. CoYFeSi has moderate thermal conductivity values close to other potential thermoelectric materials. The important factor of thermal conductivity which makes a material potential for its thermoelectric applications is that the total thermal conductivity should decrease with the increase of temperature. Both compounds CoZrMnSi and CoYFeSi fulfill these criterion. Among these two compounds, the highest ZT was observed in case of CoYFeSi and is about 0.32 at 1100 K. CoZrMnSi also showed the highest ZT value in the same temperature range and is about 0.29. These compounds gives their best ZT values in high temperature ranges and can therefore be tuned into excellent thermoelectric materials workable at very high temperature ranges.

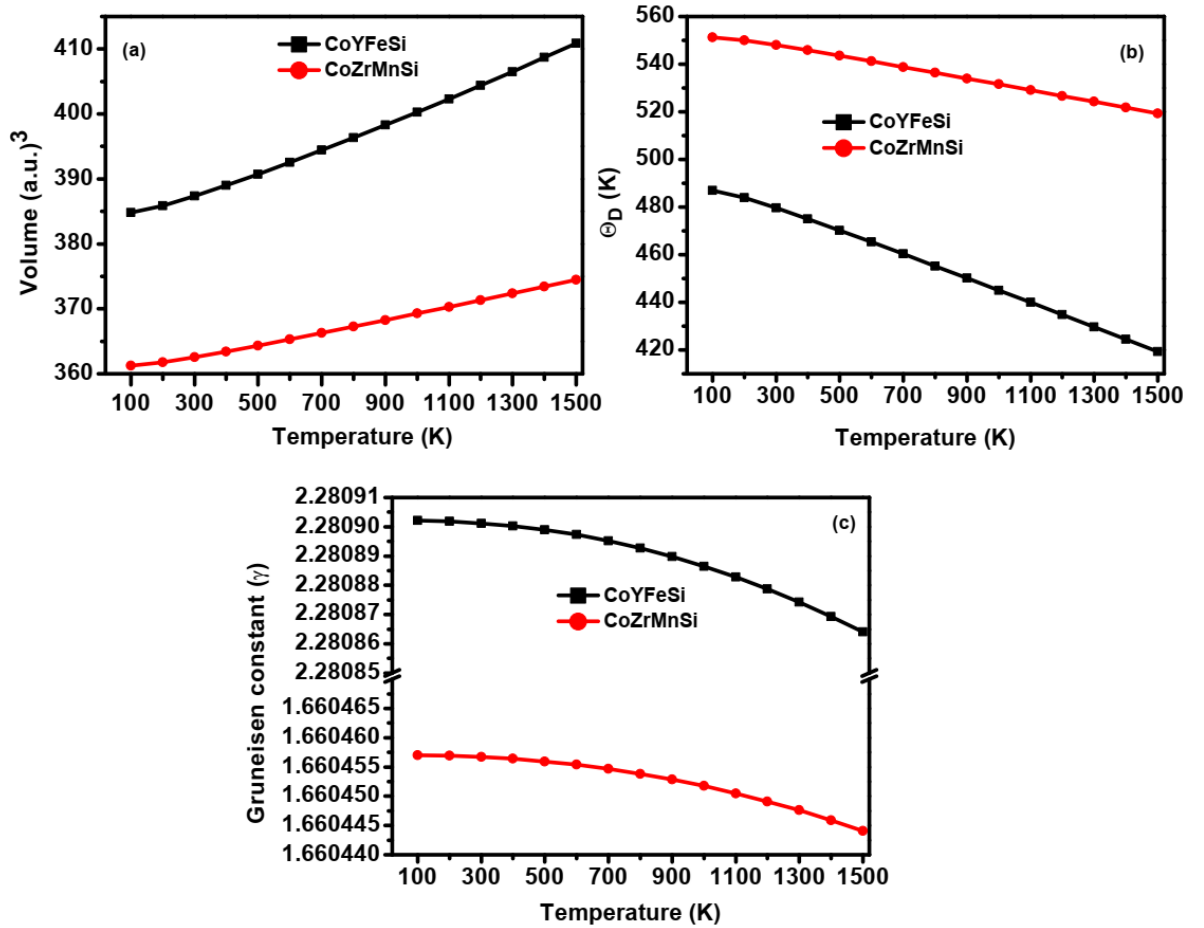


Fig. 4.2.6: Thermodynamic parameters (a) Equilibrium volume, (b) Debye's temperature and (c) Grüneisen parameter used in calculating lattice thermal conductivity, plotted as a function of temperature.

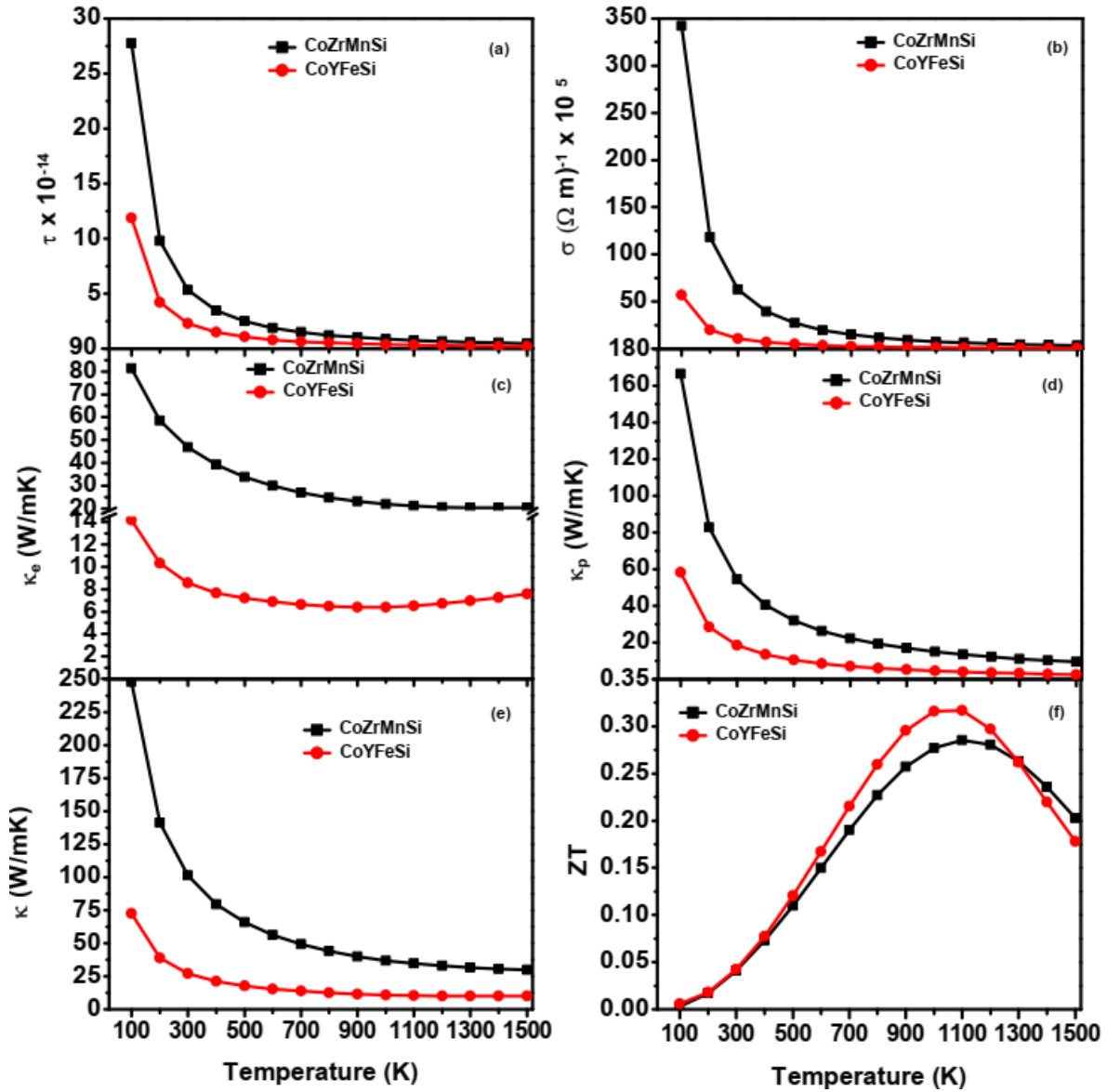


Fig. 4.2.7: Thermoelectric parameters of $\text{CoX}'\text{Y}'\text{Si}$ ($\text{X}'=\text{Y, Zr}$; $\text{Y}'=\text{Fe, Mn}$) QH compounds plotted as a function of temperature (a) Relaxation time (b) electrical conductivity (c) electronic thermal conductivity (d) lattice thermal conductivity (e) total thermal conductivity and (f) the Figure of merit.

Table 4.2.3: Thermoelectric parameters of CoZrMnSi and CoYFeSi, for those temperatures where ZT is found to be maximum. Both CoZrMnSi and CoYFeSi gives maximum ZT at 1100 K.

Thermoelectric parameters	CoZrMnSi	CoYFeSi
Relaxation time (τ) (sec^{-1})	7.6×10^{-15}	3.25×10^{-15}
Seebeck coefficient (S) ($\mu \text{ V/K}$)	136.06	-136
Electrical conductivity (σ) (Ωm)⁻¹	6.214×10^5	1.026×10^5
Electronic thermal conductivity (κ_e) (W/mK)	21.14	6.5
Lattice thermal conductivity (κ_p) (W/mK)	13.5	3.96
Total thermal conductivity (κ) (W/mK)	34.63	10.47
Figure of merit (ZT)	0.29	0.32

4.3 XSiSb (X=Ti, Hf) Half-Heusler Compounds

These compounds are metallic in nature but despite of their metallic nature they are investigated for potential thermoelectric application due to their low thermal conductivity. Usually metals have very high thermal conductivity and is thus neglected in the search of good thermoelectric materials. Subjected to structure modifications, these compounds can show potential thermoelectric behaviour at room temperatures and thus they make it to the list of thermoelectric materials. Structure anisotropy is to be taken care of in order to realise these materials in practise.

4.3.1 Structural Optimization of XSiSb (X=Ti, Hf)

TiSiSb and HfSiSb are hypothetical compound and we have assumed that it has the same structure as Ge based TiGeSb. TiGeSb crystallizes in a ZrSiS-type structure possessing tetragonal-phase with P4/nmm space group. (Joshi *et al.*, 2017) A unit cell of HfSiSb and TiSiSb consists of six atoms occupying three two-fold positions with Hf on 2c (1/4, 1/4, 0.2420), Si on 2a (3/4, 1/4, 0) and Sb on 2c (1/4, 1/4, 0.6112) for HfSiSb and Ti on 2c (1/4, 1/4, 0.2404), Si on 2a (3/4, 1/4, 0) and Sb on 2c (1/4, 1/4, 0.6175) for TiSiSb (Mahan *et. al.*, 1997). Structural optimization based on Murnaghan's equation of state (Murnaghan, 1994) was performed to obtain the relax structure with minimum energy and is shown along with the crystal structure in Fig. 4.3.1. Unfortunately, to the best of our knowledge, there are no experimental results for the comparison of the calculated lattice constant, bulk modulus, etc. Thus we have compared it with that of the available theoretical ones, as shown in table 4.3.1. It is seen from the table that the present structural parameters of HfSiSb and TiSiSb compound are in excellent agreement with the available theoretical values.

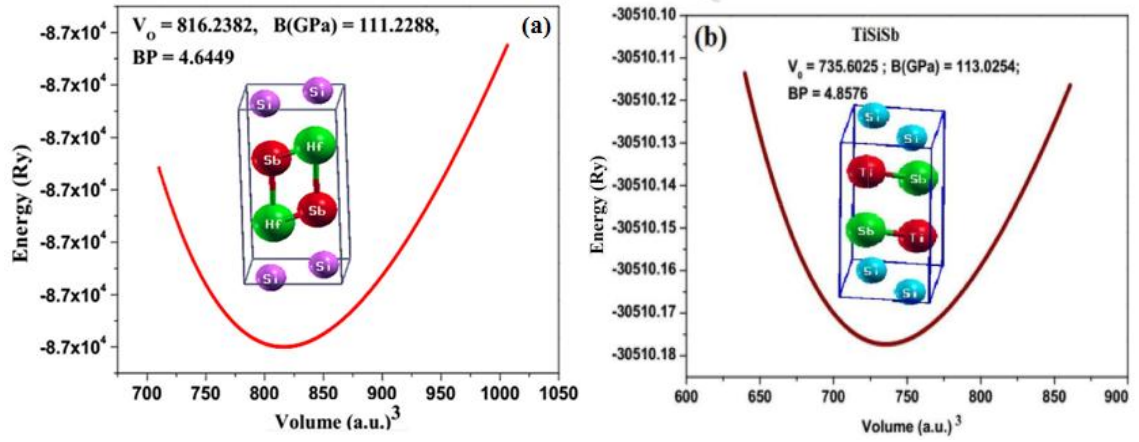


Fig. 4.3.1: Crystal structure along with the volume optimization curve for
(a) HfSiSb and (b) TiSiSb

Table 4.3.1: Comparison of the calculated lattice parameters with the available theoretical results.

Compounds	Lattice constant (a) Å		Lattice constant (c) Å		B(GPa)	B'
	Previous result	Calculated result	Previous result	Calculated result		
HfSiSb	3.740*	3.746	8.603	8.618	111.23	4.645
TiSiSb	3.634*	3.642	8.203	8.22	113.025	4.86

*(Deligoz *et al.*, 2016)

4.3.2 Electronic properties of XSiSb (X=Ti, Hf)

To determine the thermoelectric properties it is necessary to obtain a good description of the electronic structure. The band structure along with the total DOS is plotted in case of HfSiSb and is shown in Fig. 4.3.2 (a). The contributions of different electronic states in the valence and the conduction band determines the electronic property of the material. It can be clearly seen that no band gap is observed, implying that these materials are metallic in nature. In the Fermi level E_F , there is no hybridization between the Hf- d_2 and Si/Sb- d_0 states and, hence, a band gap is missing. This is because of dispersed bands that are a result of the overlap between p-states of Hf with that of Si and Sb (Joshi *et al.*, 2017). The band curves near the Fermi level are quite sharp in almost all directions except in the $X-M$ direction, where the band curves are flat in the valence band region. Sharp curves are beneficial for the Seebeck coefficient and this may be the reason for non-zero value of the Seebeck coefficient (Joshi *et al.*, 2017). From the partial DOS plots shown in Fig. 4.3.3 and 4.3.4, the maximum contribution to the total DOS is due to the Hf- d_2 states (~ 4.2 eV) and there is an appreciable contribution from the p states of Si and Sb. Since Hf has the highest contribution near the Fermi energy, therefore the sharp peaks in the DOS are mainly due to d-state electrons (Joshi *et al.*, 2017). The DOS near the Fermi energy of HfSiSb is about 8 electrons eV^{-1} , which is the main reason for high electrical conductivity. Thus, the electrons at the top of the valence band and those at the bottom of the conduction band mostly come from the d -orbital and some from the p -orbital. The sharp peak at 0–2 eV below the Fermi energy is due to the occupied dt_{2g} (d_{xy} , d_{xz} , d_{yz}) states while the peaks above the Fermi energy at around 2–6 eV are due to the unoccupied d_{eg} (d_{z^2} , $d_{x^2+y^2}$) states (Joshi *et al.*, 2017). In comparison to the DOS results, it can be seen from the band structure results that the bands from 1.4 eV to 8 eV

are due to the d -state electron of the Hf atom. The dense band at the vicinity of the Fermi energy (E_F) is mostly due to the d -states of Hf atoms, whereas the thin bands away from E_F are mainly due to the $Sb-p$ and $Si-p$ states. In the valence band region, from about -7.2 eV to 1.6 eV, the bands are dominated by the d -states of Hf atoms; the p -states of Si and Sb have a very low contribution (Joshi *et al.*, 2017). In the conduction band region, the contribution to DOS by all Hf, Si and Sb atoms is very small and is almost equal. A closer look at PDOS plot shows that the maximum contribution of $Si-p$ states (mainly from the p_z orbital) to the total DOS is at -1.6 eV, whereas $Sb-(p_x + p_y)$ contributed at -1.8 eV, below E_F . Still, the sharp peaks at $(1-2$ eV) below E_F are very small compared to the peaks due to Hf- d states. Thus, the hybridization between Hf- d_2 and Si/Sb- d_0 states are missing, and this may be the reason for deformed and dispersed DOS at E_F (Joshi *et al.*, 2017).

Similarly for TiSiSb, the sharp peak at ~ 2 eV above Fermi energy is due to the occupied dt_{2g} (d_{xy} , d_{xz} , d_{yz}) states while the peaks below Fermi energy at around $0 - 2$ eV is due to the unoccupied d_{eg} (d_{z^2} , $d_{x^2+y^2}$) states. The overlapping of valence and conduction band indicates the metallic nature of TiSiSb (Joshi *et al.*, 2017). In the upper valence region, from -2 eV the bands are mainly due to d -state of Ti atoms. The bands in the conduction region are dominated by the d -state of Ti atoms. In the fermi level E_F , the p -state of Ti overlaps with that of Si and Sb, resulting in dispersed band along the Fermi level. Since there is no hybridization among the states, hence no band gap is observed for TiSiSb (Joshi *et al.*, 2017) (See Fig. 4.3.2 (b)).

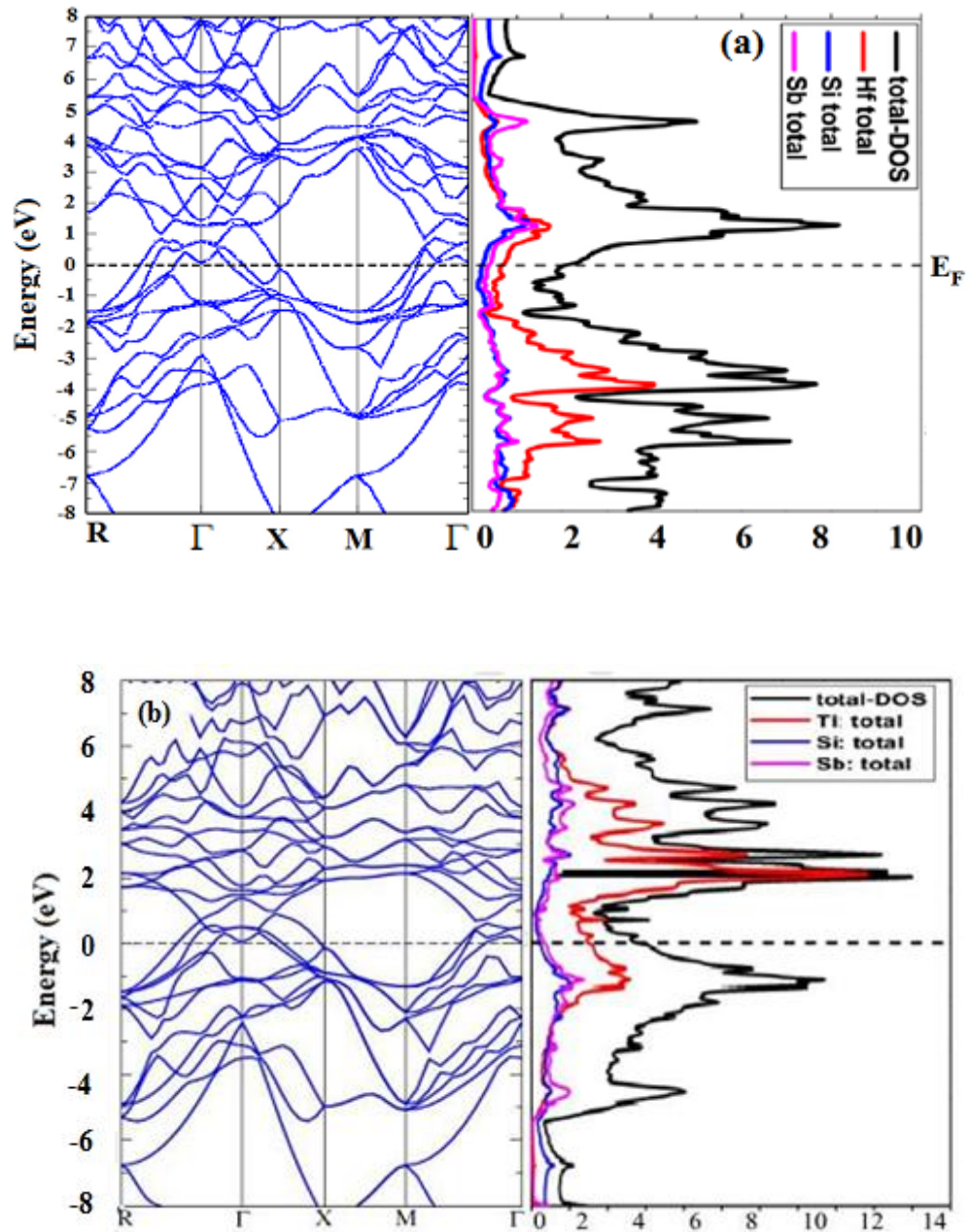


Fig. 4.3.2: Total DOS and band structure plot of (a) HfSiSb and (b) TiSiSb half-Heusler compounds, plotted using GGA approximation.

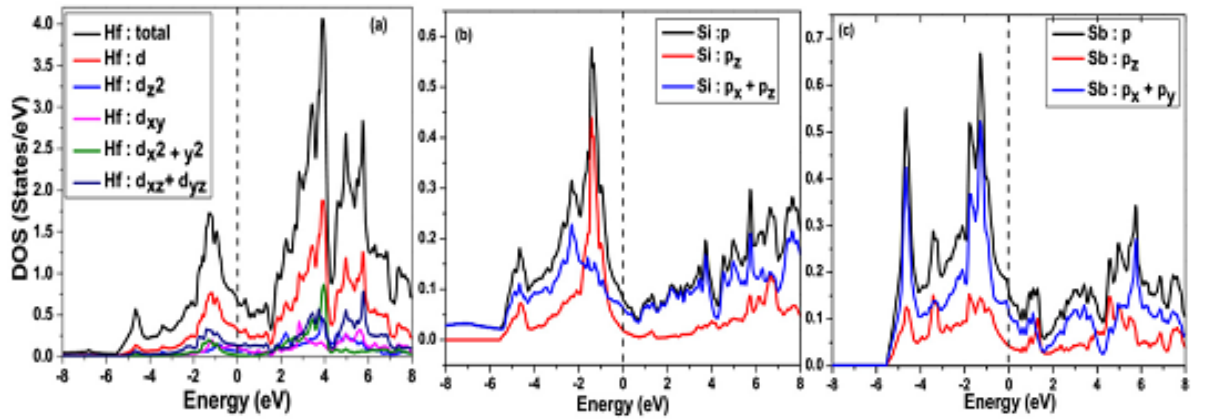


Fig. 4.3.3: Partial DOS plot of (a) Hf, (b) Si and (c) Sb for HfSiSb.

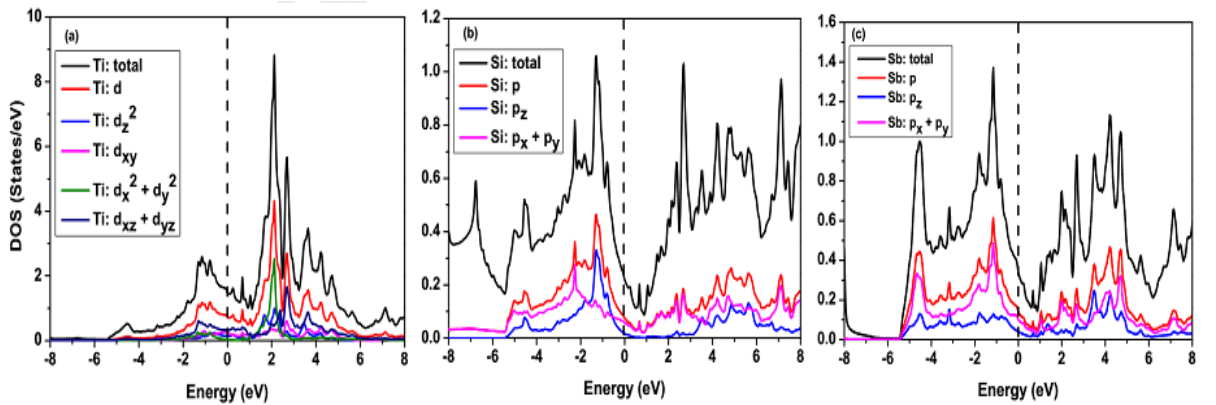


Fig. 4.3.4: Partial DOS plot of (a) Ti, (b) Si and (c) Sb for TiSiSb.

4.3.3 Thermoelectric properties of XSiSb (X=Ti, Hf)

The thermoelectric properties such as S , σ/τ , and κ/τ were calculated from the BTE in combination with the first principles band-structure calculations using a simple rigid-band and the RTA. One of the demerit of BoltzTraP is that the relaxation time is not known. TiGeSb and TiSiSb compounds have negligible heat transport, hence it can be assumed that their relaxation time is constant (Boukai *et al.*, 2008). Our calculation for electrical conductivity and electronic thermal conductivity are based upon the assumption that relaxation time is energy independent constant equal to 6.4×10^{-15} (Joshi *et al.*, 2017). We have used the constant relaxation time approximation in case of metallic compounds only and this is due to the difficulty in the calculation of the relaxation time as a function of temperature, because of the complex band structures of the metallic compounds.

Thermoelectric parameters were calculated along the XX (perpendicular) direction and along the ZZ (parallel) direction due to the tetragonal structure of the compound. Here we have only highlighted the important thermoelectric properties of the materials. The detailed properties on the electronic and the thermoelectric parameters of these compounds can be found in details in our paper (Joshi *et al.*, 2017). The lattice thermal conductivities were estimated by the RTA–BTE, as implemented in the code Phono3py (Togo *et al.*, 2015). The thermal conductivity above 100 K is due to both the electronic as well as phononic contribution. Below 100 K, electronic thermal conductivity is negligible (Li *et al.*, 2014).

A plot of thermoelectric parameters as a function of temperature is shown in Fig. 4.3.5. and 4.3.6. The calculated Seebeck coefficient for HfSiSb and TiSiSb are of the order of 10^{-4} (1000 $\mu\text{V/K}$), at room temperature (300 K). Here an additional compound

TiGeSb is also considered in order to compare the thermoelectric properties of XSiSb (X=Ti, Hf). This is done because XSiSb (X=Ti, Hf) are both hypothetical compounds and TiGeSb being a compound experimentally synthesized, its inclusion will make the comparison more practical.

From the plots it is found that the compounds work best in or around room temperature. The calculated thermoelectric parameters at room temperature are presented in table 4.3.2. At room temperature, the total thermal conductivity (κ) of TiSiSb is greater than that of TiGeSb. However along the parallel direction, κ of TiGeSb is much higher than that of TiSiSb. As the temperature increases, the κ for TiGeSb also increases linearly, whereas for TiSiSb, it remains almost constant with temperature.

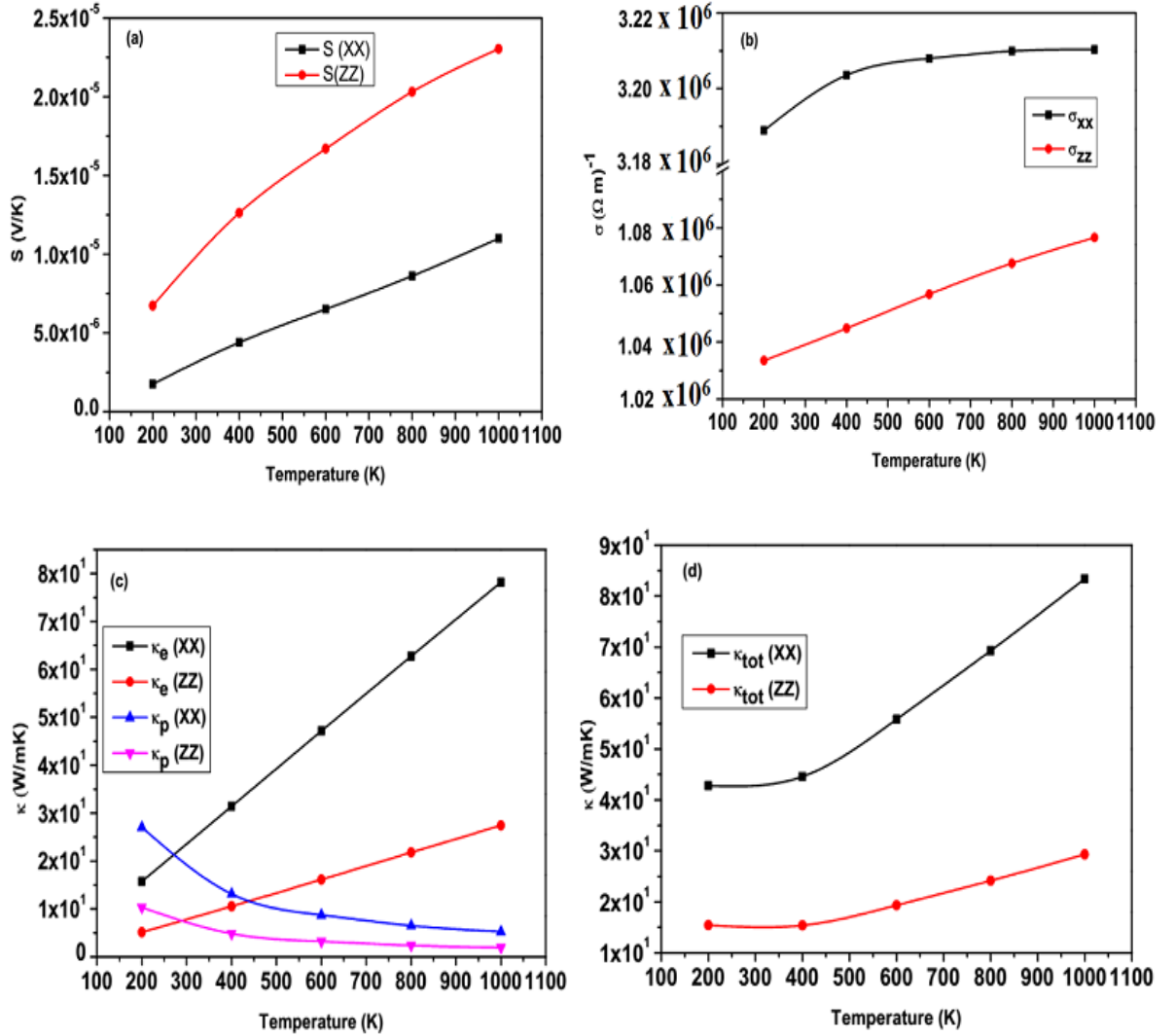


Fig. 4.3.5: Thermoelectric parameters of HfSiSb (a) Seebeck coefficient, (b) Electrical conductivity and (c) electronic and phononic thermal conductivity and (d) total thermal conductivity, as a function of temperature.

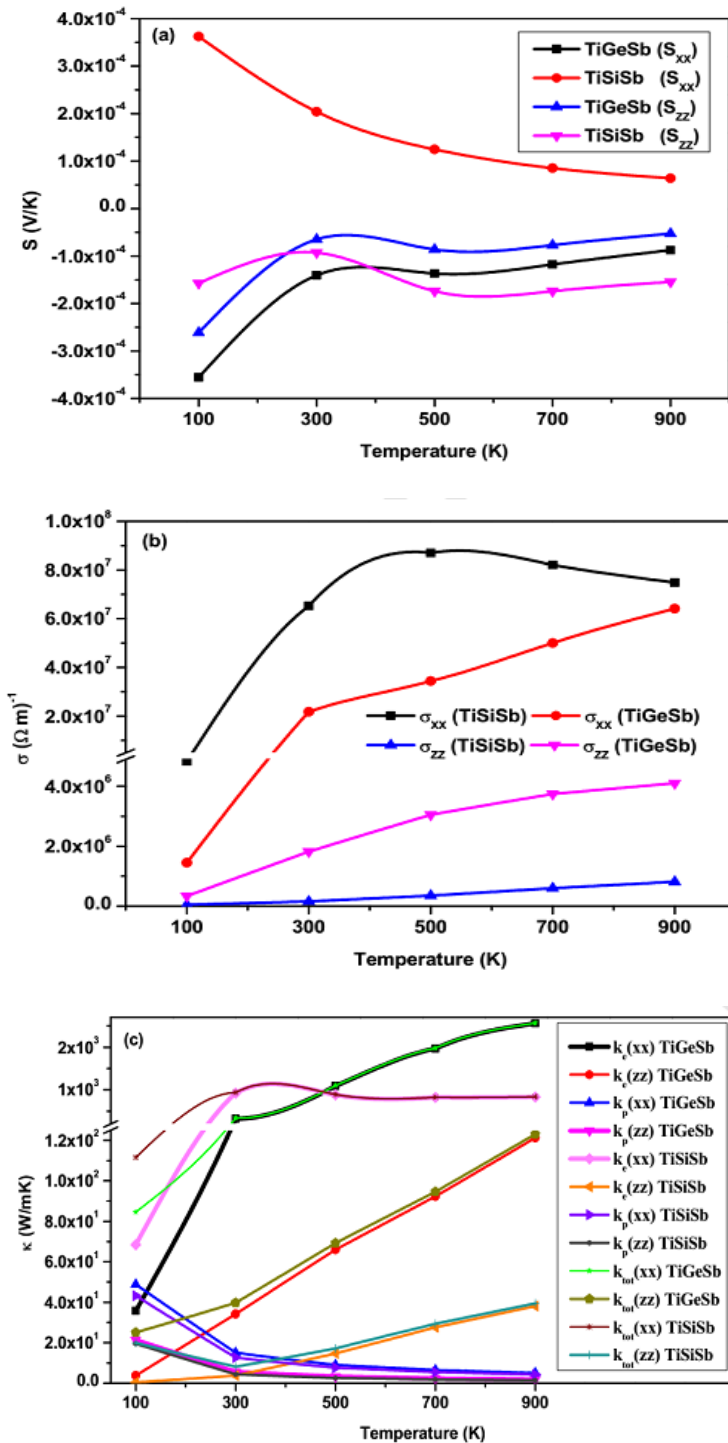


Fig. 4.3.6: Thermoelectric parameters of TiSiSb (a) Seebeck coefficient, (b) Electrical conductivity and (c) total thermal conductivity, as a function of temperature. They are compared with the more practical compound TiGeSb.

Table 4.3.2: Calculated thermoelectric parameters at room temperatures

Thermoelectric parameters	HfSiSb	TiGeSb	TiSiSb
S_{xx} (V/K)	-2.1×10^{-4}	-1.4×10^{-4}	2.04×10^{-4}
S_{zz} (V/K)	-3.26×10^{-4}	-6.5×10^{-5}	-9.25×10^{-5}
Majority Carriers (XX)	n-type	n-type	p-type
Majority Carriers (ZZ)	n-type	n-type	n-type
$\sigma_{xx} (\Omega m)^{-1}$	7.13×10^7	2.17×10^7	6.52×10^7
$\sigma_{zz} (\Omega m)^{-1}$	6.71×10^6	1.82×10^6	1.56×10^5
$\kappa_e (XX) (W/mK)$	5.67×10^2	3.52×10^2	9.23×10^2
$\kappa_e (ZZ) (W/mK)$	0.59×10^2	34.2	3.82
$\kappa_p (XX) (W/mK)$	17.65	15.1	12.7
$\kappa_p (ZZ) (W/mK)$	6.56	5.6	4.4

Chapter 5:

Conclusions

Conclusion

In this thesis, we have presented a systematic study of ground state electronic and thermoelectric properties of Heusler compounds with the following combinations $M\text{CoSb}$ ($M=\text{Ti, Zr and Hf}$), XAuSn (Sc, Lu), $\text{CoX}'\text{Y}'\text{Si}$ ($\text{X}'=\text{Y, Zr; Y}'=\text{Fe, Mn}$) and XSiSb ($\text{X}=\text{Ti, Hf}$) HH and QH compounds. . We have considered in total 9 compounds in which $M\text{CoSb}$ ($M=\text{Ti, Zr and Hf}$), XAuSn (Sc, Lu) and $\text{CoX}'\text{Y}'\text{Si}$ ($\text{X}'=\text{Y, Zr; Y}'=\text{Fe, Mn}$) crystallize into unique FCC structure with space group $F\bar{4}3m$ (No.216), whereas, XSiSb ($\text{X}=\text{Ti, Hf}$) crystallize into tetragonal $P4/nmm$ space group. We have studied the structural properties, electronic band structure, density of states and the thermoelectric properties of the compounds in its equilibrium position by using FP-LAPW method based on density functional theory (DFT). The optimized lattice parameters performed in GGA are in good agreement with the available theoretical results. The minor variations of the optimized lattice parameters with the results obtained experimentally are because of the choice of our functional (GGA), which is found to overestimate the lattice constants.

Our main aim was to study the thermoelectric properties of HH compounds which have not yet revealed their properties. In order to achieve this we used the FP-LAPW method based upon the density functional theory along with quasiharmonic approximation and Boltzmann transport theory. The structural and the electronic parameters such as the lattice constant and the energy band gap are in agreement with the

available literature. We found that HH compound MCoSb and ScAuSn are more stable and has greater probability to be synthesized experimentally (corresponding to negative formation energy) when we considered the position M; $x=y=z=0.25$, Co; $x=y=z=0$ and Sb; $x=y=z=0.75$, rather than considering the general position of HH compounds which is M; $x=y=z=0$, Co; $x=y=z=0.25$ and Sb; $x=y=z=0.5$. The modified Becke-Johnson potential is almost ineffective to compute the band gaps of the compounds and thus the customary GGA functional yields appreciable band structure related results. Thermodynamic properties study showed the decrease of Debye's temperature with the rise in temperature. This indicates that at higher temperatures the compound MCoSb becomes less anharmonic and thus tends towards harmonic oscillations. Finally, the high Seebeck coefficient and the low thermal conductivity showed the carrier concentration optimized at 10^{19} cm⁻³ and p-type MCoSb will be more efficient than the n-type MCoSb HH compounds. The lattice thermal conductivity are in close agreement with the experimental results. Our calculation is done computing the variation of relaxation time with temperature, which many theoretical studies lack. The calculated ZT value, even though not high, is still higher than the available experimental results and we believe that optimizing the transport parameters like Seebeck coefficient, electrical and thermal conductivity will further reveal high ZT values. This will add a strong support on our prediction that MCoSb has possible thermoelectric applications.

XAuSn (Sc, Lu) and CoX'Y'Si ($X'=Y$, Zr; $Y'=Fe$, Mn) compounds also showed good thermoelectric characteristics with thermal conductivity decreasing with the increase in temperatures. LuAuSn and CoYFeSi showed topological insulating behavior and these compounds can act as new type of thermoelectric materials opting to their ZT values which is quiet high, considering the pure form of the materials. Unfortunately no

experimental nor theoretical results were available for comparison because these compounds were not investigated for thermoelectric applications.

In case of HfSiSb and TiXSb (X=Ge, Si), overall shape of the band structure is found to be in well agreement with the available results. Despite of having metallic properties, TiXSb showed a potential thermoelectric characteristics. The linear increase in Seebeck coefficient with rise in temperature is key. This may be due to the low thermal conductivity and high Seebeck coefficient of the material. Hence, the present work encourage more detailed study of the systems in exploring their energy band structures in relation to structural phases. Furthermore, the effect of pressure on the system initiate phase transition and consequently the electronic structure. The another approach of tuning electronic structure is introducing the doping concentration of heavy elements. As a result the Seebeck coefficient and electrical conductivity will increase that leads to enhance ZT values. Our present study of tetragonal ternary antimonides will open a new window for further research among the family of analogous materials. The best thermoelectric materials known to date are either narrow gap semiconductors or semimetals, thus a deep profound study of these materials may lead us to metallic thermoelectric materials function able at room temperatures.

Finally, we would like to end the discussion by stating that there are some cases where GGA and mBJ does not give band gaps close to the experimental values. This may be mostly because of the temperature difference between the theoretical and the experimental setup. However, it may also be the inefficiency of the code. In some cases this can be remedied by introducing a strong intra-atomic interaction in a Hartree-Fock like manner, as an onsite replacement. This approach is commonly known as the LSDA+U method. In some case like Co₂FeAl when LSDA+U was used, it shows half-

metallic characteristics which GGA and LSDA fails to do so. However it is a very tedious method and requires heavy computational efforts and longer time. For all cases, default values of U were used by the code. However, this will be taken care of in our future works.

References

Andrea L., Hug G. and Chaput L., (2014). Ab initio lattice thermal conductivity in pure and doped Half-Heusler thermoelectric materials. ONERA-DLR Aerospace Symposium, Jun 2014, COLOGNE, Germany.

Anisimov V. I., Aryasetiawan F. and Lichtenstein A. I. (1997). First- principles calculations of the electronic structure and spectra of strongly correlated systems: the LDA+U method. *J. Phys.: Condens. Matter.*, **9**:767-808.

Anisimov V. I., Zaanen J. and Andersen O. K. (1991). Band theory and Mottinsulators: Hubbard U instead of Stoner I. *Phys. Rev. B*, **44**: 943-954.

Armstrong H., Boese M., Carmichael C., Dimich H., Seay D., Sheppard N. and Beekman M. (2017). Estimating Energy Conversion Efficiency of Thermoelectric Materials: Constant Property Versus Average Property Models. *Journal of Electronic Materials*, **46** (1).

Bardeen J. and Shockley W., (1950). Deformation Potentials and Mobilities in Non-Polar Crystals. *Phys. Rev.* **80** (72); DOI:<https://doi.org/10.1103/PhysRev.80.72>.

- Becke A. D., and Johnson E. R. (2006). A simple effective potential for exchange. *J. Chem. Phys.* **124**, 221101; <https://doi.org/10.1063/1.2213970>.
- Behnia K., (2015). Fundamentals of thermoelectricity, *Oxford University Press*, United Kingdom.
- Blaha P., Schwarz K., Madsen G. K. H., Kvasnicka D., Luitz J., Schwarz K. (2012), *An Augmented Plane Wave plus Local Orbitals Program for Calculating Crystal Properties*, Wien2K User's Guide, Techn. Universitat Wien, Wien.
- Blanco M. A., Francisco E. and Luaña V., (2004). GIBBS: Isothermal-Isobaric Thermodynamics of Solids From Energy Curves Using a Quasi-Harmonic Debye Model. *Computer Physics Communications* **158**(1): 57-72.
- Boukai A. I., Bunimovich Y., Tahir-Kheli J., Yu J. K., Goddard W. A. and Heath J. R. (2008). *Nature*, **451**.
- Bos J. G and Downie R. A., (2014). Half-Heusler thermoelectrics: a complex class of materials, *J. Phys. Condens. Matter* **26**, 433201.
- Butler J. A. V., (1925). Carnot's Cycle and the Efficiency of Heat Engines. *Nature*, **116**, 607–608.
- Chaput L., Pécheur P., Tobola J. and Scherrer H., (2005). Transport in doped skutterudites: Ab initio electronic structure calculations. *Phys. Rev. B* **72**, 085126
- Charpin T., (2001). A package for calculating elastic tensors of cubic phases using WIEN. *Laboratoire des Géomatériaux de l'IPGP 4, pl Jussieu F-75252 Paris, France.*

- Chen S. and Ren Z., (2013). Recent progress of half-Heusler for moderate temperature thermoelectric applications. *Materials Today* **16**; 327-333.
- Combes J. M., (1977). The Born-Oppenheimer Approximation. *Acta Physica Austriaca*, Suppl. **XVII**; 139-159.
- Cottenier S. (2002), *Density Functional Theory and the family of (L)APW-methods: a step-by-step introduction*, Belgium: Instituut voor Kern-en Stralingsfysica, K. U. Leuven.
- De Groot R. A., Mueller F. M., Van Engen P. G., and Buschow K. H. J. (1983). New class of materials: half-metallic ferromagnets. *Phys. Rev. Lett.* **50**(25), 2024.
- Deka D., Rahman A. and Thapa R. K., (2015). Calculation of DOS and electronic structure in Bi₂S₃ and Bi₂Se₃ by using FP-LAPW method. *IJSET*, **2**: 610-614.
- Deligoz E., Ozyar U. F. and Ozisik H. B. (2016). Theoretical investigations on vibrational properties and thermal conductivities of ternary antimonides TiXSb, ZrXSb and HfXSb. *Philosophical Magazine* **96** (16):1712-1723.
- Ding G, Gao G. Y., Yu L., Ni Y. and Yao K., (2016). Thermoelectric properties of half-Heusler topological insulators MPtBi (M = Sc, Y, La) induced by strain” *Journal Of Applied Physics* **119**, 025105.
- Domenicali C. A., (1953). Irreversible thermodynamics of thermoelectric effects in inhomogeneous, anisotropic media. *Phys. Rev.*, **92**, 877-882.

- Fetter A. L. and Walecka J.D. (1971). Quantum theory of many particle systems. *McGraw-Hill, New York.*
- Fleurial J. P., Borshchovsky A., Caillat T, Ewell R. (1997). IECEC-97 - Proceedings of the Thirty-Second Intersociety Energy Conversion Engineering Conference, Vols 1-4,1080.
- Forman C., Muritala I. K., Pardemann R. and Meyer B., (2016). Estimating the global waste heat potential. *Renewable and Sustainable Energy Reviews* **57**,1568–1579.
- Galanakis I., and Mavropoulos P. (2003). Zinc-blende compounds of transition elements with N, P, As, Sb, S, Se, and Te as half-metallic systems. *Phys. Rev. B*, **67**(10), 104417.
- Galanakis I., Dederichs P. H., and Papanikolaou N. (2002). Origin and properties of the gap in the half-ferromagnetic Heusler alloys. *Phys. Rev. B*, **66**(13), 134428.
- Galanakis I., Dederichs P. H., and Papanikolaou N. (2002). Slater-Pauling behavior and origin of the half-metallicity of the full-Heusler alloys. *Phys. Rev. B*, **66**(17), 174429.
- Gao G. Y., Yao K. L., and Li N. (2011). Preserving the half-metallicity at the surfaces of rocksalt CaN and SrN and the interfaces of CaN/InN and SrN/GaP: a density functional study. *J. Phys.: Condens. Matter*, **23**(7), 075501.

- Gao G. Y., Yao K. L., Şaşıoğlu E., Sandratskii L. M., Liu Z. L., and Jiang J. L. (2007). Half-metallic ferromagnetism in zinc-blende CaC, SrC, and BaC from first principles. *Phys. Rev. B*, **75**(17), 174442.
- Gao G. Y., and Yao K. L. (2007). Half-metallic *sp*-electron ferromagnets in rocksalt structure: The case of SrC and BaC. *Appl. Phys. Lett.*, **91**(8), 082512.
- Georges A., Kotliar G., Krauth W., Rozenberg M. J. (1996), Dynamical mean-field theory of strongly correlated fermion systems and the limit of infinite dimensions. *Rev. Mod. Phys.*, **68**: 13-20.
- Gibbs Z. M., Ricci F., Li G., Zhu H., Persson K., Ceder G., Hautier G., Jain A. and Snyder G. J., (2017). Effective mass and Fermi surface complexity factor from ab initio band structure calculations. *Computational Materials* **3** (8) ; doi:10.1038/s41524-017-0013-3
- Golesorkhtabar R., Pavone P., Spitaler J., Puschnig P. and Draxl C., (2013). ElaStic: A tool for calculating second-order elastic constants from first principles, *Computer Physics Communications* **184**: 1861-1873.
- Graf, T., Felser, C., and Parkin, S. S. P., (2011). Simple rules for the understanding of Heusler compounds. *Progress in Solid State Chemistry*, **39**(1), 1-50.
- Gross E.K.U., and Dreizler R. M. (1981). Gradient expansion of the Coulomb exchange energy. *Z. Phys.*, **302**(2), 103-106.
- Haas P., Tran F. and Blaha P., (2009). Calculation of the lattice constant of solids with semilocal functionals. *Phys. Rev. B* **79**, 209902.

- Hao A., Yang X., Wang X., Zhu Y. and Liu X. J. (2010). First-principles investigations on electronic, elastic and optical properties of XC (X = Si, Ge, and Sn) under high pressure. *J. Appl. Phys.*, **108**: 063531-063537.
- He J, Naghavi S. S., Hegde V. I., Amsler M. and Wolverton C., (2018). Designing and discovering a new family of semiconducting quaternary Heusler compounds based on the 18-electron rule. *Chem. Mater.* DOI: 10.1021/acs.chemmater.8b01096.
- Heremans J. P., Jovovic V., Toberer E.S., Saramat A., Kurosaki K., Charoenphakdee A., Yamanaka S. and Snyder G. J., (2008). Enhancement of Thermoelectric Efficiency in PbTe by Distortion of the Electronic Density of States, *Science* **321**, 554-561.
- Heusler, F.(1904). Über Manganbronze und über die Synthese magnetisierbarer Legierungen aus unmagnetischen Metallen. *Angew. Chem. Int. Ed.*, 17(9), 260-264.
- Heyd J., Peralta J. E., Scuseria G. E., and Martin R. L. (2005). Energy band gaps and Lattice parameters evaluated with the Heyd-Scuseria-Ernzerhof screened hybrid functional. *J. Chem. Phys.*, **123**(17), 174101.
- Hohenberg P., and Kohn W. (1964). Inhomogeneous electron gas. *Phys. Rev. B*, **136**(3B), B864.
- Jones R. O. and Gunnarsson O., (1989). The density functional formalism, its

applications and prospects. *Rev. Mod. Phys.* **61**, 689.

Joshi H., Rai D. P., Patra P. K., Bhamu K. C. and Thapa R. K., (2016). An Enhanced Thermoelectric Property of 1-D Silicon Atomic Wire: An Ab-Initio Study. *Nanoscience and Nanoengineering* **4**(4): 59-63.

Joshi H., Rai D. P., Sandeep, Shankar A., Patra P. K. and Thapa R. K., (2017). A comparative study of electronic and thermoelectric properties of bulk, 2D sheet and 1D wire of Silicon: an ab-initio study. *Int. J. Nanoelectronics and Materials* **10**, 93-100

Joshi H., Rai D. P., and Thapa R. K., (2018). A potential half-Heusler thermoelectric material ScAuSn: A first principle study. *AIP Conference Proceedings*, **1942**, 110056.

Joshi H, Rai D P , Deligoz E, Ozisik H. B. and Thapa R. K., (2017). The electronic and thermoelectric properties of a d₂/d₀ type tetragonal half-Heusler compound, HfSiSb: a FP- LAPW method. *Mater. Res. Express.* **4** 105506.

Joshi H, Rai D. P., Verma K.D., Bhamu K.C. and Thapa R. K., (2017). Thermoelectric properties of tetragonal half-Heusler compounds, TiXSb (X = Ge, Si): A probe from Density Functional Theory (DFT). DOI: 10.1016/j.jallcom.2017.08.065.

Kaur K, Rai D. P., Thapa R. K. and Srivastava S., (2017). Structural, electronic, mechanical, and thermoelectric properties of a novel half Heusler compound HfPtPb. *Journal Of Applied Physics* **122**, 045110.

- Kaur K., Kumar R., and Rai D.P., (2018). A promising thermoelectric response of HfRhSb half Heusler compound at high temperature: A first principle study. *Journal of Alloys and Compounds*, **748**, 127-132.
- Kittel C. and Hunklinger S., Einführung in die Festkörperchemie – Fermi-Gas freier Elektronen, volume 14, chapter 6, pages 149–177. Oldenbourg Verlag, München Wien, 2006.
- Kohn W., and Sham L. J. (1965). Self-consistent equations including exchange and correlation effects. *Phys. Rev.*, **140**(4A), A1133.
- Kresse G., and Furthmüller J. (1996). Efficiency of ab-initio total energy calculations for metals and semiconductors using a plane-wave basis set. *Comput. Mater. Sci.*, **6**(1), 15-50.
- Kundu A, Ghosh S., Banerjee R., Ghosh S. and Sanyal B., (2017). New quaternary half-metallic ferromagnets with large Curie temperatures. *Scientific Reports* **7**, DOI:10.1038/s41598-017-01782-5.
- Kurosaki K., Ohishi Y., Muta H. and Yamanaka S., (2017). *J. Mater. Chem. C*, **5**, 66-77.
- Lee M. S., Poudeu F. P. and Mahanti S. D., (2011). Electronic structure and thermoelectric properties of Sb-based semiconducting half-Heusler compounds. *Phys. Rev. B* **83**, 085204.
- Lewis S. P., Allen P. B., and Sasaki T. (1997). Band structure and transport properties of CrO₂. *Phys. Rev. B.*, **55**(16), 10253.

- Li W., Carrete J., Katcho N. A. and Mingo N., (2014). ShengBTE: A solver of the Boltzmann transport equation for phonons. *Computer Physics Communications* **185** (6); 1747-1758.
- Ma S. K. and Brueckner K. A., (1968). Correlation Energy of an Electron Gas with a Slowly Varying High Density. *Phys. Rev. Jour. Archive*, **165**(18).
- Madsen G. K. H. and Singh D. J., (2006). BoltzTraP. A code for calculating band-structure dependent quantities. *Computer Physics Communications* **175**; 67–71.
- Mahan G. D. and Sofo J. O., (1996). The best thermoelectric. *Proc. Natl. Acad. Sci. U.S.A.*, **93**(15):7436– 7439.
- Melnyk G., Bauer E., Rogl P., Skolozdra R. and Seidl E., (1999). Thermoelectric properties of ternary transition metal antimonides. *Journal of Alloys and Compounds* **296**; 235–242.
- Morelli D. T. and Slack G. A., (2006). High Lattice Thermal Conductivity Solids. In: Shindé S.L., Goela J.S. (eds) *High Thermal Conductivity Materials*. Springer, New York, NY
- Murnaghan F. D. (1944). The Compressibility of Media under Extreme Pressures, *Proc. Natl. Acad. Sci., USA* , **30**: 244-247.
- Offernes L., Ravindran P. and Kjekshus A., (2007). Electronic structure and chemical bonding in half-Heusler phases, *Journal of Alloys and Compounds* **439**; 37–54.

- Olvera A. A., Moroz N. A., Sahoo P., Ren P., Bailey T. P., Page A. A., Uher C. and Poudeu P. F. P., (2017). Partial indium solubility induces chemical stability and colossal thermoelectric figure of merit in Cu₂Se. *Energy & Environmental Science*, **7**, 328-336.
- Osterhage H., Gooth J., Hamdou B., Gwozdz P., Zierold R. and Nielsch K., (2014). Thermoelectric properties of topological insulator Bi₂Te₃, Sb₂Te₃, and Bi₂Se₃ thin film quantum wells. *Appl. Phys. Lett.* **105**, 123117.
- Otero-de-la-Roza A., Abbasi-Pérez D. and Luaña V., (2011). Gibbs2: A new version of the quasiharmonic model code. II. Models for solid-state thermodynamics, features and implementation. *Computer Physics Communications* **182**; 2232–2248.
- Pauling L. (1938). The nature of the interatomic forces in metals. *Phys. Rev.*, **54**(11), 899.
- Pei Y., Wang H., and Snyder G. J., (2012). Band engineering of thermoelectric materials. *Adv. Mater.* **24**(46):6125–6135.
- Perdew J.P.(1985). Density functional theory and the band gap problem. *Int. J. Quantum Chem.*, **28**(S19),497-523.
- Perdew J.P.(1986). Density-functional approximation for the correlation energy of the inhomogeneous electron gas. *Phys. Rev. B*, **33**(12), 8822.
- Perdew J. P., and Wang Y. (1992). Accurate and simple analytic representation of the electron-gas correlation energy. *Phys. Rev. B*, **45**(23),13244.

- Perdew J. P., and Zunger A. (1981). Self-interaction correction to density-functional approximations for many-electron systems. *Phys. Rev. B*, **23**(10), 5048.
- Perdew J. P., Burke K., and Ernzerhof M. (1996). Generalized gradient approximation made simple. *Phys. Rev. Lett.* **77**(18), 3865.
- Rai, D.P., Sandeep, Shankar, A., Ghimire, M.P., Thapa, R.K., (2012). Ground State Study of Co₂Val: LSDA+U method, *Phys. Scr.* **86**: 405702-11.
- Rowe D., (2005) *Thermoelectrics Handbook*, edited by D. Rowe (CRC Press, 2005).
- Ritchie H., and Roser M., (2018). Energy Production & Changing Energy Sources. Published online at OurWorldInData.org. Retrieved from: [https://ourworldindata.org/energy-production-and-changing-energy-sources'](https://ourworldindata.org/energy-production-and-changing-energy-sources) [Online Resource].
- Sawai W., Lin H. Markiewicz R. S., Wray L. A., Xia Y., Xu S. Y., Hasan M. Z. and Bansil A., (2010). Topological electronic structure in half-Heusler topological insulators. *Phys. Rev. B* **82**, 125208.
- Saqr K. M., Mansour M. K., Musa M. N., (2008). *Int J Automot Techn* **9**, 155-159.
- Schwarz K. and Blaha P. (2003), Solid state calculations using WIEN2k, *Computational Materials Science*, **28**: 259-273.
- Sebastian C.P., Eckert H., Rayaprol S., Hoffmann R. D. and Pottgen R., (2006). Crystal chemistry and spectroscopic properties of ScAuSn, YAuSn and LuAuSn. *Solid State Science* **8** (5); 560-566.

- Seebeck T., (1823). Magnetische Polarisation der Metalle und Erze durch Temperatur-Differenz, *Abhandlungen der Deutschen Akademie der Wissenschaften zu Berlin*.
- Sekimoto T., Kurosaki K., Muta H., and Yamanaka S., *IEEE- 24th International Conference on Thermoelectrics* (2005).
- Sekimoto T., Kurosaki K., Muta H., and Yamanaka S., (2007). High-Thermoelectric Figure of Merit Realized in p-Type Half-Heusler Compounds: $\text{ZrCoSn}_x\text{Sb}_{1-x}$. *Japanese Journal of Applied Physics* **46** (2); 25–28.
- Shankar A., Rai D. P., Sandeep, Khenata R., Thapa R. K. and Mandal P. K., (2016). Electronic Structure and Thermoelectricity of Filled skutterudite $\text{CeRu}_4\text{Sb}_{12}$, *Journal of Alloys and Compounds*, **672**: 98-103.
- Sherman B., Heikes R. R. and Ure R. W., (1960). Calculation of Efficiency of Thermoelectric Devices. *J. Appl. Phys.* **31** (1); doi: 10.1063/1.1735380.
- Shi F., Jia L., Si M. S., Zhang Z., Xie J., Xiao C., Yang D., Shi H. and Luo Q., (2018). Tunable band inversion in half-Heusler topological LuAuSn/LuPtBi superlattices. *Appl. Phys. Express.* **11**, 095701; DOI <https://doi.org/10.7567/APEX.11.095701>.
- Silpawilawan W, Kurosaki K, Ohishi Y, Muta H and Yamanaka S., (2017). FeNbSb p-type half-Heusler compound: beneficial thermomechanical properties and high-temperature stability for thermoelectrics, *J. Mater. Chem. C*, **5**, 6677-6681.
- Slater J. C. (1936). The ferromagnetism of nickel. II. Temperature effects. *Phys. Rev.*, **49**(12), 931.

- Snyder G. J. and Toberer E.S., (2008). Complex thermoelectric materials, *Nature Materials* **7**, 105–114.
- Sootsman J. R., Chung D. Y., and Kanatzidis M. G., (2009). New and old concepts in thermoelectric materials. *Angew. Chem. Int. Ed.*, **48**(46), 8616-8639.
- Stadnyk Y., Horyn, A., Romaka, V. V., Gorelenko, Y., Romaka, L. P., Hlil, E. K., & Fruchart, D. (2010). Crystal, electronic structure and electronic transport properties of the $Ti_{1-x}V_xNiSn$ ($x=0-0.10$) solid solutions. *J. Solid State Chem.*, **183**(12), 3023-3028.
- Sun G., Li Y., Zhao X., Mi Y. and Wang L., (2015). First-Principles Investigation of the Effect of M-Doped (M = Zr, Hf) TiCoSb Half-Heusler Thermoelectric Material, *Journal of Materials Science and Chemical Engineering* **3**; 78-86.
- Tobola J., Pierre J., Kaprzyk S., Skolozdra R. V., and Kouacou M. A. (1998). Crossover from semiconductor to magnetic metal in semi-Heusler phases as a function of valence electron concentration. *J. Phys.: Condens. Matter* **10** (5), 1013.
- Togo A. and Tanaka I., (2015). First principles phonon calculations in materials science. *Scr. Mater.* **105**; 1-5.
- Wang C. H., Liu C. J., Wang C. L., Chien C. C., Hwu Y., Liu R. S., Yang C. S., Je J. H., Lin H. M. and Margaritondo G., (2009). Intense X-ray induced formation of silver nanoparticles stabilized by biocompatible polymers. *Applied Physics A* **97** (2); 295-300.

- Wimmer, E., Krakauer, H., Weinert, M., and Freeman, A. J. (1981). Full-potential self-consistent linearized-augmented-plane-wave method for calculating the electronic structure of molecules and surfaces: O₂ molecule. *Phys. Rev. B*, **24**(2), 864.
- Wolfgang G. Zeier. (2017). New tricks for optimizing thermoelectric materials. *Current Opinion in Green and Sustainable Chemistry* **4**, 210-213.
- Xi J., Long M., Tang L., Wang D. and Shuai Z. (2012). First-principles prediction of charge mobility in carbon and organic nanomaterials, *Nanoscale* **4**(15):4348-69.
- Yan X., Joshi G., Liu W., Lan Y., Wang H., Lee S, Simonson J. W., Poon S. J., Tritt T. M., Chen G. and Ren Z. F., (2011). Enhanced Thermoelectric Figure of Merit of p-Type Half-Heuslers, *Nano Lett.*, **11** (2), 556–560.
- Yamamoto A., Miyazaki H. and Takeuchi T., (2014). Thermoelectric properties of Al-(Mn,X)-Si C54-phase (X = Ru and Re), *Jour. of Appl. Phys.* **115**, 023708; <https://doi.org/10.1063/1.4861643>.
- Yang J., Li H., Wu T., Zhang W., Chen L. and Yang J., (2008). Evaluation of Half-Heusler Compounds as Thermoelectric Materials Based on the Calculated Electrical Transport Properties. *Adv. Funct. Mater.*, **18**, 2880–2888.
- Yuan B., Wang B., Huang L., Lei X., Zhao L., Wang C. and Zhang Q., (2017). Effects of Sb Substitution by Sn on the Thermoelectric Properties of ZrCoSb. *Journal of Electronic Materials* **46** (5); 3076–3082.

- Zeier W.G., (2017). New tricks for optimizing thermoelectric materials. *Current Opinion in Green and Sustainable Chemistry*, **4**, 23-28 doi:10.1016/j.cogsc.2017.02.003
- Zheng, Jin-cheng, (2008). Recent advances in thermoelectric materials, *Front. Phys. China* **3**:269-279.
- Zoroddu A., Bernardini F., Ruggerone P. and Fiorentini V., (2001). First-principles prediction of structure, energetics, formation enthalpy, elastic constants, polarization, and piezoelectric constants of AlN, GaN, and InN: Comparison of local and gradient-corrected density-functional theory. *Phys. Rev. B* **64**, 045208; DOI:<https://doi.org/10.1103/PhysRevB.64.045208>.

Brief Biodata of Himanshu Joshi

36/1 Leborg cart road, Singamari, Darjeeling, West Bengal, India-734101

Email : himanshuabijoshi09@gmail.com

Phone: +918257803359

EDUCATION

Mizoram University	Aizawl, Mizoram
Ph.D. in Physics	November, 2018
Mizoram University	Aizawl, Mizoram
M.Sc in Physics	July, 2015
University of North Bengal	Siliguri, West Bengal
B.Sc. with Honors in Physics	May, 2013

RESEARCH EXPERIENCE

- Worked as a JRF in a research project entitled “Search of New class of thermoelectric material among the family of Heusler compounds: A First Principle Study”, under DST-SERB, Govt. of India from September 2016 - September 2018.
- Worked on electronic structure, optical and elastic properties of Heusler compounds using the Full Potential Linearized Augmented Plane Wave method based upon Density Functional Theory.
- Performed theoretical calculation on transport properties of Heusler compounds and calculated their thermoelectric figure of merit.

- Managed to calculate the lattice thermal conductivity of Heusler and Perovskite type compounds.
- Published several research papers in reputed National/International Journals.
- Participated in several National/International Workshops/Conferences in India as well as abroad.
- Submitted Ph.D. thesis entitled “Theoretical investigation of a new class of thermoelectric materials among the family of Heusler compounds” to Mizoram University, Aizawl, Mizoram, India.

LEADERSHIP/TEAMWORK EXPERIENCE

- Was a member of the local organizing committee for Condensed Matter Days-2016, A National Conference organized by Dept. of Physics, Mizoram University.
- Mentored and trained 4 post graduate students for Masters Dissertation.
- Has been an active member of the Condensed Matter Theory Research Group, Mizoram University, India from July 2013 till date.
- Has been giving lecture classes to post graduate students on Condensed Matter Physics and Quantum Physics.
- Has served the Department of Physics, St. Josephs College Darjeeling as Class Representative during the academic year 2012-2013.

ADDITIONAL EXPERIENCE

- Successfully completed nine years course in Human Value Education from Sri Satya Sai Seva Organization.
- Served as a Cadet in NCC for two years and attended camping programs.

- Has passed the NCC Certificate “A” examination.
- Completed six months course in Hardware Maintenance and Networking from Manipal Institute of Computer Education.

SKILLS

LANGUAGE:

- English – Full professional proficiency
- Nepali – Full professional proficiency
- Hindi – Full professional proficiency

TECHNICAL

- Working knowledge of FORTRAN and C++ programming languages.
- Working knowledge of Wien2K, FHI-AIMS, Quantum Espresso and SPR-KKR computer codes.
- Professional proficiency in MS-Word, MS-Excel, MS-Paint, Latex, Origin, XM-Grace, Gnu plot etc. data editing and plotting softwares.
- Working knowledge of Windows and Linux/Unix based operating systems.

PERSONAL INFORMATION

Name	:	Himanshu Joshi
Father’s Name	:	Shanker Prasad Joshi
Mother’s Name	:	Duhita Joshi
Date of Birth	:	27 th February, 1991

RESEARCH PUBLICATIONS

(A) Journals

- [1] A. Shankar, D.P. Rai, Sandeep, **H. Joshi**, R. Khenata, M.P. Ghimire, R.K. Thapa, P.K. Mandal, Energy band structure, elastic and optical constants of the filled skutterudite CeRu₄As₁₂, Materials Science in Semiconductor Processing 46 (2016), pp. 10–16.
- [2] **H. Joshi**, D. P. Rai, Sandeep and R. K. Thapa, Electronic structure and Thermoelectric property of Co₂YGe (Y=Mn, Fe) Heusler compounds: A First Principle Study, Journal of Physics Conference series (2016).
- [3] **H. Joshi**, D. P. Rai, P. K. Patra, K. C. Bhamu and R. K. Thapa, An Enhanced Thermoelectric Property of 1-D Silicon Atomic Wire: An Ab-Initio Study, Nanoscience and Nanoengineering 4 (2016), pp. 59-63.
- [4] **H. Joshi**, D. P. Rai, E Deligoz, H B Ozisik and R K Thapa, The electronic and thermoelectric properties of a d₂/d₀ type tetragonal half-Heusler compound, HfSiSb: a FP-LAPW method, Mater. Res. Express 4 (2017) 105506.
- [5] **H. Joshi**, D.P. Rai, K.D. Verma, K.C. Bhamu, R.K. Thapa, Thermoelectric properties of tetragonal half-Heusler compounds, TiXSb (X = Ge, Si): A probe from Density Functional Theory (DFT), Journal of Alloys and Compounds, 756 (2017).
- [6] **H. Joshi**, D.P. Rai and R. K. Thapa, An Insight to the Structural, Physical, Optical, Mechanical, Elastic, Thermodynamic and Enhanced thermoelectric properties of Half- Heusler MCoSb (M= Ti, Zr and Hf) intermetallics. (Communicated)
- [7] **H. Joshi**, Lalhriatpuia Hnamte, D.P. Rai and R. K. Thapa, Thermoelectric properties of ZrSiSn: A First principle approach (Accepted in Indian Journal of Physics).
- [8] **H. Joshi** and R. K. Thapa, Thermoelectricity of Half-Heusler Topological Insulator LuAuSn. (Communicated).
- [9] Lalhriatpuia Hnamte, **H. Joshi** and Thapa R. K. (2018), Investigation of the Electronic and Optical properties of double perovskite oxide Pb₂ScMO₆ (M=Ta, Sb): A first principle approach. Journal of Physics and Chemistry of Solids (Elsevier) (Communicated)
- [10] Neupane, K., **H. Joshi**, Hnamte, L. and Thapa, R. K., Study of structural and electronic properties of KCaF₃ type fluoro-perovskite, International Research Journal of Advanced Engineering and Science (IRJAES), ISSN (online): 2455-9024.

(B) Conference Proceedings

- [1] Lalhriatpuia Hnamte, Sandeep, **H. Joshi**, and Thapa R. K. (2017), Electronic and optical properties of double perovskite Ba_2VMoO_6 : FP-LAPW study. AIP Conference Proceedings 1953, 140132. doi: 10.1063/1.5033307.
- [2] **H. Joshi**, D. P. Rai, and R. K. Thapa, A potential half-Heusler thermoelectric material $ScAuSn$: A first principle study, AIP Conference Proceedings 1942, 110056 (2018); doi: 10.1063/1.5029039.
- [3] **H. Joshi**, D P Rai, Sandeep and R K Thapa, Electronic structure and thermoelectric property of Co_2YGe ($Y=Mn, Fe$) Heusler compounds: a first principle study, Journal of Physics: Conference Series 765 (2016), 012010 doi:10.1088/1742-6596/765/1/012010.

CONFERENCE AND WORKSHOPS ATTENDED

1. Hands-On Workshop and Humbolt Kolleg: Density Functional Theory and beyond - basic principles and modern insights, Isfahan University of Technology (Iran), from 2-13 May 2016.
2. CMDAYS-2016, A National Conference Organized by the Department of Physics, Mizoram University from 29-31 August 2016
3. CMDAYS-2017, A National Conference Organized by the Department of Physics, Tezpur University, from 29-31 August 2017.
4. DAE-SSPS (Solid State Physics Symposium), Organized by Bhabha Atomic Research Center from 26th-30th DEC, 2017 held at Bhabha Atomic Research Center, Mumbai.

PAPER PRESENTATION IN CONFERENCE AND WORKSHOPS

1. Presented a poster entitled “Study of Thermoelectric figure of merit of 1-D Silicon atomic wire, In ”Hands-On Workshop and Humbolt Kolleg: Density Functional Theory and beyond - basic principles and modern insights, Isfahan University of Technology (Iran), from 2-13 May 2016.
2. Presented a paper entitled “Electronic structure and Thermoelectric property of Co_2YGe ($Y=Mn, Fe$) Heusler compounds: A First Principle Study.” at CMDAYS-2016, A National Conference Organized by the Department of Physics, Mizoram University from 29-31 August 2016.
3. Presented a paper entitled “Thermoelectric properties of Half- Heusler compound $HfGeSb$: A First Principle approach” at at CMDAYS-2017, A National

Conference Organized by the Department of Physics, Tezpur University, from 29-31 August 2017.

4. Presented a poster entitled “Quest for thermoelectricity in Half-Heusler compounds: A first principle approach” at at CMDAYS-2017, A National Conference Organized by the Department of Physics, Tezpur University, from 29-31 August 2017.

5. Attended the DAE-SSPS (Solid State Physics Symposium) from 26th-30th DEC, 2017 held at Bhabha Atomic Research Center, Mumbai , India and presented a poster entitled “A Potential Half-Heusler ScAuSn: A First Principle study”.